A Dissertation

entitled

Fundamentals of Corona Assisted Flow Instabilities: From Liquid Manipulation to Emulsion Formation to Separation

by

Mohcen Shahbaznezhad

Submitted to the Graduate Faculty as partial fulfillment of the requirements for the Doctor of Philosophy Degree in Electrical Engineering

_____

Dr. Hossein Sojoudi, Chair

_____

Dr. Richard G. Molyet, Co-Chair

_____

Dr. Mohammed Niamat, Committee Member

_____

Dr. Abbas Semnani, Committee Member

_____

Dr. Yakov Lapitsky, Committee Member

_____

Dr. Barry Scheuermann
Dean College of Graduate Studies

The University of Toledo

Spring 2021

An Abstract of

Fundamentals of Corona Assisted Flow Instabilities: From Liquid Manipulation to Emulsion Formation to Separation

by

Mohcen Shahbaznezhad

Submitted to the Graduate Faculty as partial fulfillment of the requirements for the Doctor of Philosophy Degree in Electrical Engineering

The University of Toledo

September 2020

Table of Contents

List of Tables

List of Figures

List of Abbreviations

EHD	Electro Hydro-Dynamic
DDI	Dipole-Dipole Interaction
EP	Electrophoresis
DEP	Dielectrophoresis
A	Angstrom
W/O	Water in Oil emulsion
O/W	Oil in Water emulsion
EFD	Electro-Fluid-Dynamic

Summary

Electrohydrodynamic (EHD) found a lot of attention in the scientific community because of its low energy and flexibility in addressing different challenges. The first chapter of this dissertation explains the history of using EHD to manipulate, separation and emulsion formation, and also talks about the theory and mechanism of gaseous discharge. The second chapter of this dissertation presents the results of experimental observations of the EHD flow induced in bulk dielectric liquid layers using corona discharge. The governing liquid properties for the deformations are discussed, indicating the vital role of surface tension and viscosity. Critical voltages at which rapid transformation of the liquid's deformation occurs are identified and discussed. The liquid layer thickness is shown to be a dominant parameter in the efficacy of such proposed pump designs.

Chapter third discusses an experimental approach to study the effects of a contactless method on electrocoalescence of water in oil (W/O) emulsion. A positive corona discharge is utilized to create a nonuniform electric field for the coalescence of water droplets ranging from nano to macro sizes in oil mediums. Two approaches are employed in this chapter; qualitative analysis conducted by visually studying coalescence patterns in videos captured with a high-speed camera, and a quantitative analysis based on calculations obtained from dynamic light scattering (DLS) measurements. From the behavior of the water droplets under the electric field, it is observed that dipole-dipole interaction (DDI), migratory

coalescence (electrophoresis (EP)), and dielectrophoresis (DEP) have major roles in promoting the coalescence events.

Chapter fourth investigates the impacts of non-uniform and pulsed DC electric fields on the coalescence of water droplets inside an oil medium. The operating process parameters were experimentally calibrated and optimized to increase the effectiveness and energy consumption efficiency of the coalescence process. High-speed imaging and image processing techniques were used to investigate the effect of different active forces (*i.e.* DDI, EP, and DEP) during the coalescence process. An optimal coalescence recipe was proposed by continuous measurement of the distance, velocity, and acceleration of the coalescing water droplets.

Chapter fifth introduces a top-down method of emulsion formation that is proposed using a contactless corona discharge applicable to a wide range of emulsions (e.g. macro, nanoemulsions). The corona discharge creates an ionic wind (electroconvection) that drags water vapor droplets, created by a humidifier, into an oil medium. The corona discharge also induces motion of the oil medium via an electrohydrodynamic (EHD) pumping effect using a modulated bottom electrode geometry. By these two effects, this contactless method enables immersion of the water droplets into the moving oil medium continuously forming a water-in-oil (W/O) emulsion. This method does not require high power and/or an excessive amount of surfactant. The medium used in this study was silicone oil in different viscosities. The impact of oil viscosity in the properties of created emulsion and the power consumption of the process is studied. This is a low-cost, contactless, and power-efficient process enabling the continuous formation of emulsions with varying oil viscosities.

Chapter 1

1 Electrohydrodynamics, electrocoalescence, and emulsion

1.1 Introduction

Electrohydrodynamics (EHD), also known as Electro-Fluid-Dynamic (EFD), is caused and defined by the motion of a liquid or gas phase of materials in the presence of an electric field [1]. Thanks to its diverse applications, EHD has introduced many new areas of study in physics, medicine, and engineering sciences. However, a few studies related to EHD are focused on gas ionization and particularly corona discharge [2].

1.1.1 Early discovery of corona discharge

Corona was first introduced in a book authored by Peek, F.W. (1929). He found out that by increasing the voltage between two smooth conductors to a critical potential, hissing

noise and a visible violet arc can be observed, followed by ozone formation [3]. He also mentioned that in the overstressed air, O_2 and N_2 react, leading to oxide formation and power loss through chemical reactions, arc formation, noise, and the heat from the discharge current. In his reports, he mentioned that the wattmeter shows significantly different higher values, while the voltage level is increased. The same phenomenon happens while implementing alternating and direct currents. Utilizing a stroboscope, he **Figure**d out the different patterns in positive and negative corona discharges. While applying a negative voltage, red-colored beads appear on the wire, whereas applications of positive voltage resulted in a smooth blue-colored fine arc. In order to mathematically analyze the electric field strength (E), he proposed an equation that considers air density and the corona electrode radius [3].

$$V_0 = m_v g_0 \delta r_e \left(1 + \frac{c}{\sqrt{\delta r_e}}\right) \ln\left(\frac{x}{r_e}\right) \qquad (1-1)$$

where V_0 is corona onset voltage, m_v is electrode irregularity factor, g_0 disruptive electric field, δ is the air density factor, r_e is electrode radius, c is a constant, and *x* is corona gap.

1.1.2 Corona discharge and its applications

Corona has been previously implemented in mass spectrometry to determine the elemental/chemical composition of components; it also had extensive use in ozone production and water treatment applications [4-7]. In air filtration applications, the corona is used to deposit particles such as dust and soot electrostatically [8]. Other well-known

forms of corona can be named the electrostatic painting, separation, and electrospinning of polymers [8-10]. The corona wind also got attention thanks to its capabilities in heat [11-14] and mass transport applications [15-18]. It provides promising enhancement of convection in heat transfer of internal [19, 20] and external flows [21], while it is widely used in evaporation/drying [17, 22, 23] and flame control tasks [24-26].

1.2 The electrical discharge in gases and corona discharge

The electrical discharge in gaseous media takes place in different regimes, which results in various physical explanations of the process. Charge carriers can be delivered by different means. The most common ones are extreme injections of ionized gas molecules, small particles, or charged droplets, and the generation of the charged segments by direct gas ionization. The latter scheme happens when there exists sufficient excitation of the gas media in order to disintegrate the molecular bonding in the electric field. As a result, there is a high chance that the properties of the gas molecules change significantly with an ultimate level of switching to a localized gas plasma in the system occurs.

An effective way to introduce charges inside the system is to exploit “Townsend Avalanche,” which is literally generating an avalanche multiplication of free electrons with impact ionization of neutralized gas molecules[27]. In order to achieve this state, the free electrons in the gas media must receive an energy level higher than that of gas ionization in order to supply sufficient kinetic energy for a free traverse period. An ion-electron pair will form after the molecules undergo the mentioned condition. By each collision, the

newly generated charges get accelerated in the external electric field and lead to a chain reaction of collisions, causing an avalanche of the charged carriers. After passing a critical number of paired carriers in the media, it can be concluded that the gas is transformed into a plasma state.

The occupation region of plasma is geometry-dependent, even in uniform electric fields. Thus, with a modification of electrode geometric design, it is possible to have a thin layer of plasma in the working system. For instance, a sharp anode pole (usually thin wires or sharp pins) will give strong electric fields, and the electrons can be easily attracted by the cathode pole. This happens while the positive charges need to move through a low electric field in order to reach the cathode pole, forming a drift region. Due to this property, the charge carriers are considered to be unipolar [28]. It is not arbitrary to have the ionizing region close to the anode pole, and in fact, it has some noticeable advantages. Firstly, there is only one type of carrier existing in the drift region, which is positive ions. At the same time, if the ionizing takes place close to the cathode pole, there might be some negative ions (electrons) in the region. The other advantage is that in the anode region, ozone production is minimal compared to the cathode region, which leads to enhanced material durability [29]. The analysis in the drift region is focused on the drift region composition or fluid outside of the ionization layer. This specific region is also known as the “corona discharge” region. Since in this region, the fluid properties are considered to be close to full uniform, this leaves the macroscopic modeling approaches with the advantage of assigning current density as a function of the external electric field.

In general, gas discharge is categorized into three regimes (shown in **Figure 1-1**): 1) Dark discharge or Townsend, 2) Glow discharge, and 3) Arc discharge. 1) Townsend discharge happens below the breakdown voltage, and it consumes current in the range of microamps. 2) Glow discharge, which happens when the voltage reaches breakdown voltage and current increases to the range of milliamps. 3) Arc discharge, in which the current increases significantly in the range of hundreds of amps producing heat. In theory, arc discharge can be either thermal discharge or non-thermal discharge

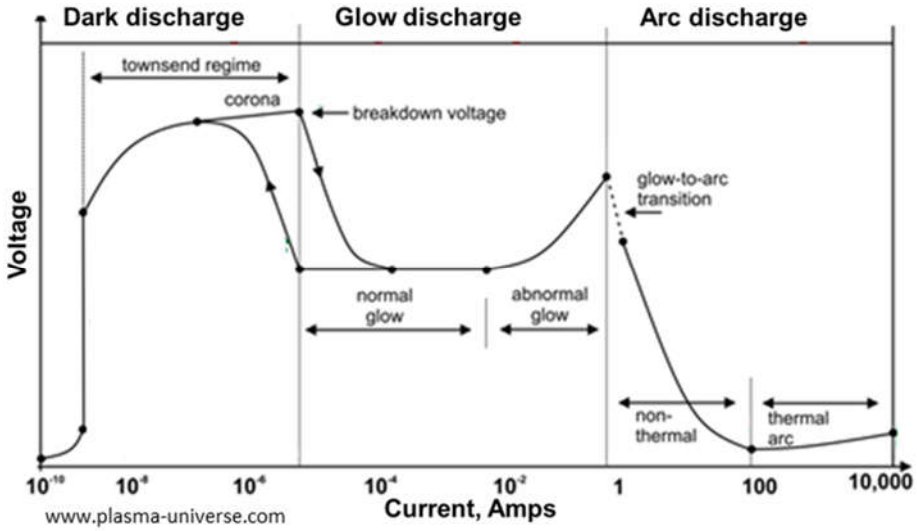

Figure 1-1 Gas discharge regimes.

The behavior of gases and the ionization process are changed by the different polarity of the electrodes and an AC discharge.

To distinguish different regimes, Akishev suggested the following formula for corona to glow discharge:

$$\frac{I}{V}=k(V-V_0) \tag{1-2}$$

where K is a constant, and V is the applied voltage. The discharge regime is Townsend when the value of K is constant for different voltages and currents. The polynomial value suggests that we are entering the glow discharge regimes.

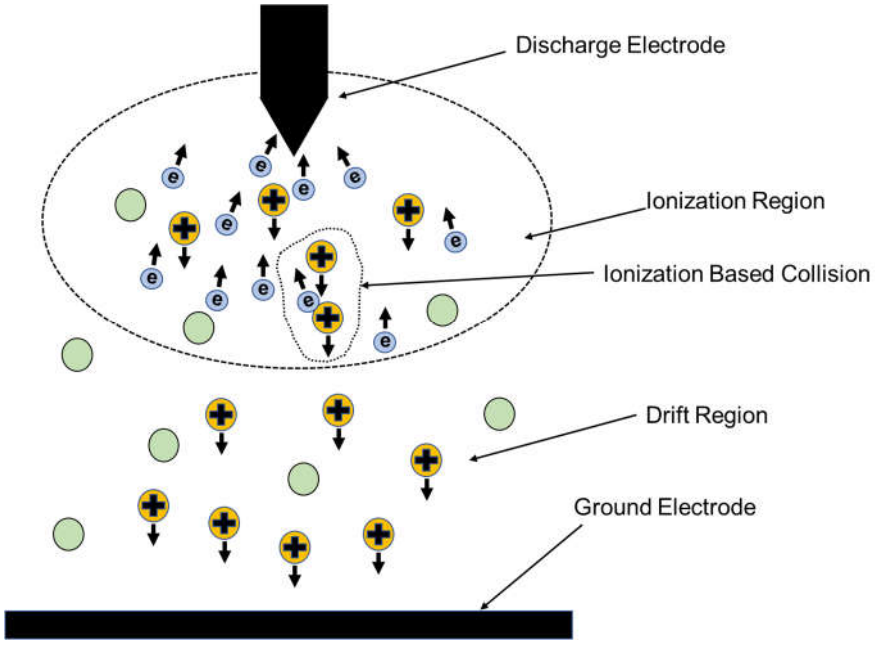

Figure 1-2 Gas ionization process in the positive corona discharge.

1.2.1 Positive corona discharge

In positive corona discharge, a density of free electrons is much lower than negative corona discharge, and they are in the range of thousandths in density. However, in the positive corona discharge, the density of electrons in the region near the sharp electrode or high potential gradient is larger, where electrons have enough energy to be liberated from

neutral atoms or molecules [30]. Hence, the positive discharge is more suitable for an application that requires higher activation energy.

In positive corona discharge, ionization initiates by an external agent in the region of the high potential gradient, and a liberated electron is attracted to the sharp electrode. In contrast, the positive ion approaches the ground electrode. Collisions between the ions and neutral molecules (atoms) in the area close to the sharp electrode create more and more liberated electrons and cause a phenomenon called an electron avalanche [31], as shown in **Figure** 1-2.

1.2.2 Negative corona discharge

The process of ionization in negative corona discharge is more complex than in positive discharge. In negative corona discharge, the required energy for liberating electrons from the sharp electrode is lower than liberating from a neutral atom. As a result, the source of ionization is the flow of electrons, which moves outward from the sharp electrode, and the liberated electrons from neutral molecules (atoms) are not useful to sustain the discharge [30, 32]. Also, the collision of the positive ions to the sharp electrode can liberate another electron from the surface. During the movement of the electrons in the drift region towards the opposite electrode, they encounter other molecules (atoms) such as oxygen or water vapor, attaching to them and producing negative ions [33] (**Figure** 1-3).

1.3 EHD flow

EHD results from the collision of the accelerated particles in an electric field and the molecules introduced from the neutral gas [34]. This collision leads to an "ionic wind," which is simply the rise of induced airflow. This flow was reported by Cabeo for the very first time in 1629 [35]. However, the first official observation was reported by Hauksbee in 1709 [36]. While he discovered that the weak wind is formed close to an electrified object, Cavalo has reported the first qualitative description of the ionic wind. Faraday, in turn, explored the movement mechanism of air particles between two electrodes while a high voltage is applied. In his report, he concluded that the ionic wind is caused by momentum transfer between the charged/uncharged particles. After all these efforts, Maxwell released the most comprehensive explanation of this process, which is still implemented in this field of research. He conducted the first qualitative analysis on gaseous discharge and pave a path for future research [35].

1.3.1 EHD pumping

EHD pumping is about the interaction of fluids and electric fields [21], which results in a fluid pumping process induced by the electric field [37] or enhancement of heat transfer [38]. EHD mass and heat transfer are wanted in industries with restrictions and requirements regarding device operation conditions while a high heat or mass transfer rate

is desired [39, 40]. A good example of this application is in microgravity conditions in which an energy-efficient heat transfer mechanism is desired because the conventional

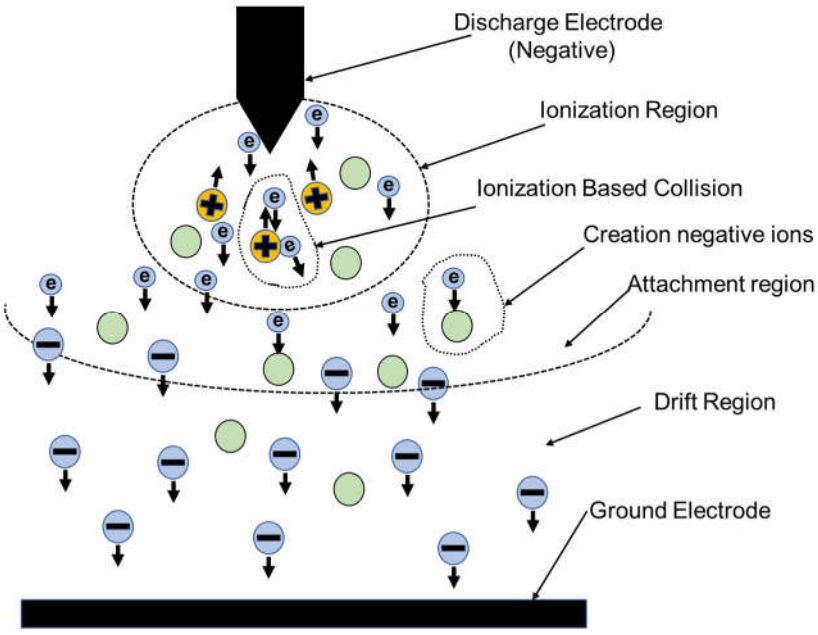

Figure 1-3 Negative corona discharge.

circulation pumps consume significantly higher power to provide the same transfer rate. In addition, the maintenance requirements for the mentioned method of heat or mass transfer are less, and they do not generate loud noises and mechanical vibrations. These advantages come from the fact that these systems do not implement any moving parts, and as a result, the vibration is eliminated. This gives the opportunity to implement these systems of heat/mass transfer in precise applications such as optical mirrors and high-power laser diodes, which require high precision in positioning.

Direct charge injection between the electrode-fluid interface is one of the most applied methods of free-charge generation. The electric field is applied between the sharp and the blunt electrodes, which are also known as the emitter and the collector, respectively. The electric field accelerates the free charges along its direction between the two opposite surfaces and creates a drag force by applying shear stress to the fluid medium. These EHD pumps are known as direct-ion injection or ion-drag pumps [41]. Setzer and Pickard have shown the experimental and theoretical viability of ion-drag pumps in their scientific reports [42, 43]. The experiments were initiated on oil as the transforming fluid, and velocities up to 10 cm/s were achieved using meshed electrodes. In a recent work by Bryan and Seyed-Yagoobi, higher velocities up to 33 cm/s were achieved [44]. Sharbaugh et al. [45], designed a pump with a 167 KVA distribution transformer, in order to improve convective cooling of the transformer but it only stayed operational for 500 hours since the collector electrode clogged the stream by accumulating the contaminations around it, dropping the pressure drastically. The main drawback of this method based on literature is that the electrical and thermophysical behavior of the medium fluid will be altered after a long time of operation, which leaves doubt about the reliability of this process for long-term applications [46]. It has been reported that the lifetime of a sharp electrode can be no more than 1 hour since the electrochemical processes will degrade the sharpness of the electrode and will reduce the efficiency of the process significantly [47].

1.4 Emulsion

Emulsions are an unstable mixture of two immiscible fluids, one of them being dispersed in the other one in the existence of a surface-active agent. Emulsion droplets display all of the unstable collides behavior, from Brownian motion to reversible phase transitions and irreversible transitions. They are made by shearing two phases resulting in the dispersing of one phase into the other [48]. The volume ratio of the droplet (water) to another phase (oil) may alter from near zero to almost one: in a highly concentrated emulsion, the structure is similar to the cellular structure of air-liquid foams, which sometimes are called bi-liquid foams. The mechanical properties and internal dynamics vary from sparse emulsion to dense emulsion. From diluted to highly concentrated, emulsions exhibit very different internal dynamics and mechanical properties. In a highly sparse emulsion, they behave like viscous Newtonian fluids when agitated by Brownian motion [49]. When the fraction increases and it reaches near 63% for monodisperse droplets, the internal dynamic is significantly limited, and emulsions behave as viscoelastic solids [50]. Simple direct emulsions are a mixture of oil droplets in water, and inverse emulsions are a mixture of water droplets in a continuous oil phase [51].

In general, the emulsion can be categorized into three types: water-in-oil (W/O) emulsion, oil-in-water (O/W) emulsion, and multiple emulsion. When water droplets are dispersed in a continuous oil phase, W/O emulsion is made. When oil droplets are dispersed in the continuous water phase, an O/W emulsion is made. Multiple-emulsion is a complicated

system, and it is made when either W/O or O/W emulsions are dispersed into another immiscible phase [52]. Multiple-emulsion also can be categorized into water-in-oil-in-water (W/O/W) emulsion and oil-in-water-in-oil (O/W/O) emulsion [53]. All kinds of emulsions can be either desired or problematic and depending on the application sometimes, we want to have emulsions, and sometimes we don't want to have emulsions. Emulsions find many applications from paints to cosmetic and drug delivery [54]. In oil industries, usually, a separation of two-phase is a goal, and different methods are used to break up emulsions.

1.4.1 Type of emulsions

The size of droplets in the continuous phase can be another way to categorize emulsions [55]. An emulsion is considered a macroemulsion if droplets are larger than 0.1 μm. These emulsions are generally thermodynamically unstable as the two phases willing to coalesce and separate to decrease their interfacial energies over time. However, by implementing the stabilization mechanisms, the rate of droplet coalescence decrease [56]. This category is very common, and most of the emulsions are in the form of a macro emulsion. Also, there is another group of emulsions, called microemulsions. This type of emulsions is made when two immiscible fluids exist, and emulsions are made because of the ultra-low interfacial energy. The droplets' size is less than 100 nm in microemulsions, and they are believed as thermodynamically stable mixtures. Microemulsions are different from macro emulsions by considering stability and formation [57].

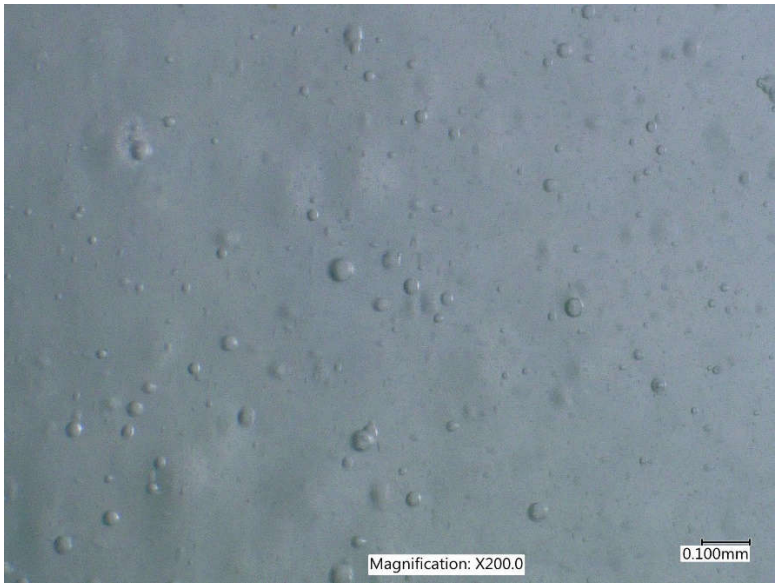

Figure 1-4 Oil in water macroemulsion under an optical microscope.

1.4.2 Formation of emulsions

The two most important factors to bring oil and water together and make emulsions are the presence of active-surface agents and an adequate amount of mixing. In general, a more stable emulsion corresponds to a smaller size, and the smaller size corresponds to the larger shear rate. [58]. Also, the properties and concentration of the emulsifying agent have a major role to dictate the type and stability of emulsions.

1.4.3 Stability of oil-water emulsions

Emulsions are considered unstable systems from a thermodynamic perspective because of a tendency to minimize interfacial energy in the interface of continuous and disperse phases. [59]. However, most emulsions show kinetic stability in their shelf life. It is believed that the interaction of the surface-active agent in the interface of the two phases is responsible for emulsions stability. [60]. The formation of an interfacial layer between the small size droplets of water and oil causes kinetic stability [61]. The presence of surfactant and its consequence on electrostatic and steric forces improves the stability of emulsions [62].

The most straightforward method to find out the stability of an emulsion is a bottle test [63]. This method is simply based on the procedure, including diluting emulsion with solvent, adding surfactant, agitation, and observing phase separation by time in controlled temperature [64]. Another parameter that also can indirectly be used to measure stability is Zeta potential. It can be measured by diluting the emulsion and observe electrophoretic mobility on ions. Zeta potential value depends on the physicochemical property of the disperse phase. It is believed that the Zeta potential larger than ±30 mV is sufficient enough to ensure the physical stability of the nanoemulsion [65]. Also, droplets size can be considered as stability of emulsions; it is believed that the thermal collision force acting on continuous phase molecules creates the Brownian motion, which prevents smaller droplets from settling [66].

1.4.4 Droplet size distribution in emulsions

Droplet size distribution can be considered as one of the most important characteristics of emulsion [67]. Also, it can be used as an alternative way to measure the stability of the emulsion. The most common method to measuring the size distribution of droplets is the detection of light scattering, which is a wildly-used technique since it was introduced by John Tyndall in 1868 [68]. In a dynamic light-scattering (DLS) method, the laser light is emitted toward droplets and encounters them. As a result, the incident light scatters in all directions, and scattering magnitude is monitored by a detector. The recorded incident light will go through a concept called Doppler broadening as the droplets are in continuous motion in continuous phase [69]. The scattered light can be mutually destructive phases and cancel each other, or they can be mutually constructive phases to create a detectable signal. Also, some different algorithms and approaches can be used to analyze the data to determine the size and uniformity of the emulsions [70].

1.5 Coalescence in oil and gas industries

It is highly desirable to have a separation of water and crude oil in the stabilized emulsion phase in the oil and gas industries. Cost of transportation water with oil, deactivation of catalysts, increased operation cost, and corrosion of equipment, machines, pipelines, etc., are adverse results of the existing water in oil, which makes dehydration a significantly crucial step in production.

Increased pumping, surface corrosion, eroded pipelines, and equipment are some of the costly processes in the petroleum industry that are resulted from emulsified water in crude oil [71]. Crude oil prices can directly be impacted by emulsion treatment leading to significant research efforts for reducing the cost of this treatment [72-74]. Electrostatic, hydrodynamic, or Brownian processes are utilized to induce droplet attraction alongside chemical and thermal liquid treatments. However, the chemical treatment processes (such as adding into stimulation and remediation crude oil [75]) are criticized due to the high precaution needed in work, their chemical complexity, their negative effects on any system, and the fact that they produce waste materials known as "rag" which are hard to deal with (e.g. PO-EO and EGMBE which are not environmentally acceptable). On the other hand, once accepted thermal treatments, are now scrutinized due to the fact that the heat applied to the crude oil will change its properties and the quality of low carbon and volatile chain components or fractions of the extracted oil [76]. The most efficient process of emulsion resolution is electrostatic coalescence, which provides acceptable environmental impacts, energy efficiency, and economic output. This process shows increasing potential in the destabilization of the emulsions and breaking and coalescence of the water droplets in the emulsions.

When two or more droplets in an irreversible thermodynamic process are gathered together in the form of a larger droplet, coalescence takes place. In other words, it is successive completion of three distinct sub-processes, which are as following [77]: 1) External forces (i.e., gravity, etc.) are important factors in colliding droplets. 2) The thinning of the

interstitial film of the liquid is the other affecting parameter in order to form a continuous phase of the material. As the separation in interfacial decreases to less than 1000˚ A, some other surfaces and electrostatic forces become in charge of altering the drainage mechanics. These forces are mostly known as electric double layer repulsion and Van der Waals [78-80]. In the presence of surfactants and with an increase in bulk viscosity, the thinning rate increases significantly, due to increasing electrostatic interaction and increasing shear stress respectively which is the indicator of the collision [81]. 3) Marginal regeneration and Marangoni behavior oppose the elimination of the liquid inside the thin film and may result in a non-steady configuration. In this condition, the critical thickness of the film, which is in the order of tens of nanometers, is reached, and any external disturbance in mechanical or thermal modes can result in the breakage of the film and making the droplets coalesce. This is a necessary process to form coalescence by breakage fluid film [81, 82].

1.5.1 Electrocoalescence

The most common practice of water separation from crude oil production in oil and gas industries is to apply a high electric/electrostatic field to the flow of emulsion and coalesce the water droplets [83, 84]. Some researchers utilized the application of an electrostatic field to organic liquids in order to extract solvents from the liquid media by eliminating the aqueous droplets [85]. An electric field can cause breakage of emulsion with the coalescence of droplets in low and high field strengths. In high electric fields, the breakage is quite stable while in low strength, the separation takes place in the shape of a chain of

water droplets, and after removal of the field, the droplets return to their normal form in the emulsion [86, 87]. In addition, differential sedimentation and Brownian motion can result in slight coalescence, which is negligible relative to the coalescence that takes place in the presence of the electrostatic field [88].

It is assumed that the droplets get polarized or charged under the extremely high external electric field and agglomerate to the point that they coalesce. The coalescence happens after the application of the electric field in aqueous/oil emulsions, and the aqueous droplets will get closer to each other to the point that they stick to one another. However, there is a thin film of oil between the adjacent aqueous droplets that defines the stability of the emulsion. It is crucial to break this thin film to let the droplets gather together and form a larger droplet, finally separating the aqueous phase [89]. The stability of the emulsion can be quantitatively and qualitatively investigated by several methods such as differential scanning calorimetry (DSC) (particularly for double emulsion) [90], bottle test, turbidity measurement, and time-domain dielectric spectroscopy [91]. Power consumption is the key to assessing the efficiency of electrical processes, and it directly relates to the bridging of electrodes and the electrical conductivity of the medium used in the process. In the case of completely nonconductive, the very small current drawn to the medium is negligible compared to the high energy-consuming processes [92].

The design of new coalescence systems based on the droplet-droplet concept is getting the greatest attention in the field of separation [93]. Good practices in order to get a more accurate understanding of the mechanism of coalescence can be achieved via

experimentally investigating a water-oil emulsion. By doing this experiment, one can find out the optimum electric field and electrode geometry to obtain the best results [94]. In the following sections, different aspects of the electric field, the droplet interface, and the droplet-droplet coalescence are reviewed.

1.5.1.1 Mechanisms and models of electrocoalescence

Based on the fact that any electric field, regardless of its strength, can separate water droplets from a water-oil mixture, several approaches are introduced such as electrophoresis, dielectrophoresis, electro fining, dipole coalescence, a random collision of droplets, intermolecular bond formation, and formation of droplets [95-98]. It is believed that the main mechanism of separation is based on the applied electric field, the geometry of the electrodes, and the portion of the dispersed phase in the mixture/emulsion. Waterman introduced two water droplet electrocoalescence approaches, which are electro fining and dipole-dipole coalescence. The former includes collision of charged droplets-different sized droplets in a DC electric field, dielectrophoresis, and dipole coalescence [99].

In the case of an AC electric field, Galvin found out that the dominant phenomenon is the formation of droplet pairs instead of a chain of droplets, and the droplet-droplet speed increases while droplet-droplet separation decreases. In addition, he did not observe any film resistance in droplet-droplet coalescence, but before coalescence, the droplets were deformed [100]. Since the coalescing droplets prefer to move at the same velocity but in different directions, electrophoresis cannot be a significant mechanism in this situation.

The gravitational separation for the coalesced droplets can be calculated from the equation (1-3), which is governed by the Navier-Stokes equation, and the sedimentation velocity can be found by:

$$v = \frac{(2a^2(\rho_W - \rho_C)g)}{9\eta} \tag{1-3}$$

where a is the droplet radius, ρ_W is the droplet density, ρ_C is the continuous phase density, η is the dynamic fluid viscosity, and g is the gravitational constant. A water droplet of 1 mm radius will settle through a 1-centimeter column of silicone oil with a viscosity of 100 cst in about 13 seconds, a 100 μm water droplet will take about 37 hours, and a 100 nm droplet will take about 42 years.

Based on equation (1-3), it can be concluded that decreasing the continuous phase viscosity (affected by temperature), increasing the phase density difference (affected by diluents), and increasing the droplet size, will result in the improvement of gravitational settling [101]. Gathering all these parameters, it is obvious that the separation efficiency is influenced the most by the applied external electric field. Equation (1-3) is simplified and should only be used for single-particle approaches neglecting non-slip boundary conditions and the effect of any adjacent wall. All in all, the proportion of velocity radius of the droplet is a nonlinear second-order which emphasizes the importance of coalescence before phase separation.

1.5.1.2 Three-stage mechanisms of coalescence

The coalescence of immiscible aqueous droplets in a liquid phase occurs through different steps. At first, the droplets get close to each other while a thin film of oil is separating them after the initial contact. In the second stage, film thinning (film degradation) takes place, and the thickness of the separating layer between the droplets decreases to the point that they can merge [98, 102-104]. In the final stage, the thin film is in the critical thickness, and a mechanical or thermal disturbance causes film elimination, which results in a coalescence phenomenon in aqueous droplets [54]. Although the discussion shows the main reasons for film thinning, other researchers have shown that other parameters are affecting this process, which could be surface diffusion of soluble surfactants in the bulk phase [80, 105-107].

1.5.1.3 Film thinning of a continuous phase

Thinning and breaking are the two important factors in determining the lifetime of the water-oil mixture and how the oil interfacial film is withstanding the situation. As the thickness of the film gets close to 1000° A, other surface forces such as Van der Waals and double-layer repulsion start affecting the thinning rate by increasing and decreasing the drainage rate, respectively [54]. With the application of an external stimulus, the metastable condition of the thin film becomes unstable, and the metastable condition forms when the Van der Waals, double-layer repulsion, and border suction attraction forces are balanced.

Film drainage causes droplet-interface coalescence, and it can be improved by forces induced electrically at the liquid-liquid interface [108]. Droplet-droplet coalescence happens when the two adjacent droplets are close enough (below or at the critical distance from each other), which results in degradation and elimination of the oil film due to enough energy of the droplets breaking the dielectric resistance in the oil film [109].

1.5.2 Dipole-dipole coalescence

Brownian motion, flocculation, sedimentation, and electrophoresis, are used to bring the droplets together to make the dipole coalescence happen [110]. Williams, Bailes, and Waterman have reported that in the case of AC and DC electric fields, these forces are the main reasons for droplet-droplet coalescence [88, 99, 111]. According to Williams, dipole coalescence and migratory coalescence (electrophoretic, which applies to the charged droplets) are combined to form electrostatic coalescence. The dielectrophoretic attractive force between two water droplets forms their polarization in an electric field, inducing dipole coalescence [88]. Based on the charge polarity of materials, electrophoresis moves the droplets of water in the opposite direction of the electric field [112]. A different sign of charges on aqueous droplets can be provided in the presence of an external electric field [109]. The two adjacent droplets can change the potential and velocity fields around the neighboring droplets, which causes a hydrodynamic resistance on water droplets resulting in the flow of droplets around one another. The other force, known as Van der Waals (attraction and repulsion between atoms), pulls the droplets close to each other if the initial

distance is low enough [109]. Relative to the external electric field, reorientation of the dipoles will cause aqueous droplets in dielectric liquid to be polarized [96, 113].

1.5.2.1 Dipole-dipole interaction

Water droplets in emulsions subjected to an electric field are polarized and become dipoles when positive and negative charges are induced at two polar ends. Those dipoles are aligned in the direction of the electric field. Two water droplets attract each other when two opposite charged ends are close together. This is the force of the interaction between two water droplets. It is believed that this interaction is the main cause of coalescence in most of the electrocoalescence process using either the AC or DC electric fields. Also, droplets may repel each other if the sign of the charges in the nearest ends agree together.

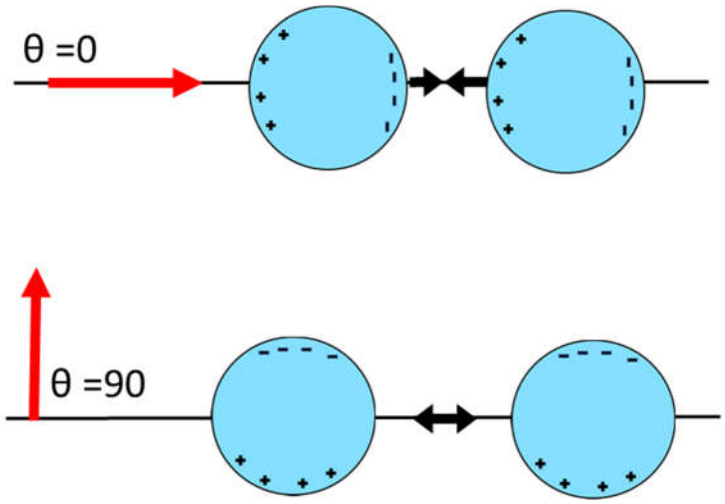

Figure 1-5 Two water droplets exposed to an electric field.

The interaction force between two droplets can be found from the following equations, which include two components in the radial and tangent direction [114].

$$F_d = {K_c}^2 \frac{-6\pi\epsilon_0\epsilon_c a_i^3 a_j^3 E^2}{d^4}(1 + 3COS(2\theta)) \quad (1\text{-}4)$$

$$F_\theta = {K_c}^2 \frac{-12\pi\epsilon_0\epsilon_c a_i^3 a_j^3 E^2}{d^4}(sin(2\theta)) \quad (1\text{-}5)$$

where$a$ is a water droplets radius, ϵ_0 is the permittivity of free space, ϵ_c is the dielectric constant of the continuous phase, K_c is the Clausius-Mossotti factor defined as $\frac{(\epsilon_d - \epsilon_c)}{\epsilon_d + 2\epsilon_c}$, ϵ_d is the dielectric constant of the disperse phase, *d* is the distance between the center of the droplet, and **E** is an external electric field [115].

Two water droplets attract each other if $(1 + 3COS(2\theta)) > 0$. Therefore, $\theta < 54.7°$ or $\theta > 125.3°$ [116].

Dipole coalescence events originate from the dielectrophoretic force of attraction between two neighbor water droplets due to polarization of the water droplets. When water droplets are exposed to a strong electric field, an electric dipole is induced in them. The dipole moment is given by:

$$\boldsymbol{\mu} = \nu \boldsymbol{P} \quad (1\text{-}6)$$

where $\boldsymbol{P}$ is a polarization or moment per unit volume and ν is a volume. For spherical droplet $\nu = \frac{4}{3}\pi a^3$ and $\boldsymbol{P} = (\epsilon_d - \epsilon_c)\epsilon_0 \boldsymbol{E_{in}}$, where a is the droplet radius and $\boldsymbol{E_{in}}$ is the internal field in the sphere that can be found from: $\boldsymbol{E_{in}} = \frac{3\epsilon_c}{\epsilon_d + 2\epsilon_c}\boldsymbol{E}$. $\boldsymbol{E}$ is an external electric

field. By substituting into equation (1-6) the dipole moment for each water droplet can be obtained as:

$$\boldsymbol{\mu} = 4\pi a_i^3 \epsilon_0 \epsilon_c K_c \boldsymbol{E} \tag{1-7}$$

where K_c is the Clausius-Mossotti factor defined as $\frac{(\epsilon_d - \epsilon_c)}{\epsilon_d + 2\epsilon_c}$.

DDI has been extensively investigated, and several models have been introduced to explain the electric force between the water droplets. The interaction energy between two water droplet dipoles separated by a distance (d) is given by [117]:

$$E_{\mu_{i,j}} = \frac{\boldsymbol{d}_{ij}{}^2 \boldsymbol{\mu}_i . \boldsymbol{\mu}_j - 3(\boldsymbol{\mu}_i . \boldsymbol{d}_{ij})(\boldsymbol{\mu}_j . \boldsymbol{d}_{ji})}{4\pi\epsilon_0 \epsilon_c \boldsymbol{d}_{ij}{}^5} \tag{1-8}$$

By substituting $\boldsymbol{\mu}$ from equation (1-7) and by some mathematical arrangement, equation (1-8) becomes:

$$E_{\mu_{ij}} = \frac{-4\pi a_i^3 a_j^3 \epsilon_0 \epsilon_c K_c^2 |\mathbf{E}_i||\mathbf{E}_j|}{|\boldsymbol{d}_{ij}{}^3|} (\cos(\theta_i + \theta_j) + \cos(\theta_i)\cos(\theta_j) \tag{1-9}$$

The force acting between two water droplets has two components, one in the radial direction and the other one is in the transverse direction and that can be found by differentiating the $E_{\mu_{ij}}$ from equation (1-9):

$$\boldsymbol{F}_{ij} = \nabla(E_{\mu_{ij}}) \tag{1-10}$$

$$\boldsymbol{F}_{d_{ij}} = -\frac{\partial E_{\mu_{ij}}}{\partial d_{ij}} = \frac{-6\pi a_i^3 a_j^3 \epsilon_0 \epsilon_c K_c^2 |\mathbf{E}_i||\mathbf{E}_j|}{|\boldsymbol{d}_{ij}{}^4|} \left(3\cos(\theta_i + \theta_j) + \cos(\theta_i - \theta_j)\right) \underset{d}{\rightarrow} \tag{1-11}$$

$$\boldsymbol{F}_{\theta_{ij}} = -\frac{\partial E_{\mu_{ij}}}{\partial \theta_{i,j}} = \frac{12\pi a_i^3 a_j^3 \epsilon_0 \epsilon_c K_c^2 |\mathbf{E}_i||\mathbf{E}_j|}{|\boldsymbol{d}_{ij}{}^3|} \left((\sin(\theta_i + \theta_j)\right) \underset{\theta}{\rightarrow} \tag{1-12}$$

The negative value of the forces shows the attraction between the water droplets. In addition, these equations can be applied to the uniform electric field (e.g. $\mathbf{E}_i = \mathbf{E}_j \; and \; \theta_i = \theta_j$) which agree with the previously introduced models in equations (1-5) and (1-4) [118].

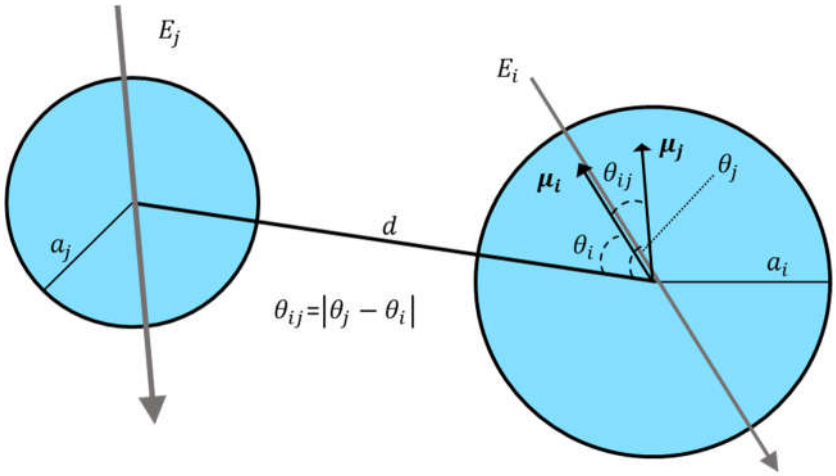

Figure 1-6 Two water droplets under a non-uniform electric field. $\boldsymbol{E_i}$ and $\boldsymbol{E_j}$ are the electric field components in the center of the water droplets and $\boldsymbol{\mu_i}$, $\boldsymbol{\mu_j}$ are the induced dipoles as an effect of the polarization. θ_i and θ_j are the angles between $\boldsymbol{\mu_i}$ and $\boldsymbol{\mu_j}$ with the distance vector between center of two water droplets (d), respectively. Charges are induced in both water droplets, making a dipole momentum. The DDI forces act between the droplets causing their mutual attraction. Theoretically, this attraction force follows equations (1-11) and (1-12). It is believed that these forces are the primary cause of electrocoalescence in emulsions.

1.5.2.2 Electrophoresis

The movement of particles/droplets due to an external electric field in a stationary fluid is called electrophoresis. The applied charge to the droplets/particles, fluid around them, or both of them causes a movement that is known as electrophoretic mobility, which is

measured by particle velocity regarding the strength of the electric field applied to it [99, 119].

The electrophoresis (EP) force can be found from Coulomb 'law (**Figure 1-6**), and it is equal to **E**

$$\mathbf{F} = \mathbf{E}q \tag{1-13}$$

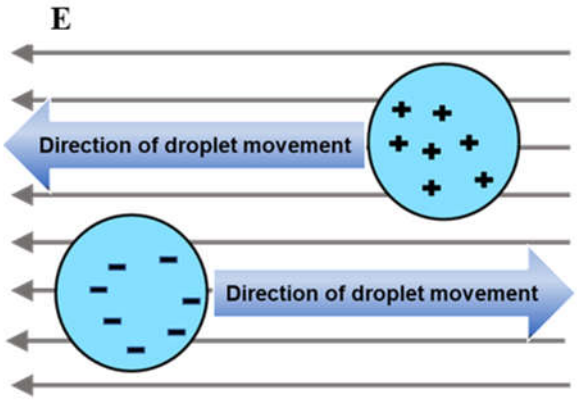

Figure 1-7 Effect of an electric field on charged water droplets.

The interfacial surface between the liquids can gain a net surface charge which forms an electrical double layer, given by:

$$q_d = 4\pi a^2 \zeta \sqrt{\frac{\varepsilon_c \sigma_c}{\Delta}} \tag{1-14}$$

where ζ is the zeta potential, Δ coefficient of diffusion, ε_c dielectric constant, and σ_c is the conductivity of the continuous phase. Also, water droplets touching any electrode surface receive a charge which is given by:

$$q = 6.6\pi\varepsilon_c a^2 |\boldsymbol{E}| \tag{1-15}$$

where a is the radius of the water droplet and $\boldsymbol{E}$ is the strength of the electric field. Water droplets traveling the gap between the electrodes to reach the opposite electrode as an effect of Coulombic forces, which is electrophoreses (EP) in nature.

Water droplets travel the gap between the electrodes to reach the opposite electrode as an effect of Coulombic forces. The force acting between the water droplets can be found from the following equation [120]:

$$\mathbf{F_{ij}} = \left(\frac{q_i q_j}{4\pi\varepsilon_c\varepsilon_0 d^2}\right)\vec{d} \qquad (1-16)$$

By substituting equation (1-15) in (1-16), the attraction force in non-uniform electric field can be obtained as:

$$\mathbf{F_{ij}} = \left(\frac{10.9\pi\varepsilon_c\varepsilon_0 {a_i}^2 {a_j}^2 |\mathbf{E_i}||\mathbf{E_j}|}{d^2}\right)\vec{d} \qquad (1-17)$$

1.5.2.3 Dielectrophoresis (DEP)

The other type of movement in particles/droplets in a fluid is known as dielectrophoresis, which is applied to the uncharged particles/droplets moving them in the electric field direction non-uniformly [112, 121]. The higher permittivity of the particles/droplets relative to that of the continuous phase will result in the movement of the particles in the electric field direction toward stronger fields. The particles/droplets do not need to be charged since the motion force is induced by polar droplets in a non-uniform electric field. All the dipoles have equal positive-negative charges, and the electric fields are aligned with these dipoles [122]. As a basic physical fact, the dipoles are aligned in a way that one end

of the dipole is facing the weaker field while the other end is the opposite. This drives the dipoles in the direction of the field toward stronger regions (**Figure** 1-7). If the direction of the electric field is reversed, this just increases the ability of the dipole to move in the same direction since the proportion of the dipole and the electric field is that the moving force is dependent on the square of field strength [112, 121]. Although the mentioned theory is apparent, it is important to note that dipole coalescence takes place due to dielectrophoresis [123]. In order to clarify this phenomenon, a pair of water droplets in oil will tend to attract each other and move toward stronger fields in between those droplets. This theory remains valid even in the case of perturbation generation in electric fields due to the presence of water droplets, i.e., spatially uniform electric fields [112, 124, 125].

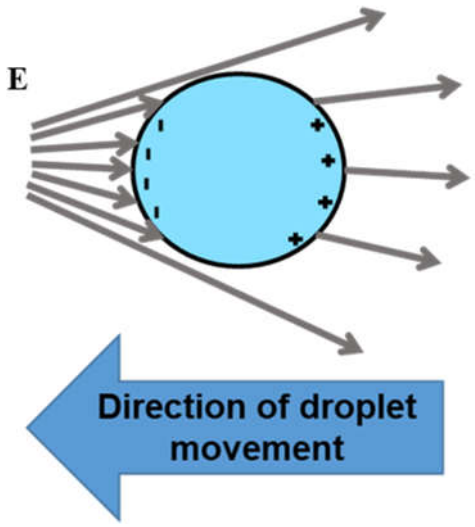

Figure 1-8 Water droplet exposed to a non-uniform electric field and the dielectrophoretic force moves it in the direction of the stronger electric field

The motion of matter due to the polarization effect in a non-uniform electric field is called DEP. The material with the higher dielectric constant moves toward the higher intensity of electric field, unlike EP, which depends on charged particles. Any induced or permanent dipole has a limited charge in it; when exposed to an electric field water droplet aligns with the electric field, but in the non-uniform electric field, one side of the dipole is always exposed to the higher electric field rather than the other side. In this case, the net force is not zero and the dipole moves towards the region having a higher electric field. Also, it should be noted that the DEP force does not depend on the direction of the electric field and the dipole moves in the same direction even if the direction of the field is reversed. The net force induced by DEP is given by:

$$\boldsymbol{F}_e = 2\pi a^3 \epsilon_c \epsilon_0 K_c \nabla \boldsymbol{E}^2 \quad (1\text{-}18)$$

DEP forces move the water droplets toward the stronger electric field in the center in a collective way and increase the chance of the coalescence by increasing the chances of collision between water droplets (migratory coalescence) and enhance the effect of the DDI, due to decreasing the distance between water droplets. DEP can significantly enhance the performance of coalescer, especially in dilute emulsions. Also, the corona setup needs just one electrode in direct contact with liquid, due to the contactless nature of the gas discharge resulting in decreasing the effect of adhesion disruption.

Chapter 2

2 Instabilities of bulk dielectric fluids under corona-initiated charge injection

2.1 Abstract

Electrohydrodynamic (EHD) flow induced in dielectric fluids by charge injection is capable of producing convective instabilities accompanied by surface deformation of fluids. This work presents the results of experimental observations of the EHD flow induced in bulk dielectric liquid layers using corona discharge. A method for deformation analysis of surface liquid is presented and used to characterize the convective instabilities and bulk deformations formed within the fluid. The governing liquid properties for the deformations are discussed, indicating the vital role of surface tension and viscosity. Critical voltages at which rapid transformation of the liquid's deformation occurs are identified and discussed. Consideration is also given to the potential application of the EHD flow as an air-wave type EHD pump, including analyses of pumping performance and its

governing parameters. The liquid layer thickness is shown to be a dominant parameter in the efficacy of such proposed pump designs.

2.2 Introduction

Dielectric liquids are widely used in different applications such as energy industries and pharmaceutical products. Although many of these applications do not directly interact with the dielectric properties of these materials, it is possible to utilize these unique properties in order to enhance the existing applications or create application-specific properties. Dielectric liquids are generally used for the manipulation of material through their electrical properties which are widely known to be a subcategory of electrohydrodynamics (EHD) [2]. EHD force is mainly utilized in the form of pumps that operate based on ion drag. In these mechanisms, a non-homogeneous electric field produces forces that are exerted to a fluid with a space charge density, leading to the process of pumping. This concept is thoroughly explained by Melcher and it could be summarized in the following equation [126]:

$$\mathbf{F} = q\mathbf{E} + \mathbf{P}\cdot\nabla E - \frac{1}{2}E^2\nabla\varepsilon + \nabla\left(\frac{1}{2}\rho\frac{\partial\varepsilon}{\partial\rho}E^2\right) \quad (2\text{-}1)$$

where P is the polarization vector, ε is the permittivity of the fluid, and ρ is the fluid density. The first term in equation (2-1) is from the coulombic force acting on the space charge captured by the liquid and is the dominant term in most of the EHD pumps. Besides the first term which represents the columbic force, other terms introduce other forces that are comparatively negligible in calculating the acting force in EHD pumps. These forces are

polarization, dielectric, and electro-strictive forces which are shown in the second, third, and the last part of the equation (2-1), respectively.

Injection, induction, and conduction EHD pumps are the three main categories of pumps for the generation of pressure differentials and fluid acceleration [127, 128]. Injection pumping is characterized by momentum transfer from injected unipolar ions in an electric field to the surrounding fluid [42]. However, due to its low efficiency, limited pressure generation, and issues with electrode deterioration, this type of pump found few practical applications [21]. Although these pumps are not efficient, they are useful in applications such as microfluidics where additional heat and mass transfer are desired without the use of moving parts. Induction pumping sometimes referred to as traveling wave-induced electroconvection, is a non-contact method that relies on the induction of charges to a liquid surface from electric conductivity gradients induced via an AC traveling wave [21, 129]. Conduction pumps utilize electric fields to produce regions of dissociated ions in a liquid near the electrodes, inducing fluid motion [21]. Induction and conduction pumping methods have attracted more interest and applications due to their higher working efficiency.

A special category of injection EHD pumps is the air-wave type where the injected ions are produced by a corona discharge, perpendicular to the top surface of the fluid [130]. Corona discharge is the drift of unipolar charges from an ionization region produced by large electric field gradients [131], often created by applying large potentials to a sharp electrode tip. After placing the liquid between the sharp tip and the ground electrode,

charges can then be injected to the surface of the liquid. This ion impingement causes a fluid flow toward the ground electrode. Previous studies on corona discharge have made numerous observations on the behavior of liquids under unipolar discharge including the types of existing instabilities, the onset voltages, currents, and the governing electrical properties of the liquids [132-135]. While these studies have discussed the phenomenon, they are often limited to theoretical formulations and to discussions of surface deformation patterning of thin liquids. However, there has not been any study extending these theories to EHD flow in thicker dielectric layers. [136], has investigated the pressure and deformation on the surface of a thick water layer, when exposed to the corona discharge. In their work, pressure and surface deformations along the liquid surface were measured and were correlated to the ionic wind created by the corona discharge. Another investigation of the corona-induced EHD flow can be seen in the work of Mahmoudi, et al. [137], where a droplet of a dielectric liquid was spread across a surface after exposure to the corona discharge revealing an increased wetting potential that the corona discharge can induce on dielectric fluids.

Analysis of the fluid velocity profiles and current distributions for air-wave EHD pumps have been studied for various electrode geometries and applied voltages [130]. Experiments using tip-plane configuration have shown that by combining an air-wire and a sloped electrode, dielectric fluids can be pumped out of a containment vessel by an ionic wind [138, 139] and current flow is concentrated at the air-liquid interface [130, 140]. Other enhancements to the EHD pumping have been suggested utilizing liquid properties

(i.e. viscosity), electrode geometry, and controlled electrical conductivity of the electrodes (electrically insulating or conductive coatings) [141]. However, these studies have not investigated vertical pumping of the dielectric liquids and their efficiency in the vertical configuration.

Here, we investigate the effects of corona discharge on bulk dielectric liquids from new aspects. The ions released from a corona discharge can cause simultaneous heat and mass transfer in a dielectric medium interface upon impact. Most of the previous studies on ion injection and pumping abilities of corona discharge are based on ion dragging with no mention of pumping within vertical configurations. In addition, previous studies have been mostly theoretical without providing experimental proofs and visualizations, focusing only on the behavior of the EHD phenomenon in a thin liquid layer. In this work, we focus on the forcing behavior of the discharge as well as the scale and formation of a liquid movement that is induced by the high voltage discharge. Attention is given to the power requirements as well as the effect of various liquid properties including viscosity, electrical conductivity, and surface tension on the pumping performance, characterized by an observed change in the liquid layer thickness. To the best of our knowledge, this work is the first in-depth experimental analysis of the pumping performance of corona injection-induced EHD flow in bulk dielectric liquids.

2.3 Experimental Setup

A tabletop setup was designed to expose dielectric liquids to corona discharge. **Figure 2-1** (A) Schematic of the experimental shows the schematic of the setup consisted of three main systems: a high-voltage generating system tied to a super fine tungsten needle as a corona-generating electrode, a mechanical apparatus designed to hold a grounding electrode in contact with a dielectric liquid, and a measuring system incorporating current measuring equipment. Two cameras are also incorporated in the setup for real-time imaging. A high-speed camera (Olympus TR i-speed) capable of up to 10,000 fps was used in combination with a macro photography lens to observe the rapid changes in liquid behavior during tests from the side of the apparatus. A smaller Nikon D5500 was remotely operated to take video of the top view of the liquid surface during the tests. Voltages and currents were actively monitored and recorded using the built-in measurement system of the TREK amplifier coupled to a Keithley 2100 digital multimeter. The high-voltage system utilizes a ±10 kV TREK Model 10/10B high-voltage amplifier connected to a bench-top DC power supply (BK 1698). Due to limitations in the power supply's accuracy, the smallest possible voltage increment at the electrode was 100 V. While capable of outputting both AC and negative voltages, only positive voltages were used for the results presented in this work. The high slew-rate (350V/μs) of the amplifier made it ideal for measuring the response time of the liquid layers.

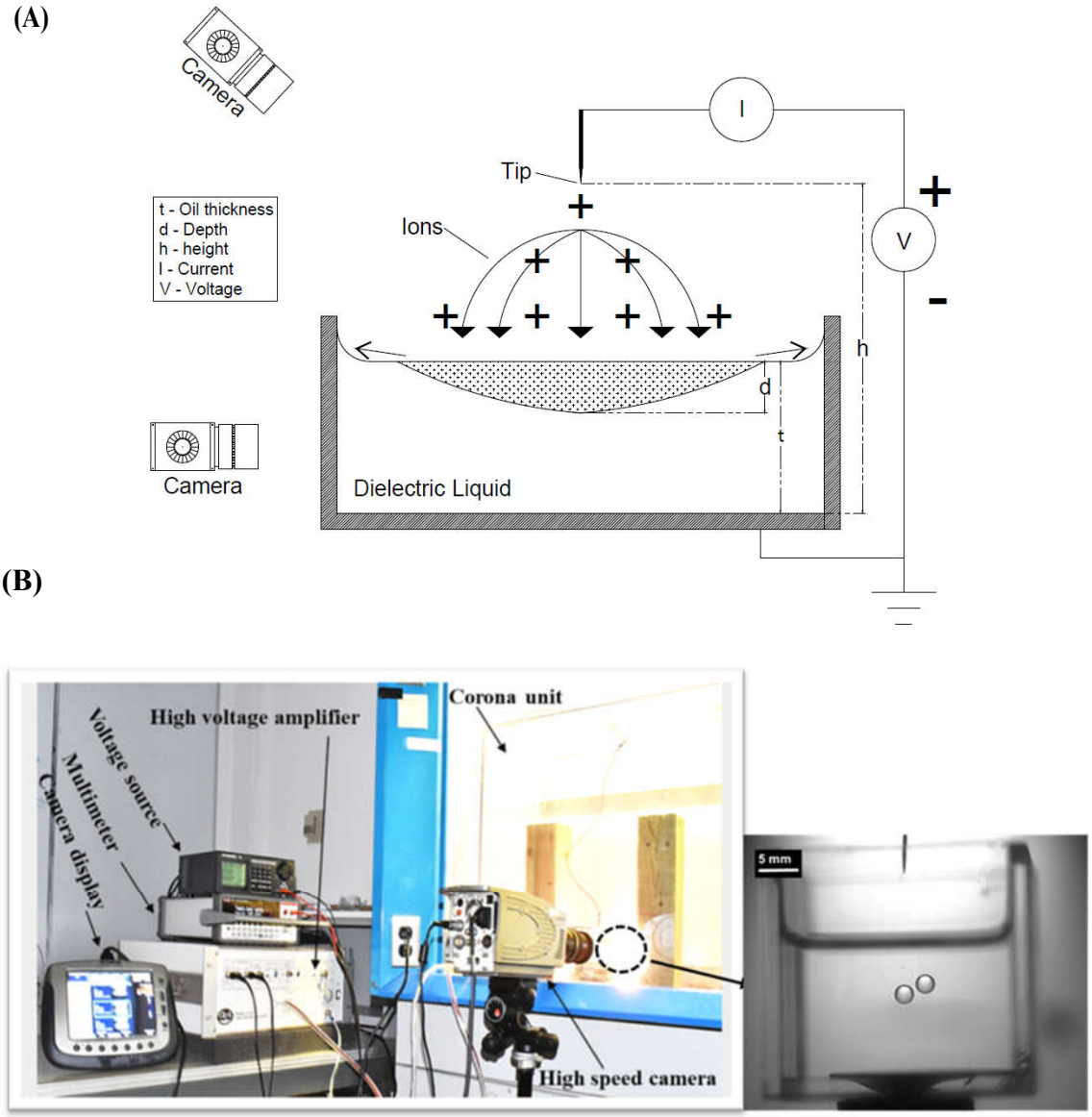

Figure 2-1 (A) Schematic of the experimental setup illustrating the formation of an ionic wind from a sharp needle electrode connected to a high voltage amplifier. The high electric field gradients near the tip result in localized ionization of air. For positive voltage application, the ions produced by these large electric fields will begin to drift towards the ground electrode below. As they move through the air, they are continually acted upon by the electric fields in the air causing acceleration of ions and their surrounding air, resulting in the formation of the ionic wind. When these charges hit a non-conductive fluid, they become trapped and form space charges. These space charges then interact with the electric

field producing motion within the bulk fluid in turn creating large surface deformations. Information is collected on this behavior using a pair of cameras and an ammeter in order to characterize these complex formations. Depth, d, represents how far the liquid surface has moved relative to its initial thickness, t, during tests. The height of the needle, h, was adjusted by a laboratory lift, to which the container was fixed. **(B)** Experimental setup. A high voltage amplifier, DC power supply, multimeter, high-speed camera, super fine tungsten needle, large quartz cell, and mechanical apparatus. Water droplets were dispersed from the top surface into the test cell.

The apparatus holding both the high-voltage needle and the grounding electrode was encapsulated in a transparent plexiglass box to prevent dangerous interactions with the needle. The grounding electrode was a 1-inch copper disk fixed to the bottom of a large cubic quartz cuvette. The ground electrode was slightly offset to improve the viewing angles of the top surface of liquids as deformations are localized above the grounding electrode. Other qualitative tests were performed with larger grounding electrodes. The tungsten needle electrode was fixed while the liquid containing cuvette was adjusted vertically during the tests. Tungsten was used as the needle electrode to reduce damage and wear to the tip. The tip was routinely examined and if any discoloration observed, polishing with a liquid metal polish (Brasso) followed by thorough washing with DI water and Isopropanol was performed. If any variations in voltage readings appeared before each experiment, the needle electrode was polished using the above procedure. Regardless of any observed variation, the tungsten needle was polished weekly in order to make sure that the tip is in a good shape and the process conditions are identical during all the experiments.

The tested silicone oils were obtained from MicroLubrol (50, 100, and 350 cst) and HUDY (3,000 cst). Castor oil was obtained from Sigma Aldrich. Approximate liquid properties are given in **Table** 2-1 Oil properties. Measurement of the electrical conductivity

was attempted with a rudimentary setup using standard 4 mm electrophoresis cuvettes as test cells. The conductivity for both the castor and silicone oil was confirmed to be close the expected value (1×10^{-13} – 1×10^{-12} S/m respectively).

2.4 Methodology

Since most of the data captured over the course of the experiments was in the form of videos, a simple and efficient method for analyzing the results had to be devised. To obtain how the deformation's size changed during experiments, a process involving the creation of thresholds was devised using an image processing software ImageJ. This process is shown in **Figure** 2-2. Successful implementation of this procedure required consistent and sharp contrast between the background and the oil deformation. In addition, any anomalies in the video that might be caused by light fluctuations or bubbles in the liquid were edited out after thresholding was complete, in order to generate accurate results. Post-processing was then performed to analyze the effect of the magnitude of the voltage, the rate of response, and changes in oil layer thickness through a similar process.

In addition, tracking of internal fluid motion using the ImageJ plugin TrackMate was also performed. It was also possible to produce contours of the surface deformations from the side and below in the hopes of comparing current deformation results to previous experiments and to eventually use the contour to perform a more rigorous theoretical analysis of the acting forces and fluid dynamics. However, both methods required

significant post-processing to highlight only the desired contours. These methods were thus not pursued in this study.

Analysis of the liquid's edge height (top of meniscus) was performed to determine the change in oil height due to exposure to corona discharge. It is assumed that this change in oil height is repeated around the edge of the container and, thus, marks the volume displaced by the discharge process.

2.5 Results

Impact of corona discharge on bulk dielectric liquids is investigated in two sets of studies. First, the effect of the dielectric liquid's thickness on the EHD response of the system was studied. To this end, the liquid thickness was varied from 1 mm to 10 mm for a constant electrode needle height, h = 15 mm. Prior, qualitative tests were performed to measure the effect of needle height on the corona discharge characteristics. **Figure** 2-3 shows that when there is no oil layer between the needle and the ground, the I-V response follows that of standard Townsend Discharge, which expresses a relationship between current and voltage for a corona discharge in the equation (1-2)[142]:

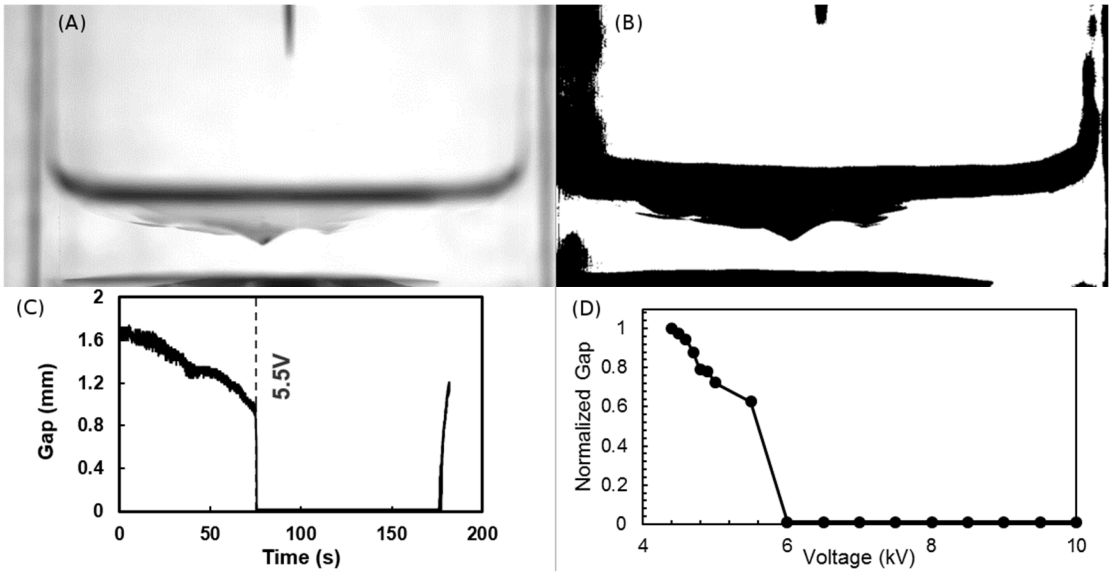

Figure 2-2 The image analysis processing method used to convert videos taken by the i-Speed 3 camera into data of the time and voltage response of the liquid. (A) Shows the original state of the image with visible liquid deformations under the needle induced by corona discharge. After thresholding the image, (B), is produced where the oil deformation and the electrode are shown as pitch black (intensity=0) on a white background (intensity=255). (C) shows the results of processing the thresholded image, wherein the size of the gap is obtained from the thresholded image. The gap size is the distance (originally returned as the number of pixels) between the bottom of the black deformed region formed by the surface deformation to the top of the black layer at the bottom produced by the ground electrode. These areas are identified by the averaging of the pixel intensity (0 for black and 255 for white) across each row of pixels in the image. A region of interest is chosen at the center of the image so as to avoid the dark regions associated with light inhomogeneity located near the walls. Noting that the un-deformed oil appears white, it should return an average value of 255 across a row that contains neither the deformed surface nor the bottom electrode. This is done for all frames of the video to produce a plot of the deformation with time. The 5.5 V line shown in (C) highlights a critical liquid deformation at which the liquid layer rapidly approaches the electrode. Also included in (C) is the rapid return of the liquid layer to its un-deformed gap size, which occurs after the voltage is removed at the end of test (170 seconds). (D) Shows the final processing step, which splits the data from (C) into intervals representing the voltage applied during each time step. Normally tests are performed incrementally increasing applied voltage every 10 seconds. The processing for (D) typically averages over the last 2 seconds of each interval to remove potential transients.

However, as the needle gets closer to the ground electrode a significant increase in current occurs. At this point, the I-V relationship no longer follows the Townsend Discharge regime, suggesting a change from corona discharge to a discharge more similar to the exponential glow-discharge [142]. With the addition of a liquid layer, this behavior changes. A transition occurs from no liquid (t=0) to liquid of t = 5.5 mm thickness such that at this thickness, the current produced by each needle height is approximately the same, which suggests that the electrical resistance of the dielectric medium is much larger than the corona drift region due to its dominant rule to determine the current. Therefore, the variations in electrode geometry are not effective at changing the current response in this range of dielectric liquid thickness. However, it is not clear at what oil thickness the transition occurs nor what fluid properties may affect it (beyond a qualitative understanding). For oil thicknesses approaching 5 mm the current produced at a given voltage is higher for needles closer to the ground electrode. However, above this point the nearest needle produces the least current for a given voltage. It is also difficult to evaluate the discharge in terms of Townsend Discharge or any other known regime as the current decreases below a threshold voltage before rising again. This might be attributed to space charge built up in the dielectric liquid. This charge accumulation stems from the inability of the liquid layer to transfer charges instantaneously. As explained by Chicon et al [134], space charge accumulation will occur when the ion transit time is shorter than the dielectric relaxation time:

$$\frac{\varepsilon}{\sigma} > \frac{t}{K_L E} \cong \frac{t^2}{K_L V_L} \qquad (2-2)$$

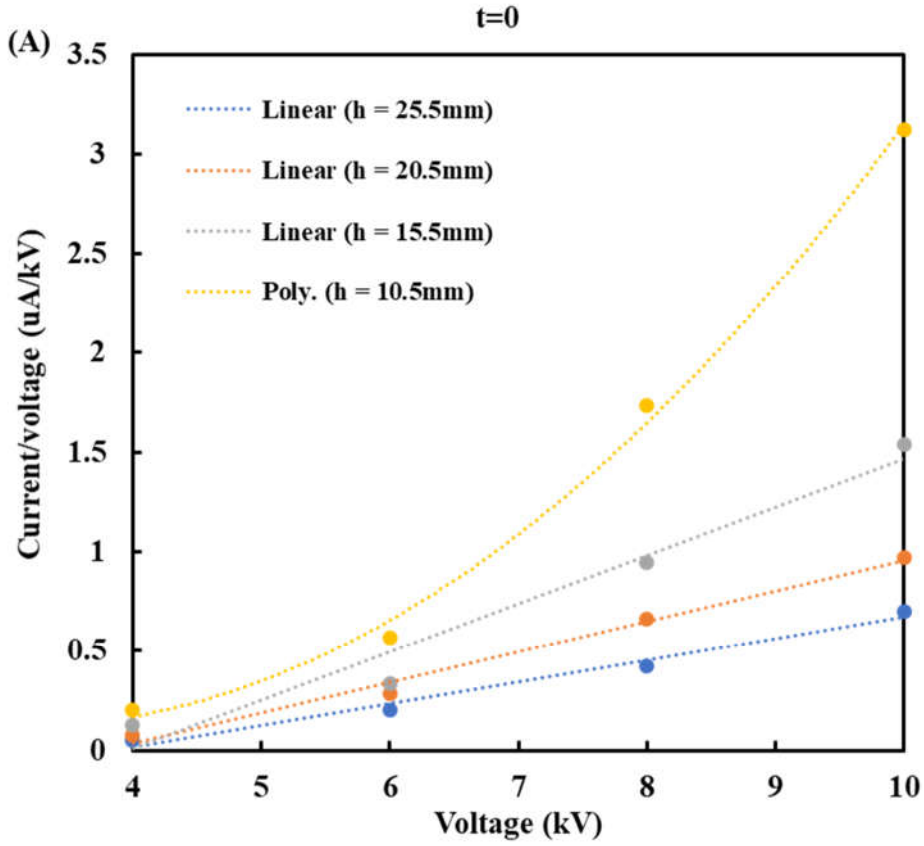
(A)
t=0
Linear (h = 25.5mm)
Linear (h = 20.5mm)
Linear (h = 15.5mm)
Poly. (h = 10.5mm)
Current/voltage (uA/kV)
Voltage (kV)
0
0.5
1
1.5
2
2.5
3
3.5
4
5
6
7
8
9
10

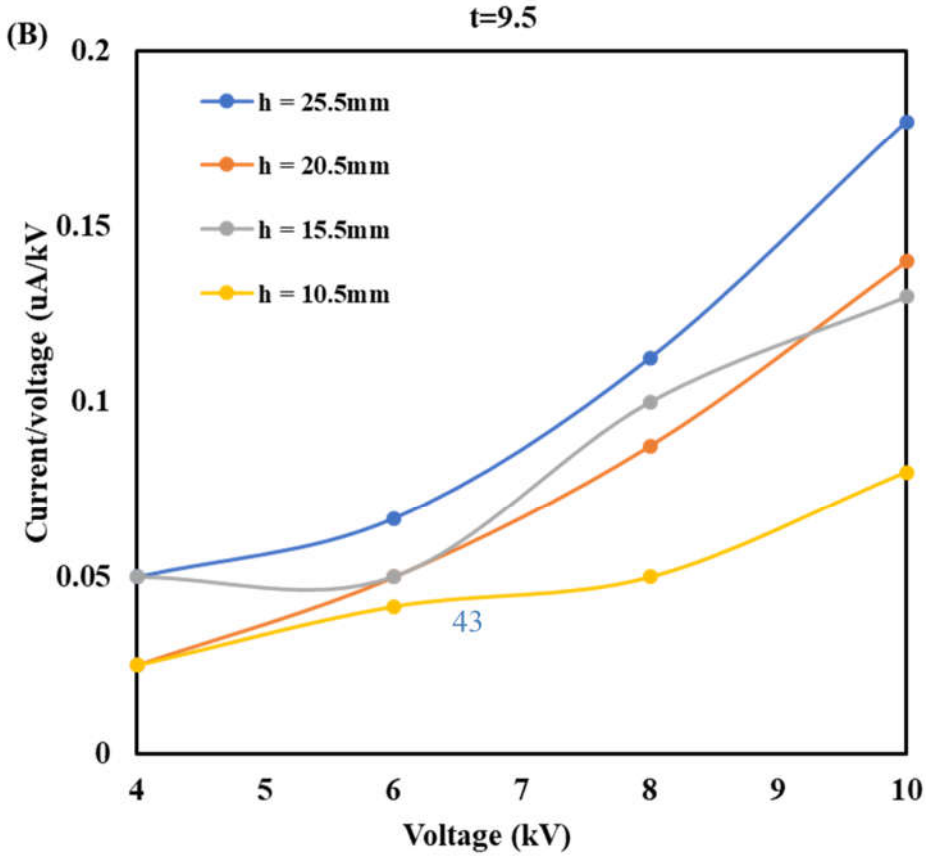
(B)
t=9.5
h = 25.5mm
h = 20.5mm
h = 15.5mm
h = 10.5mm
Current/voltage (uA/kV
Voltage (kV)
0
0.05
0.1
0.15
0.2
4
5
6
7
8
9
10

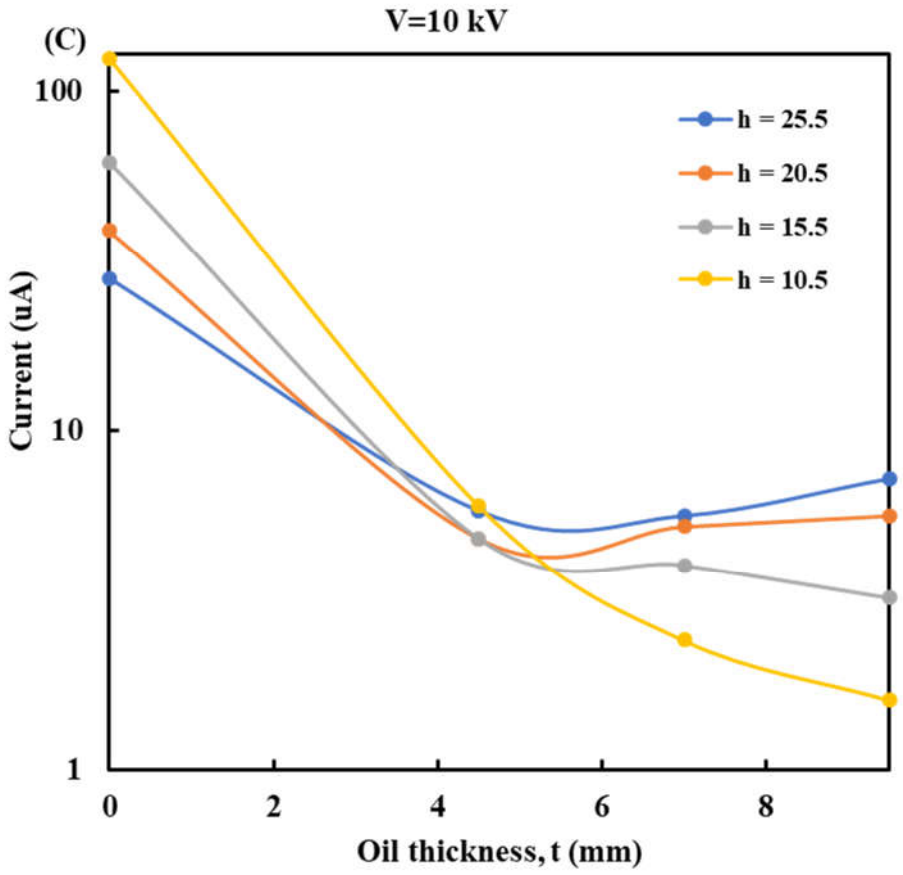

Figure 2-3 Corona discharge characterization. (A) and (B) show the measured current over applied voltage plotted vs. voltage for varied needle height (h). Dashed lines in (A) verified the linear relationship as expected for Townsend Discharge until the needle is only 10.5 mm away from the ground electrode, where the discharge enters the glow-discharge regime. (B) repeated (A) but with a silicone oil thickness of t = 9.5 mm located between the needle and the ground electrode. No linear trend is seen in (B) suggesting that the presence of the liquid layer alters the discharging behavior of the needle. (C) Shows the relationship between oil thickness (t) and the overall corona current measured for various needle heights. Between a liquid thickness of t = 5.5 and t = 7 mm there is a clear transition in behavior as the lowest needle begins to produce the least current.

where ε is the permittivity of the liquid, σ is the conductivity, t is the thickness, K_L is the ion mobility, and E is the electric field which under assumption of only small surface

deformations and uniform surface potential (V_L) can be approximated as V_L/t. The assumption of a negligible surface deformation should be valid below the critical voltage, V_c, for the onset of EHD instabilities as determined for space charge limited current flow with dynamic viscosity, μ, by [143]:

$$V_c \geq 99\frac{K_L \mu}{\varepsilon} \qquad (2-3)$$

It is therefore reasonable that the injecting electrode would inject more charges at greater distances from the charged surface as the generated ions have greater transit lengths before significant interference with the accumulated surface charge occurs. The oil thickness at which the nearest electrode begins to produce less current than those further away seems to mark the point at which the voltage at the needle is no longer sufficient to induce EHD motion sufficient to relieve the increased potential at the surface. Below this point it was noted that the nearest electrode can produce current near that of the dry case. These deformations (shown in **Figure** 2-4) resulted in the top surface of the liquid layer approaching the ground electrode just beneath the needle electrode. Due to the reduced oil layer thickness the voltage at which these deformations become of comparable size to the liquid layer is significantly smaller and as result much of the liquid's effects are negated. Above this voltage the system is thus able to produce similar discharge patterns to the dry case. This is also observed at greater thicknesses, despite the presence of an insulating liquid layer, as the deformations became large enough for spark discharges to occur through the air pockets created within the liquid layer.

Because of these qualitative tests, it was decided to leave the needle at a position of 15 mm from the grounding electrode due to its large response and limited interaction with the liquid layer beneath. The dielectric liquid thickness was then increased from 1 mm to 10 mm in 1 mm increments using both castor and silicone oils as the dielectric liquid. Silicone oils were used primarily for their high stability, but an added benefit was the wide range of available silicone oil viscosities. To qualify the effect of viscosity, silicone oils were purchased with kinematic viscosities ranging from 50 to 3000 mm^2/s. Castor oil was chosen for its relatively large surface tension (~38 mN/m at room temperature) when compared to silicone oils (~ 21 mN/m).

Figure 2-4 highlights the effect of increasing thickness of dielectric liquid on the deformations formed from corona discharge. These snapshots were each taken after a +10kV was applied for ~10 seconds to silicone oil with a kinematic viscosity of 350 mm^2/s. For $t \leq 2$ mm, the deformations formed could penetrate through the entire liquid thickness so that air pockets were now capable of reaching the surface of the grounding electrode. There is also a noticeable increase in the height of the oil layer, particularly at the edges since the bulk of the liquid in the middle is depressed as shown in the top view images in **Figure** 2-4 (left panel). These deformations are due to interactions between space charges in the air and liquid and the large electric fields produced by the needle. The electric field interactions in the air serve to increase the speed (and therefore pressure) of the ionic wind [144]. However, once the charge encounters the liquid surface it is unable to transit quickly due to the lower liquid conductivity and they thus become trapped. While they slowly

transit through the fluid the electric field continues to act on them resulting in an electrostatic pressure equivalent to [145]:

$$P_e = q_s E \cong \frac{\varepsilon_0}{2} E^2 \qquad (2-4)$$

where q_s is the surface charge density, E is the electric field on the surface, and P_e is the electrostatic pressure. Note that the approximation is valid for conductive surfaces as determined by Gauss's law.

As the liquid thickness is increased to 4 mm the structure of the deformations are observed to be largest in the center of the total deformation area with significant deformations occurring to either side of the central deformation. The authors suspect that this is due to the inhomogeneous nature of the electric field and the resulting current density of corona discharge. The distribution is reminiscent of Warburg's Law which defines the current distribution of corona as [146, 147]:

$$j = \frac{I_c}{2x^2}\cos(\theta)^n \begin{cases} n = 4.82 & \text{Positive Corona} \\ n = 4.65 & \text{Negative Corona} \end{cases} \qquad \theta \leq 65^0 \qquad (2-5)$$

where θ is the angle between the needle and a point on the surface and n is a constant. For the θ greater than 65^0 the value of current density is almost zero. I_c is total corona current and x is the gap separation. This results in a strong current density just beneath the needle electrode, which rapidly falls off to either side of the needle.

There is also generation of numerous air bubbles visible just to the right of the deformations. These bubbles often form after the charged surface deformation contacts the surface and quickly retracts as the charges within the oil are neutralized upon contact with

the ground electrode. Air often becomes trapped as these narrow channels collapse, resulting in the injection of small air bubbles on the order of 100 μm in diameter into the liquid. The surface patterning is also lost as the deformations become much less regular and more chaotic. At this point it is also clear that the deformations are conic in nature.

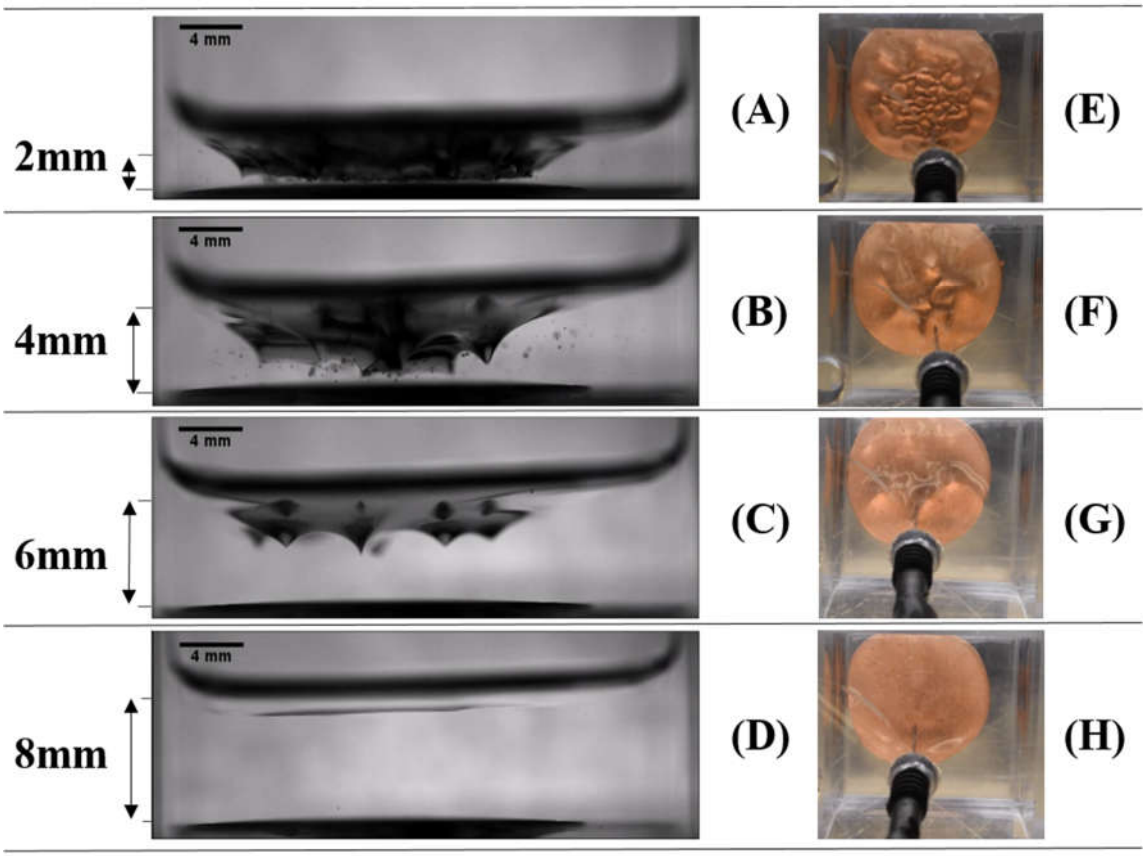

Figure 2-4 (A-D) Shows the side view images captured during exposure of silicone oil (ν = 100 cst) to corona when the needle potential was +10 kV. The measures to the side of the images represent the initial thickness of the liquid layer before tests. These images clearly show the conic nature of the deformations formed from corona exposure. The deformations in (D) are also significantly smaller than those found in (A), (B), and (C). The reduction in deformation size with respect to distance from the central peak of the deformation is visible in (B) while the patterned nature of the deformations is best shown by (C). (E-H) Show the corresponding top view images of the liquids during these tests. Note the reduction in cell size and count for increasing oil thickness. Surface deformation

size also decreases with increasing oil thickness. Above t = 6 mm, 10 kV of the applied voltage is no longer sufficient to induce notable deformations on/in this fluid.

When the liquid thickness is increased to 6 mm, the deformation appears in an orderly pattern with cells of equal size an equal distance apart, but the deformations are now significantly reduced in size and quantity. There is also no longer any noticeable change in the oil height. For a liquid thickness of 8 mm, any noticeable conic deformations are gone and only a slight deformation can be observed. This deformation is comparable in size to the deformation on the surface of water droplets when exposed to corona which is produced primarily by the ionic wind generated by the corona [136].

Figure 2-5 shows a summary of the results of tests performed on both silicone and castor oil processed as described in the methodology section. This plot shows the normalized gap, given as (t-d)/t from **Figure** 2-1, for various applied voltages. As the dielectric liquid thickness increases the voltage necessary to induce deformations through the surface increases. It often only takes relatively small changes in voltage, on the order of 100 V, to transition from a region of small deformations to deformations that penetrate through the entire oil layer thickness. This suggests that the deformation size is not tied directly to the applied voltage, but once a critical voltage dependent on the size of the oil layer is exceeded there is sufficient pressure to allow the creation of significant deformations.

The only exception to this behavior is the oil with a viscosity of 100 cst which is unable to deform to the size of the oil thickness for needle voltages as high as 10 kV. It appears that at these thicknesses, much of the charge is passed by the bulk motion of the fluid in

convective cells (see **Figure** 2-5). This bulk motion is likely quicker and easier to form for less viscous fluids since a lower shear force is required to accelerate the flow. In fact, once instabilities occur, the lower viscosity results in greater liquid flow velocity, effectively increasing the liquid's conductivity. However, it is only at the increased thickness that any differences between the various oil viscosities can be observed.

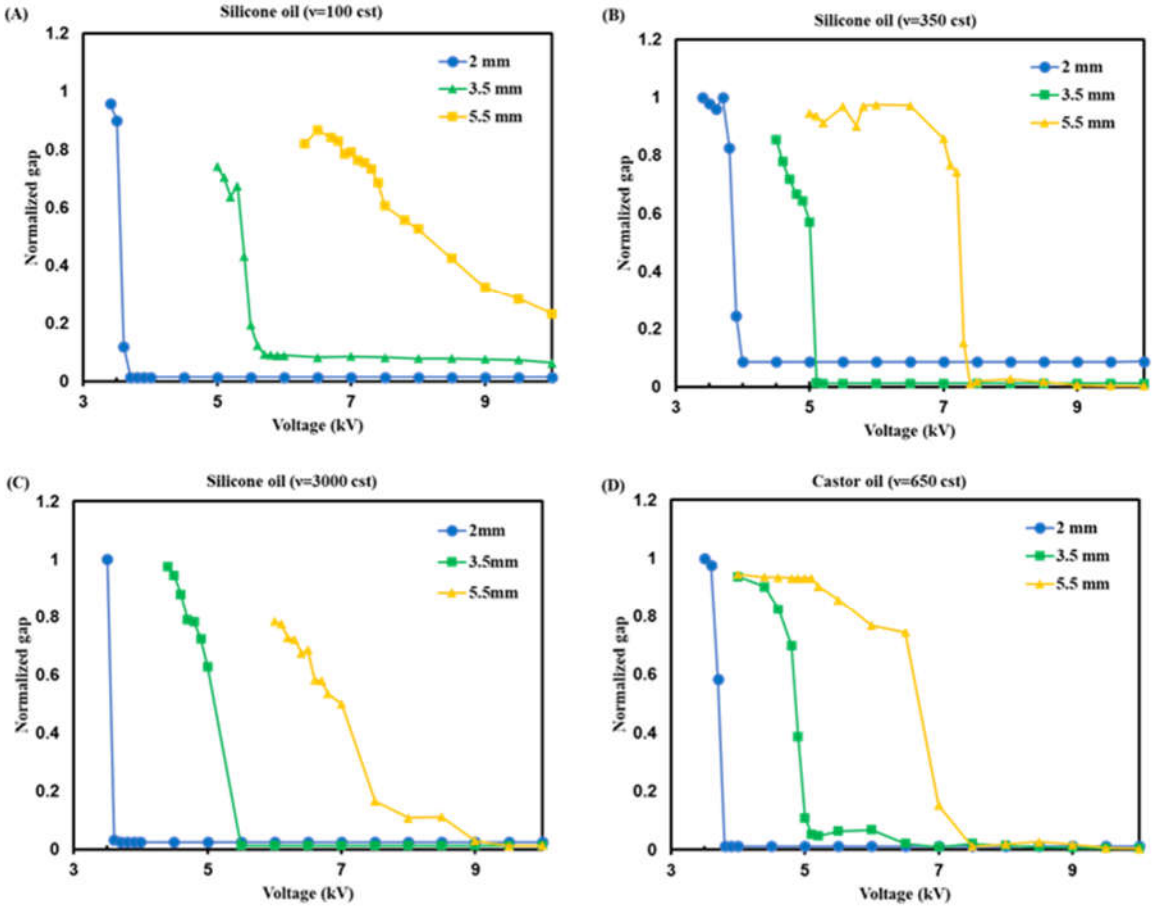

Figure 2-5 Surface deformation response to an applied needle voltage as evaluated using the method shown in **Figure** 2-2. A normalized gap, given as (t-d)/t from **Figure** 2-1, value of 0 implies the deformation has penetrated through to the ground electrode (g=t-d). Three different oil thickness are represented for four different types of fluids (A) silicone

oil (ν=100 cst), (B) silicone oil (ν=350 cst) (C) silicone oil (ν=3000 cst) (D) castor oil (ν=650 cst). In all cases, t = 5.5 mm requires the greatest voltage to fully deform while the t = 2 mm test cases require the least. Of the data presented, only silicone oil at with ν=100 cst (the least viscous oil tested) at 5.5 mm fails to reach the ground electrode. This suggests that the size of deformation reduces with liquid viscosity.

Figure 2-6 shows the tracks of multiple air bubbles formed during the testing of castor oil with a thickness (t = 9 mm) and the needle height of (h = 15 mm) and +10 kV. The fortuitous formation of these air bubbles is likely tied to the surface tension of the liquid as a noticeable increase in air bubbles observed in castor oil when compared to silicone oil which has a surface tension nearly half that of castor oil. However, this may be an indirect cause, as it seems the increase in surface tension also results in larger capillary formations as shown in **Figure** 2-6. These capillary formations also result in increased air bubble formation. The tracks showing the motion of the bubbles, and by extension, the fluid, were generated using the open-source Fiji plugin TrackMate. The tracks highlight the general fluid motion that occurs after surface instabilities are generated and clearly show their convective nature. While we acknowledge that the bubbles are not moving exactly as the fluid does, their motion is entirely directed by the motion of their neighboring fluid and thus reflects their behavior closely. This finding is in agreement with previous work that has traced the motion of corona-induced electroconvection cells [148]. The formation of convective cells has been attributed as a method of increasing the flow of charges through the liquid once the liquid's inherent conductivity is no longer sufficient to transport charges quickly enough to prevent space charge formation [149]. Also, as predicted by Atten and others [132], the final cell size is on the order of the liquid's thickness.

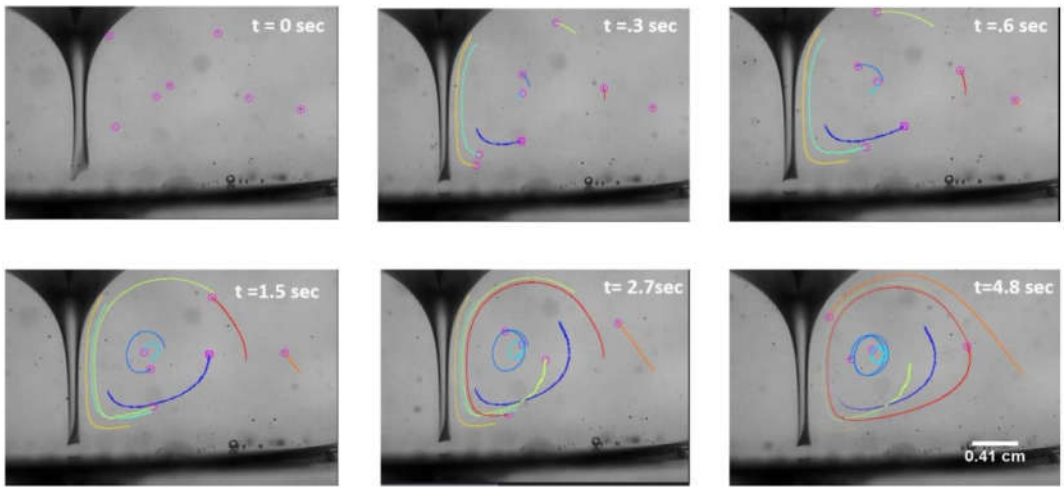

Figure 2-6 Counterclockwise convective instability tracks recorded over a period of 5 seconds in a 9 mm thick layer of castor oil. A unique color represents each track. Although not shown, the convective motion is symmetric and present on both sides of the large conic deformation seen in the images. Tracks are produced by tracing air bubbles that formed when 10 kV voltage was applied to the overhead needle. Tracks were created and visualized using the ImageJ TrackMate tool [150].

High-speed analyses were also performed during the transient formation period of the deformation, as shown in **Figure** 2-7. The images show that the cone evolution starts off slowly, with no significant deformation seen until nearly 350 ms after voltage was applied. However, once a large deformation is formed, it rapidly evolves into a conic or capillary-type structure extending almost completely through the liquid medium. This intensification period results in a fully developed cone formation within only 125 ms, resulting in a rapid acceleration of the liquid during this period.

The final formation is slightly smaller than the maximum size achieved during the formation process primarily due to retraction slightly after contact with the grounding electrode. There is also the significant spreading of the leading edge of the cone during this

phase as can be clearly seen after 650 ms of corona exposure. This spreading results in the formation of numerous air bubbles at the tip of the cone. This seems to mark an alternative

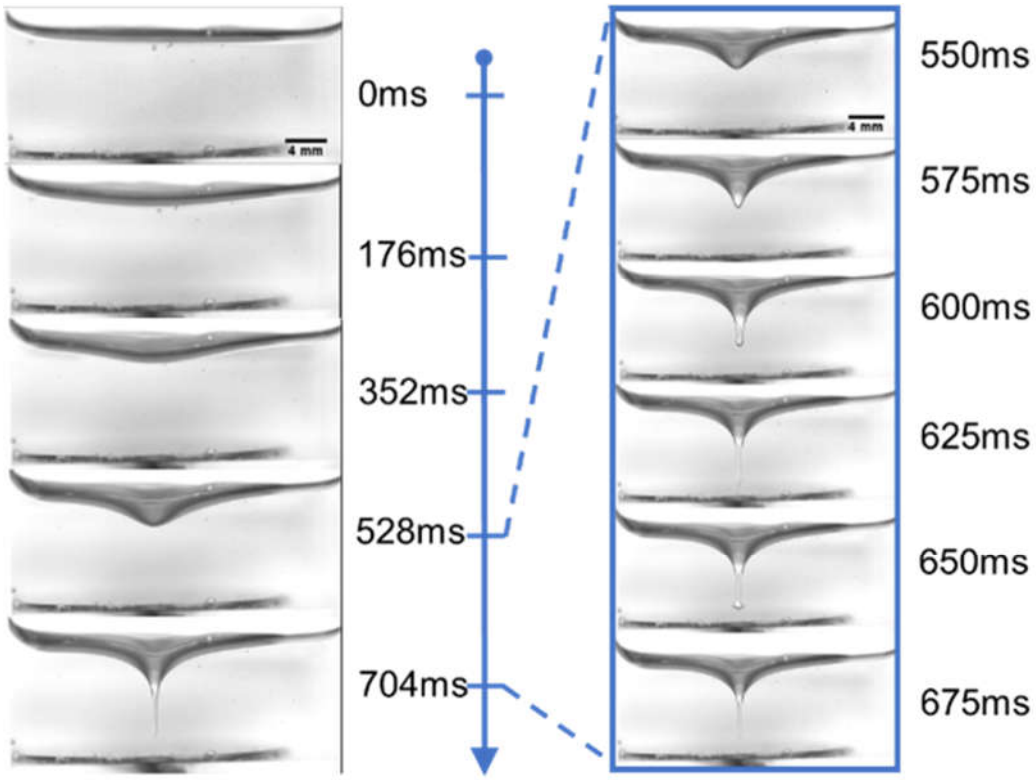

Figure 2-7 Response of a 9mm layer of castor oil to the application of a +10 kV step to the overhead needle. The video was recorded at 1000 fps with an i-Speed 3. The left-hand side shows the formation process in 176 ms intervals (the total time to steady-state formation was 704 ms). The right-hand side shows the evolution between 528 ms and 704 ms in 25 ms intervals. It can be seen from the left-hand side images that the cone formation process accelerates rapidly after the first initial deformation occurs at 528 ms. Additionally, the final cone size formed after corona exposure for 704 ms is slightly smaller than the maximum size of the cone formed after 650 ms of corona exposure. The tip of the cone can also be seen spreading after 625 ms of corona exposure, which results in the formation of two sizeable air bubbles by 650 ms.

method of air bubble formation than the observed conic collapse during chaotic periods of cone formation and destruction of the deformed surface. The spreading indicates a

significant drag force acting on the deformation during the formation process likely because of the velocity of the leading edge of the formation. Since the applied voltage heavily dictates this speed, it is reasonable to presume that there will be increased bubble formation for increased applied voltages so long as the voltage exceeds the critical value necessary to induce deformations on the order of the liquid layer thickness.

It is to be noted that this cone formation will persist for the entire period of voltage application without major change to its shape or size. Bubbles occasionally do interact with the cone causing its rapid disintegration and reformation, leading to additional bubble generation. There is also no marked increase in the current measured after the deformation forms. This seems to suggest that the conic structure merely marks an equilibrium between the injected charge and the released charge. Otherwise, more current would likely fall through this region since it is now a purely air path between the needle and the ground plate. But, as the test at lesser liquid thicknesses suggests, a large enough voltage may result in sparks forming through this conic region most likely accompanied by additional deformations across the surface. **Figure** 2-8 illustrates the differences in behavior of different oils when all other conditions are the same (oil thickness, applied voltage, needle height). Castor oil can form the largest deformation while both the silicone oil with large and small values of viscosity show little change at their surfaces. This suggests that viscosity is not one of the leading causes of the large formation produced by castor oil despite it being responsible for the decreased deformation sizes of silicone oil as seen in

Figure 2-5. It is believed that this is likely due to the large differences in surface tension. One key parameter for comparison is that of the capillary length of the two types of liquids:

$$l_c = \sqrt{\gamma/\rho g} \qquad (2-6)$$

where γ is the surface tension and ρ is the density of the liquid. Capillary length also known as capillary constant, is a length scaling factor relatings gravity and surface tension. A liquid pressure, in its static mode, is derived from its specific weight and its height in a container. In addition, surface tension forces (Laplace force) are result of cohesion between molecules of the liquid, causing pressure on the liquids. Since the attraction to the surface molecules of a liquid is less than that of the molecules inside the bulk liquid, the surface of liquids become curved (concave or convex). Based on the curvature of the meniscus (surface of the liquid) it is possible to claclulate its capillary length [151-153]. Castor oil has a capillary length of approximately 2.04 mm at room temperature while silicone oil has a capillary length of only 1.49 mm. However, the difference does not seem large enough to solely account for the radically different deformations observed. In order to investigate the effect of surface tension, glycerol oil with a viscosity close to that of the castor oil and a surface tension higher than that of castor oil was treated under the identical corona discharge. Dissimilar to the deformation observed in castor oil, the glycerol oil did not deform severely despite the higher capillary length (2.27 mm). In general, the liquid deformation is not only influenced by the surface tension but also depends on the electrical properties of the liquid. Based on equation (2-4), comparing silicone oils to the glycerol oil, an increase in the electrical conductivity is

increasing current passage through the oil. On the other hand, the amount of trapped charges on the oil surface decreases by an increasing electrical conductivity. Overall, the electrostatic pressure is a function of the applied electric field and the number of trapped charges on the surface. This combined effect eventually leads to a maximum deformation observed in the castor oil. To summarize, in silicone oil the electric field is negligible while in the glycerol medium the number of trapped charges is low. As a result, these two cases (silicone oil and glycerol oil) do not undergo a high electrostatic pressure to deform significantly.

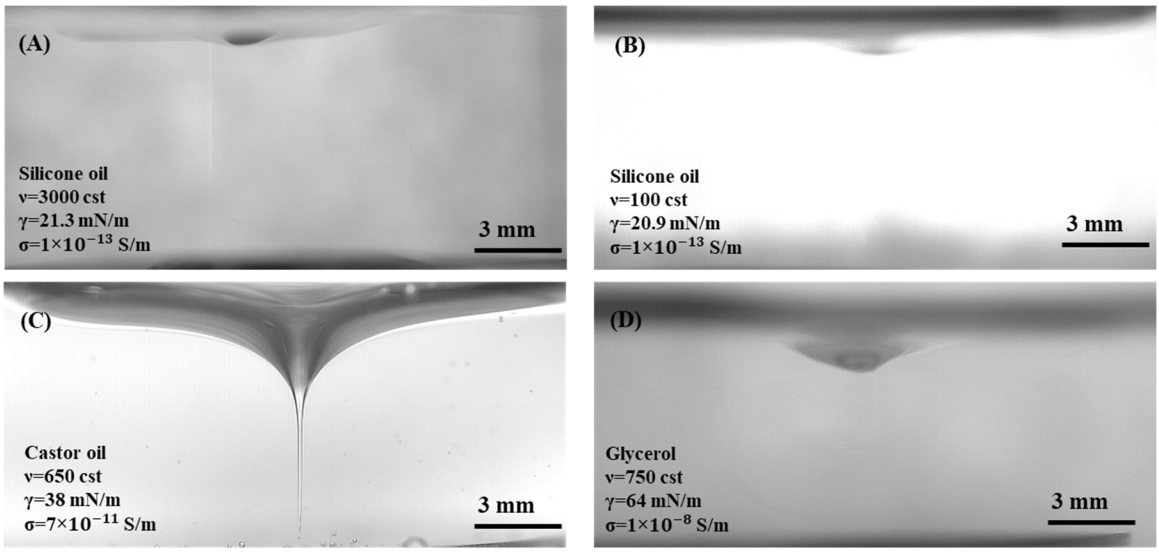

Figure 2-8 Various liquids (t = 9 mm thick) exposed to corona generated by applying +10 kV voltage to the needle. (A) Shows silicone oil (ν=3000 cst), (B) silicone oil (ν=100 cst), (C) castor oil (ν=650 cst), (D) glycerol (ν=750 cst). Deformations in the silicone and glycerol oils are minimal, potentially predominantly from the ionic wind. Note in this case, the glycerol's deformation is slightly larger than that of the silicone oil shown in (A) and (B), regardless of their viscosity. This might be attributed to the large current and thus ionic wind that the glycerol experienced since it does not produce a large concentration of injected charges. The castor oil shown in (C) experiences a much greater surface

deformation than any other fluid despite having a two order of magnitude higher conductivity than the silicone oil.

2.6 Discussion

Figure 2-9 shows how the bulk oil layer responds to a change in applied power on an oil layer of a given initial thickness. This change in oil height occurs in areas where there is no deformation because of the corona discharge and can be treated as uniform throughout those areas. For our test container, the ground electrode is 5 cm^2 and the overall container area is 9 cm^2 so we can estimate this height change to occur within area of approximately 4 cm^2. Of course, this assumption is not entirely valid as regions near the electrode still experience some ionic wind and thus some downward forcing pressure while areas near the edge tend to experience forcing pressures in the direction of the walls. This usually manifests itself in the oil beginning to climb the walls of the container; in general, the more intense the power the higher the oil can climb because of the increase of ionic wind at the wall. However, this Figure does not include those changes in their determination, only the change in height of the bulk fluid.

Two key trends can be observed in **Figure** 2-9. First, as the initial oil layer thickness decreases, the overall change in height increases for a given applied power. Thus, a pumping setup using this method is likely to be most effective with thin liquid layers. This corresponds to the greater deformation obtained at a given voltage for thinner liquid layers as seen in **Figure** 2-4. However, above a certain change in height, there is no further

significant changes in the oil height for continuing increases in power. We believe this is a result of the large deformations that have, by this point, formed in the liquid layer. These deformations result in near direct air contact from the needle electrode to the ground electrode. As a result, we believe that for changes in applied voltage an ionic wind current preferentially flows through these paths rather than into the bulk liquid layer. Thus, there will be no further increase in forcing pressure on the liquid outside of the deformed areas. An increase in convective speed is expected, but there does not appear to be widening of the deformed regions nor a noticeable increase in their density above these voltages. This results in the trend seen in **Figure** 2-9 wherein there is no further increase in liquid layer thickness from the corona discharge. However, as previously expressed, regions near the walls do seem to experience greater ionic winds resulting in an increased oil height on the sidewalls of the container.

Overall, these results seem to suggest that there is an optimal operating point for this configuration that maximizes the dielectric liquid pumping properties of potential devices. It should also be noted that the trend favors thin layer spreading as could be obtained using sloped electrode geometries similar to what has been previously observed [130, 138, 140, 141]. However, to obtain the best efficiencies careful consideration of the corona producing electrode's geometry must be considered.

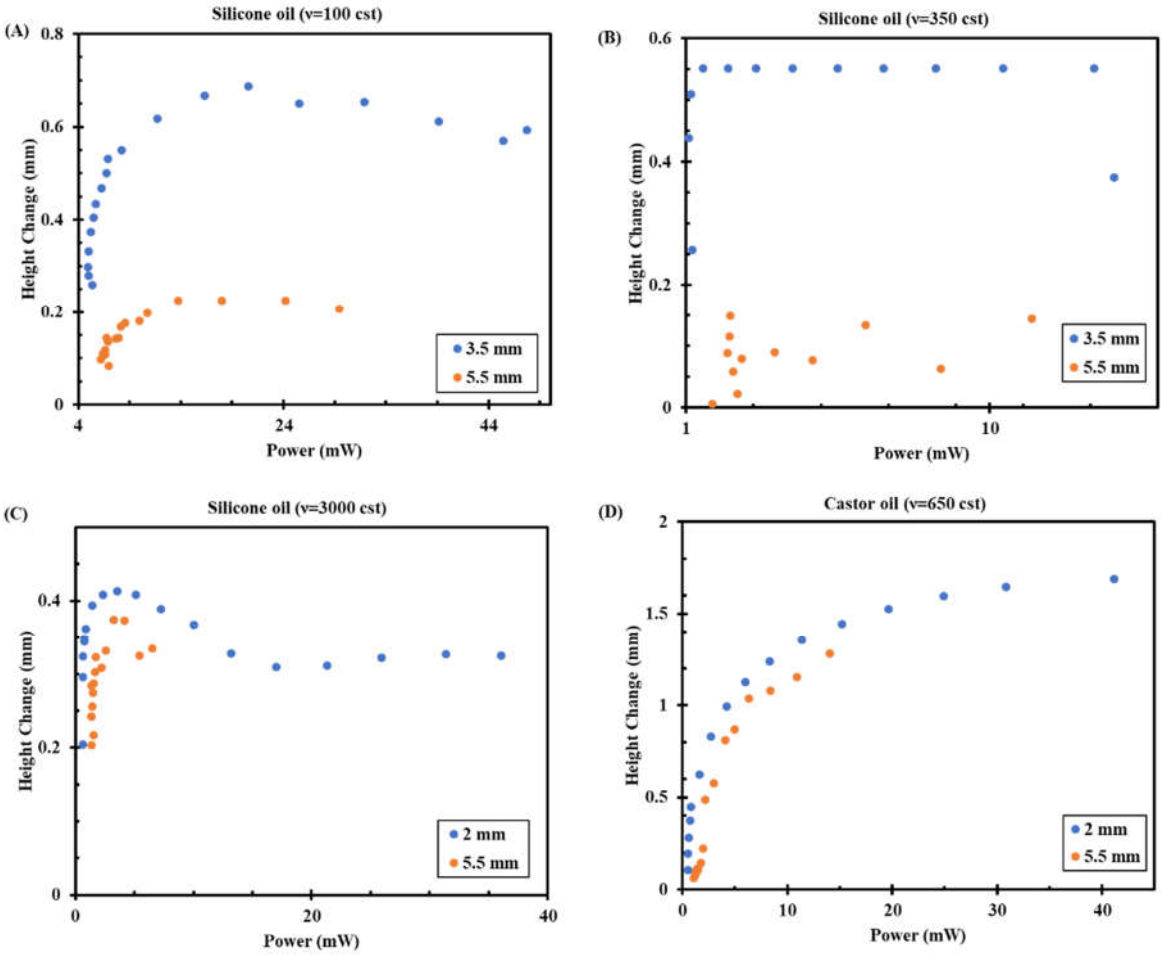

Figure 2-9 Change in liquid layer thickness plotted against the applied power for (A) silicone oil (v=100 cst) (B) silicone oil (v=350 cst) (C) silicone oil (v=3000 cst) (D) castor oil. Tests were performed with DC voltages from 3-10 kV and initial oil layer thicknesses of 2, 3.5, and 5 mm. Thicknesses were measured at the top layer of the oil as observed from the side-angle camera (see **Figure** 2-4 for visible changes in thickness). This represents a bulk change in thickness rather than the extension of oil up the walls of the container due to the ionic wind. Results indicate a greater thickness change is observable in thinner liquid layers under the same applied power, translating to improved pump performance. Additionally, the thickness change is significantly larger for less viscous fluids as can be seen by a comparison between (C) and (A) potentially caused by the larger flow velocity for equivalent electric pressures. There also appears to be a critical applied power, dependent upon the oil layer thickness and the oil type, above which no further thickness increase is experienced this is clearly visible in (B) and is likely due to increased

current flow through the already deformed region without significant interaction with the liquid layer.

Table 2-1 Oil properties

Dielectric Liquid	Conductivity σ (S/m)	Relative Permittivity ε	Surface Tension γ (mN/m)	Density ρ (g/mL)
Silicone Oil (100 cSt)	1×10^{-13}	2.73	20.9	0.964
Silicone Oil (350 cSt)	1×10^{-13}	2.75	21.2	0.969
Silicone Oil (3000 cSt)	1×10^{-13}	2.75	21.3	0.97
Castor Oil (650 cSt)	7×10^{-11}	4.69	38	0.961
Glycerol (750 cSt)	1×10^{-8}	40	64	1.261

2.7 Conclusion

In this chapter, we present a new way to analyze EHD instabilities produced by unipolar injection. We show that we are able to analyze the depth and height of dielectric liquid surfaces exposed to corona discharge utilizing image processing. Our results indicate that the theories previously used to predict the onset of instabilities in non-conductive thin liquid layers exposed to charge injection are applicable to bulk liquids spanning up to 1 cm in height. However, it is no longer possible to adhere to assumptions of limited surface deformation as deformations can extend well into the liquid medium. This negates many of the common assumptions made for analysis of these systems such as uniform surface potential or uniform charge injection.

Our work also provides an understanding of the pumping properties of corona discharge manifested at elevated oil edge thicknesses. This increase in thickness can be considered as analogous to a hydraulic lifting mechanism, treating liquid edge as the liquid

surface and the deformation as the volume displaced by a pressure normal to the surface. Modifications can be made to the experimental apparatus to exploit this forcing component to potentially extract dielectric fluids or to actuating a surface riding on this outer edge of liquids. Results also indicate that devices based on this forcing mechanism may experience a maximum effective power such that exceeding this power level will only result in an increased current and not an increased surface deformation.

Finally, we show that viscosity and surface tension are two of the most important parameters of dielectric liquids. While the liquid must still be sufficiently non-conductive to guarantee charge build-up if a liquid is sufficiently non-conductive differences in conductivity do not seem accountable for the variations in liquid behaviors. Rather, the viscosity becomes a determining factor for the response of the liquids to electric pressures. With lower viscosity, the pressure is not as concentrated on the surface, resulting in rapidly decreasing deformation depths. However, an increase in surface tension can result in greater deformation depth for greater oil layer thicknesses even if the overall deformed volume decreases. It also seems instrumental to the injection of air into the liquid medium during the chaotic formation and destruction of the surface deformation cones.

Chapter 3

3 Electro-coalescence of water-in-oil emulsion under non-uniform electric field induced by corona discharge

3.1 Abstract

This chapter discusses an experimental approach to study the effects of a contactless method on electrocoalescence of water in oil mixture/emulsion. A positive corona discharge is utilized using a sharp conductive needle without direct contact with the mixture/solution to avoid potential corrosion of the electrode. This creates a non-uniform electric field which is further used for the coalescence of water droplets in the range of micro to macro in oil. Two approaches are employed in this study; qualitative analysis conducted by visually studying coalescence patterns in videos captured with a high-speed camera, and a quantitative analysis based on calculations obtained from dynamic light scattering measurements. From the behavior of the water droplets under the electric field,

it is observed that dipole-dipole interaction, migratory coalescence/electrophoresis, and dielectrophoresis have major roles in promoting the coalescence events. The effects of oil viscosity and power consumption on the coalescence rate are also investigated, suggesting an optimal oil-water separation process. The results of this study pave a path for developing a safe, contactless, rapid, and low-power-consuming separation process, potentially suitable for an offsite application.

3.2 Introduction

3.2.1 Separation of water from oil

The separation of water from an emulsion is the most common processing step in applications such as petroleum de-emulsification, chemical dehydration, desalination, wastewater treatment processes, and other industries such as resource recycling, metallurgy, and equipment manufacturing [93, 125]. Water and oil mixtures can be separated by exerting external forces, self-induction, gravity forces, and buoyancy forces enabling their separation and removal [114, 154]. In gravity separator setups, the sedimentation time of the small water droplets (sizes less than 100 μm) is in close correlation with the residence velocity [155]. The sedimentation time for water droplets significantly changes with their size, and it can vary from seconds to years for sizes ranging from macro to micro scale [156]. The motion of water droplets towards each other triggered via mechanical forces [157], microwave radiation [158], thermal forces [159], electrostatic

forces [160], membrane separation [161, 162], demulsifier [163], adsorption [164], absorption [165], and chemical reactions [166, 167] governs the separation rate in the emulsion. However, electrocoalescence is the most common method of coalescence used in various industries, providing a fast and efficient separation of emulsions [93].

3.2.2 Electrocoalescence

The separation of a water droplet induced by external electric fields results in the generation of a dipole that further interacts with another adjacent dipolar water droplet, enhancing the coalescence rate in an emulsion. This process is called dipole-dipole interaction (DDI), which is considered the primary mechanism for observing electrocoalescence in a uniform electric field. The motion of water droplets can also be induced via Coulombic forces caused by an external electric field on charged water droplets, enhancing the chances of collision between the water droplets and leading to so-called migratory coalescence. The migratory coalescence is mainly due to the electrophoresis (EP) force and is observed when utilizing DC electric fields; a few studies available in the literature investigated this effect on the electrocoalescence process. Overall, the kinetics of electrocoalescence events are governed by various parameters such as electrical and physical properties of the fluids, the magnitude of the external electric fields, emulsion impurities, flow and turbulence of the fluids, water droplet sizes, and dispersion of water droplets, which have been extensively investigated in the literature [168-171]. However, chain formation, water droplet splitting, low performance on the low

water content, residue water droplets, and high-power consumption, particularly for AC electric field, are some of the incidents that have adverse effects on the electrocoalescence rates and performances. These incidents could potentially occur due to the application of moderate electric fields during separation processes [114]. For instance, alignment of the water droplets in the direction of the applied electric field, forming a water bridge in a shape of a chain that causes an electric discharge (i.e. short circuit) and consequently a reduced coalescence rate [172, 173]. These adverse characteristics can be alleviated either by coating the electrode tip with thin layers of dielectric materials with a compromise of extra cost and additional required electric field/power consumption. Alternatively, using a microfluidics setup could eliminate the chances of chain formation by continuous motion of the fluid inside the channels. However, the scalability of the microfluidics channels/devices is limited and they are not suitable for offsite industrial applications [174]. Also, electrode corrosion is another challenge due to the electrolytic effect at anode electrodes (especially when utilizing DC electric fields) [175].

In general, changing the strength of the electric field leads to two orders of magnitude enhancement in the coalescence rate of water droplets [176]. Some studies have shown that there is an electric field threshold in emulsions below which electrocoalescence cannot be fully triggered, requiring the intensity of the electric field to be increased to activate DDI and EP [103]. Furthermore, improving the performance of these two mechanisms are corresponded to increasing the strength of the electric field. However, by increasing the field strength, it is most likely to form water droplet chains across the electrodes and split

water droplets undesired in the coalescence process. Williams suggested three electrostatic splitting mechanisms. Water droplets will be elongated along the direction of the electric field and will be disintegrated if the electric field is strong enough. Another mechanism related to constraining the acquired charges by coming to contact with the electrode or charged water droplets is given by Rayleigh. The third disintegration mechanism is triggered when the water droplets are attached to one of the electrodes. In this case, charges accumulate at the tip of droplets and start forming the Taylor cone, which produces small droplets at the tip of the water droplet [88, 177]. This issue could be mitigated by applying a hydrophobic coating to the electrode to prevent droplet formation on the electrode; however, it requires extra cost. In spite of increasing the strength of the electric field, in some cases, the water droplets retreat after initial contact with each other forming non-coalescence water droplets; thus, this increase in an electric field can decrease the efficiency of the coalescence and ultimately the separation process [178, 179]. To avoid activating those mechanisms and increasing the interaction force (coalescence rate), it is needed to determine a general strategy to solve this problem. Recent studies have shown promising results by utilizing non-uniform electric fields for emulsion separation with improvement in the dehydration process and accelerating the movement of water droplets [180, 181]. However, an optimum electrode geometry for creating a non-uniform electric field remains challenging, mostly due to the Joule heating effect [176, 182, 183]. To address this challenge, it is required to have a flexible and contactless method when applying electric discharge and forming non-uniform electric fields.

3.2.3 Corona discharge

Corona discharge provides many advantages in several industrial applications such as photocopying, ozone generating, and air filtration [184]. When a neutral gas (i.e. air) is introduced to a high potential gradient, it results in gas ionization and loss of neutrality. The most common configuration to create corona discharge is a point-to-plane setup. The gas in the space near the sharp conductive electrode ionizes when applied a threshold voltage, sustaining a continuous discharge regime. In a positive corona discharge, positive ions of gaseous medium form free space charge carriers accelerating towards the negative ground electrode [185, 186].

Here, a contactless method of emulsion separation is presented utilizing a non-uniform electric field, induced via a corona discharge. The corona discharge generates ions for inducing an electrohydrodynamic (EHD) instability inside a W/O mixture/emulsion. The charged ions accelerate and drift towards the opposite electrode, creating an ionic wind. Locating the W/O mixture/emulsion between the corona-producing electrode and the ground electrode results in the injection of the ions and the formation of a non-uniform electric field in the mixture/emulsion. Due to the contactless nature of our method, there is no electrode corrosion as a result of exposure to the W/O mixture/emulsion. The air gap between the corona-producing electrode (a sharp conductive needle connected to a high voltage) and the W/O mixture/emulsion acts as a current barrier and results in improving the safety of this separation process. Besides, the non-uniform electric field generated in this configuration eliminates the complexity involved in conventional methods such as the

design of the electrode geometry and/or temperature rise due to the Joule heating effect [183]. Finally, the formation of the ionic wind and its injection into the W/O mixture/emulsion induces electroconvection in it, breaking up chain formation by water droplets which is problematic in conventional electrocoalescence.

3.3 Results and discussion

The corona discharge current/voltage characteristics follow the Townsend discharge regime defined by [142]:

$$\frac{I}{V}=k(V-V_0) \qquad (3-1)$$

where I is the current, V is the applied voltage, k is a constant, and V_0 is the corona onset voltage. Indeed, the space charge between the sharp electrode and the liquid surface acts as a large nonlinear resistor or, in other words, acts as current overload protection, playing a safeguard role against short circuit events. The power loss due to this resistance behavior is trivial (in the order of mW) due to the microamp range of the current. The optimum distance of the electrode (corona gap) on dielectric liquid was reported in our previous work [186]. Air molecules/atoms were ionized in the area close to the sharp electrode with a high potential gradient. The liberated electrons move toward the sharp electrode and the positive ions are subjected to an electric field, accelerating from the pointed electrode to the ground electrode. The dielectric liquid can be considered ohmic fluid if the traveling

time of the injected ions is less than the relaxation time of the liquid. Otherwise, it is fair to be assumed as a nonohmic fluid [187].

$$\frac{\varepsilon_c \varepsilon_0}{\sigma} > \frac{L^2}{K_L V_L} \qquad (3-2)$$

where ε_c is the dielectric constant of the liquid, ε_0 is the permittivity of free space, σ is the conductivity, L is the thickness, K_L is the ion mobility, and V_L is the surface potential. In this experiment, the relaxation time of silicone oil is calculated to be 400 seconds (with $\varepsilon = \varepsilon_0 \varepsilon_c$, $\varepsilon_0 = 8.85 \times 10^{-12}$ F/m, $\varepsilon_c = 2.75$, and $\sigma = 6 \times 10^{-12}$ S). On the other hand, the mobility of the ions of the air is much higher than that of liquid mobility and results in charges being trapped on the liquid surface. This situation is called Space Charge Limited Current (SCLC); therefore, we can conclude that the silicone oil in our experiments acted as a nonohmic fluid. The electric field in the corona gap can be found by [188]:

$$E(x) = \frac{V}{(x + r) \times \ln\left(\frac{2t + r}{r}\right)} \qquad (3-3)$$

where r is the sharp electrode radius of curvature, t is the corona gap, and x is the abscissa of the point to a sharp electrode. The current density in the air is $j = K_a E q$ ($dE/dz = q/\varepsilon_0$) and in the liquid is $j = K_L E q$. From the continuity of εE on the oil surface and by the integration of $V = E.dL$, we can reach the voltage distribution on the oil surface. The surface potential can be found by [135]:

$$V = \left(\frac{8J}{9 K_L \varepsilon L^2}\right) \qquad (3-4)$$

Utilizing the corona discharge, the ionic wind collides with the W/O mixture/emulsion surface and the current density varies from point to point which can be found in Warburg's equation (equation (2-5) [189].

It can be seen from the above correlation that the oil surface acts as an electrode in which the surface voltage is distributed as a function of distance to the sharp electrode. This non-uniform distribution of the surface potential and the constant potential of the ground electrode build a non-uniform electric field in the oil medium ($E=V/L$) [190].

3.3.1 Coalescence of two water droplets in oil medium

In order to examine the impact of corona discharge and various electrocoalescence phenomena involved in the process, simple tests were conducted by placing water droplets inside a silicone oil medium, and their trajectories were examined via high-speed imaging. To this end, a table setup was designed to expose water droplets dispersed inside a dielectric oil to corona discharge. **Figure** 3-1 shows the schematic of the setup, including mainly three parts: a high-voltage amplifier connected to a sharp electrode for corona generation, an adjustable mechanism used to keep a grounding electrode in contact with the emulsion, and a measuring unit incorporating current measurements**Figure**. First, the test cell was prepared by filling a quartz cube up to 15 mm high with silicone oil of 3000 cSt viscosity, and the corona gap was kept at 10 mm (t=10 mm). The high viscosity oil was used to increase the sedimentation time of the water droplets to provide enough time to observe

the droplets' behaviors during the experiment. The sedimentation velocity is defined by equation (1-3) [156]:

where a is the droplet radius, ρ_W is the droplet (water) density, ρ_C is the continuous phase (oil) density, η is the fluid dynamic viscosity, and g is the gravitational constant.

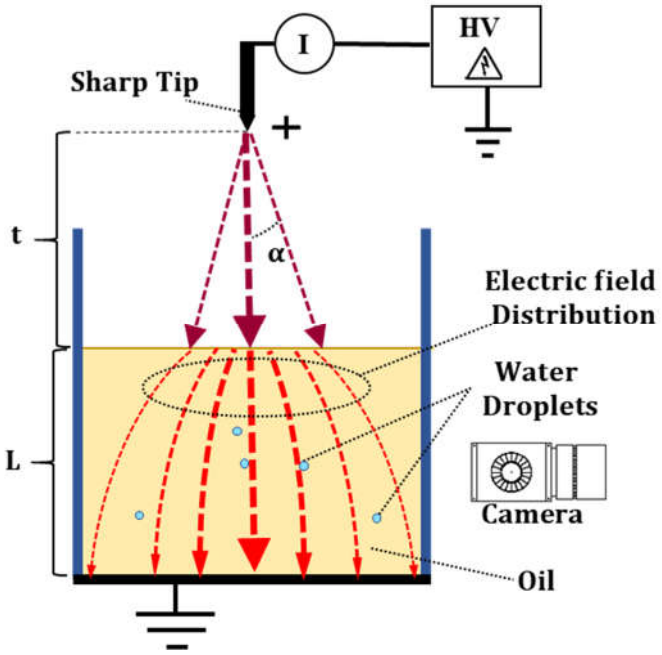

Figure 3-1 Schematic of the experimental setup. The height of the needle was adjusted by a laboratory jack to which the test cell was fixed. High voltage potential (V) creates a strong potential gradient between the electrodes resulting in ionization of the air molecules. The charged ions accelerate and drift towards the opposite electrode, creating an ionic wind. When the ionic wind collides with the emulsion surface, the charges are transformed via conduction or convection, making a non-uniform electric field in the dielectric medium. The current density distributes non-uniformly on the W/O mixture/emulsion surface following Warburg's law, presented in equation (2-5). The electric field is stronger in the center and surface of the W/O mixture/emulsion as a direct result of the current density distribution. Current and voltage were measured actively during the experiments, and videos were captured from the side view of the test cell.

Four major positions of the water droplets were considered in this experiment to investigate the effect of the DDI, EP, and DEP. The corona voltage was kept constant at 4 kV. This voltage was selected to eliminate the impact of flow motion induced by electroconvection [148].

The first two water droplets were dispersed closely in the center of the test cell (**Figure** 3-2A). In this situation, it was expected that two water droplets form dipoles due to the polarization in the electric field and interact with each other. The distance between the two dipoles was close enough to build large interaction energy and to develop radial and tangential forces as shown schematically in **Figure** 1-6 and can be described by equation (1-11 and 1-12)[191].

It can be inferred from equations (1-11) and (1-12) that the interaction between two water droplets is significantly affected by their distance (proportional to the inverse of the 4th power of their distance). In addition, an increase in the size of water droplets can enhance coalescer performance by three-folds. At the beginning of the test, the effect of the radial force was not considerable because of the angle between the dipoles and the distance vector, as can be seen in equation (1-11); hence, the droplets did not move towards each other. However, the net tangential force was not zero appearing right after polarization based on equation (1-12). Subsequently, the two dipoles rotated counterclockwise to approach the position where the radial force was high enough to overcome hydrodynamic forces, starting to maneuver. Consequently, the water droplets started to move towards each other and finally coalesced. The entire process occurred in less than 15 seconds

suggesting the fast response of the DDI mechanism if all of the requirements are met. **Figure** 3-2A shows the snapshots of droplets during this coalescence process.

Next, two water droplets were dispersed in the center of the oil medium along the corona tip, and each was touching the opposite electrodes (**Figure** 3-2B). Water droplets touching any electrode surface receive a free charge, which is given by equation (1-15).

However, it is to be noted that the amount of charges varies from point to point on the oil surface, and it depends on the surface potential as described in equation (3-4). Water droplets travel the gap between the electrodes to reach the opposite electrode due to Coulombic forces. Coalescence can happen in this gap due to the collision between the nearby water droplets or the attraction force between the neighboring oppositely charged water droplets. In the case of attraction, the force acting between the water droplets can be found from equation (1-17).

This force, responsible for electrocoalescence between two water droplets, is called migratory coalescence which is EP in nature and usually occurs in DC electric fields (or AC electric fields with a low frequency). Migratory coalescence should be considered when the water droplets succeed in keeping their charge long enough to pass the gap or at least halfway, depending on the relaxation time. In this experiment, the relaxation time (400 seconds) is high enough to guarantee water droplets traversing the gap between the electrodes and experiencing the migratory coalescence. According to equation (1-17) and comparing with equation (1-11), it can be concluded that migratory coalescence is significantly affected by the size of water droplets rather than their distance; however, the

DDI is mostly affected and manipulated by the distance between the water droplets rather than their sizes. On the other hand, with an increase in the strength of the electric field, both forces increase in two-folds in the migratory coalescence and the DDI phenomena. Consequently, the opposite charges were induced in the water droplets. They started to migrate from one electrode to another one; however, the signs of the charges do not agree, and the droplets attract each other and merge due to the coalescence process based on equations (1-17). Although the duration of the whole event was 20 seconds and it was higher than that observed time in the DDI process, it could be considered a fast response since the distance between the water droplets are relatively larger than that of the previous case.

Both DDI and migratory coalescence have been observed under a uniform electric field. When water droplets are very far, the uniform electric field is not efficient in enabling electrocoalescence. However, a non-uniform electric field forms while utilizing the corona discharge and the droplets exhibit different behavior. To examine this, another experiment was conducted. One water droplet was dispersed in the center and another at the right of the test cell (oil medium), where the electric field is weaker (**Figure** 3-2C). In a conventional electrocoalescence where the electric field is uniform, there is no chance of coalescence of these two water droplets. Due to the considerable distance between the droplets, neither DDI nor migratory coalescence can be activated. DEP could simply be translated as the motion of matter due to the polarization effect in a non-uniform electric field. Unlike EP that the movement in an electric field is dependent on charged particles,

the motion in DEP results from the difference in the dielectric constant of materials in the electric field, the materials with the higher dielectric constant move toward stronger electric fields. Since the induced water droplet dipoles have a limited charge in an electric field, they align with the electric field lines. However, in a non-uniform electric field, one side of the dipoles is always exposed to the higher electric field rather than the other sides. In this case, the net force is not zero, and the dipole moves towards the regions with stronger electric fields. Also, it should be noted that the DEP force does not depend on the direction of the electric field and the dipole moves in the same direction even if the direction of the field is reversed and can be described by equation (1-18).

The non-uniform distribution of the electric field component described in equations (3-4) and (3-5) can result in the non-zero value of the electric field gradient in the above equation. The DEP forces move the water droplets toward space with the stronger electric field in a collective way and increase the effect of the DDI and the EP. The DEP can significantly enhance the performance of coalescence, especially in dilute emulsions. Also, the DEP can still be seen in charged water droplets due to either partial charging when being in contact with the electrodes or discharging based on the oil relaxation time. At the beginning of this experiment, the water droplets were bouncing in the oil medium between its top surface and the ground electrode during the discharge exposure. This behavior, also known as a ping-pong motion, was found in some other applications in literature but not in the coalescence field [192]. It is hypothesized that when the EP starts, it is the main force that manipulates the motion of the water droplets inside of the oil medium. The observed

secondary force was DEP, the effect of which can be expressed as two components in the vertical and horizontal axes. With a non-uniform electric field induced via corona discharge, the field is stronger close to the surface in the vertical direction, and the direction of the DEP is upward. This observation confirms the electric field distribution that is expressed in equations (3-4) and (3-5). The velocity of the water droplets in the upward direction was faster than that of the downward motion even though the gravity force agreed in that direction. Ultimately, the horizontal component of the DEP was responsible for the coalescence. The electric field became stronger by approaching the center of the test cell; therefore, the direction of the DEP was towards the center. The center droplet was already exposed to the strongest electric field, and it did not have any motion in the horizontal direction. The right-hand side droplet was exposed to the weaker electric field and exposure of the DEP force pushed it to the center of the test cell, decreasing the distance between the two droplets. This process increased the chance of collision, activating the Coulomb's force between two droplets, as expressed in equation (1-17). Coalescence was initiated once the water droplets with opposite charges were sufficiently close to attracting each other due to the attraction force between two opposite charges, leading to a collision between them. This process took 7 minutes and 50 seconds to complete, which was dramatically longer than those observed in experiments described in **Figure**s 3-2A and 3-2B. However, merging two distant droplets would not be possible if the electric field was uniform, which typically occurs in conventional electrocoalescence methods. This

indicates the effectiveness of utilizing a non-uniform electric field for the coalescence of faraway droplets that is observed using a contactless corona discharge.

Finally, both water droplets were dispersed on the right side of the corona needle/test cell where the electric field is very weak (**Figure** 3-2D). Similar to what was observed in **Figure** 3-2C, water droplets exhibited bouncing between the two electrodes. The effect of the DEP was still observed, and the two water droplets started to move toward the center of the test cell. Coalescence was triggered when the distance between two water droplets was short enough to activate the migratory coalescence mechanism, leading to their attraction to each other. This event took 7 minutes and 10 seconds, and it was relatively similar to what observed in **Figure** 3-2C, suggesting that the effect of the DEP on coalescence is independent of the distance between water droplets and only depends on the strength of the electric field, where the droplets are placed.

3.3.2 Coalescence of multiple water droplets in oil medium

In order to investigate the effect of corona discharge on the coalescence of more droplets collectively and to confirm previously-observed phenomena, twelve droplets of deionized water (10 μL each in volume) were dispersed randomly in the cell and were exposed to a corona discharge induced by a 4 kV applied voltage (**Figure** 3-3A). As corona discharge initiates, DDI starts to dominate all the coalescence events in the first 20 seconds. This force affected all the adjacent water droplets leading to the formation of larger droplets. Beyond this time, by forming larger droplets, the distance between the water

droplets increased, and the rating of the DDI-induced coalescence decreased. After 10.9 seconds, the larger water droplets on the top touched the surface, receiving a positive charge, and started moving toward the ground electrode. From this point, migratory coalescence started to become the dominant mechanism for the rest of the process. The formation of the larger water droplets after 46.8 seconds enhanced de-emulsification since the small water droplets could easily suck into the interface of the larger droplet. The last water droplet, which also was the far-off water droplet from the center, merged nearly after 6 minutes as the effect of both EP and DEP.

Figure 3-3B shows normalized mean droplet volume defined as the ratio of average water droplet diameter (volume-weighted) to its initial diameter (~ 2.67 mm) versus time for the first 360 seconds after applying corona discharge. This graph can be divided into two sections: the first 20 seconds, which was dominated by the effect of DDI, and it can be considered relatively fast, and the second part from 20 seconds to the complete coalescence, which was dominated by migratory coalescence and the DEP-induced movement. The second part is quite slow due to the distance between water droplets, but the effect of the DEP is promising for the complete coalescence of all droplets and enhancing the overall performance. In addition, it should be noted here that the DEP helps to form larger droplets in the center, which can enhance the performance of the coalescence by sucking the smaller water droplets in the affected neighboring regions. Overall, the results obtained observing multiple droplets confirm the findings of two droplet

coalescence and suggest the effectiveness of applying a non-uniform electric field via corona discharge on the separation of emulsions.

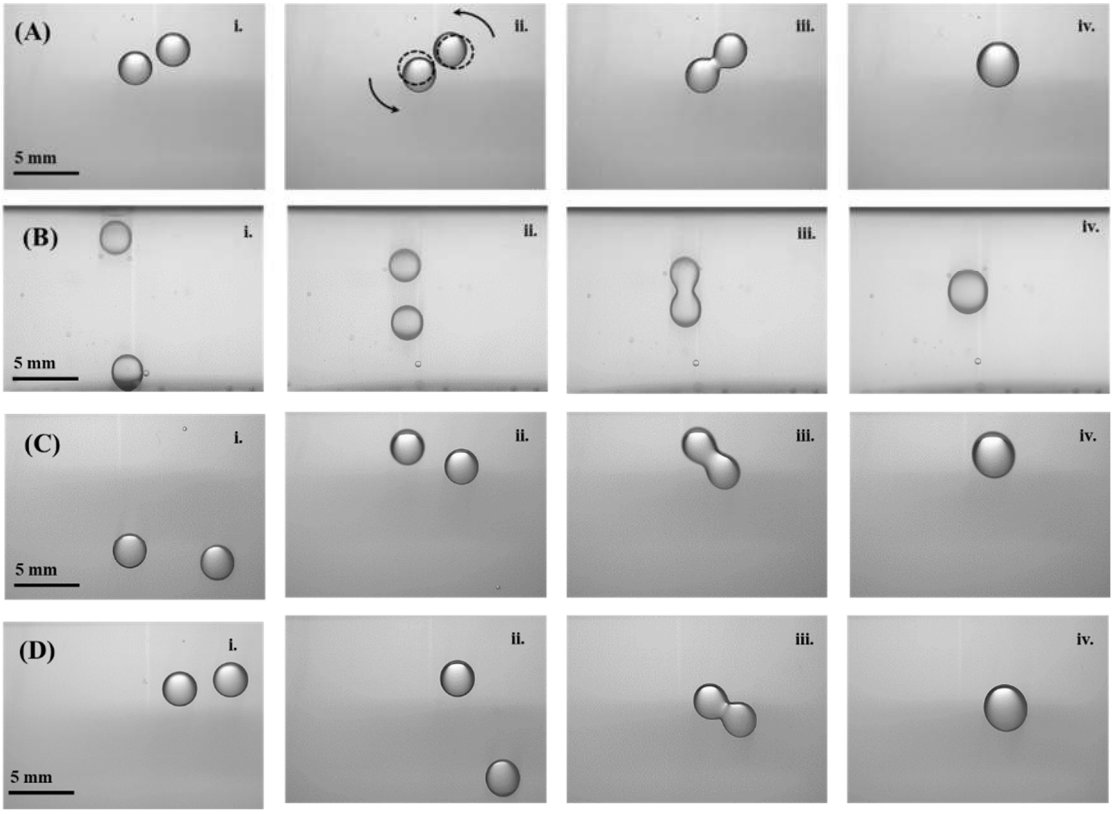

Figure 3-2 Impact of DDI, migratory coalescence, and DEP force on the coalescence of two water droplets in an oil medium. Two ten µl deionized water droplets were dispersed in four different positions/orientations (A-D) inside a test cell containing silicone (oil 3000 cSt viscous). In (A), the distance between the water droplets was close enough to activate the DDI mechanism immediately. In this case, the tangential (angular) component (equation 1-12) caused the rotation of the dipoles; then, the radial component (equation 1-11) reached the positive value and coalesced. In (B), the two water droplets were in the center and far from each other, and the DDI had a small effect on attracting water droplets. The upper water droplet first touched the top surface of the dielectric, acquired charges, and moved toward the opposite electrode, due to the effect of EP. The lower water droplet was polarized. The charge induced in the top surface did not agree in sign with the moving droplet, which caused attraction in the neighboring region and coalesced after the collision.

(C and D) none of the above mechanisms were activated in the first place, and droplets started bouncing between the two electrodes because of EP, but as an effect of DEP, they moved to the center of the test cell and coalesced.

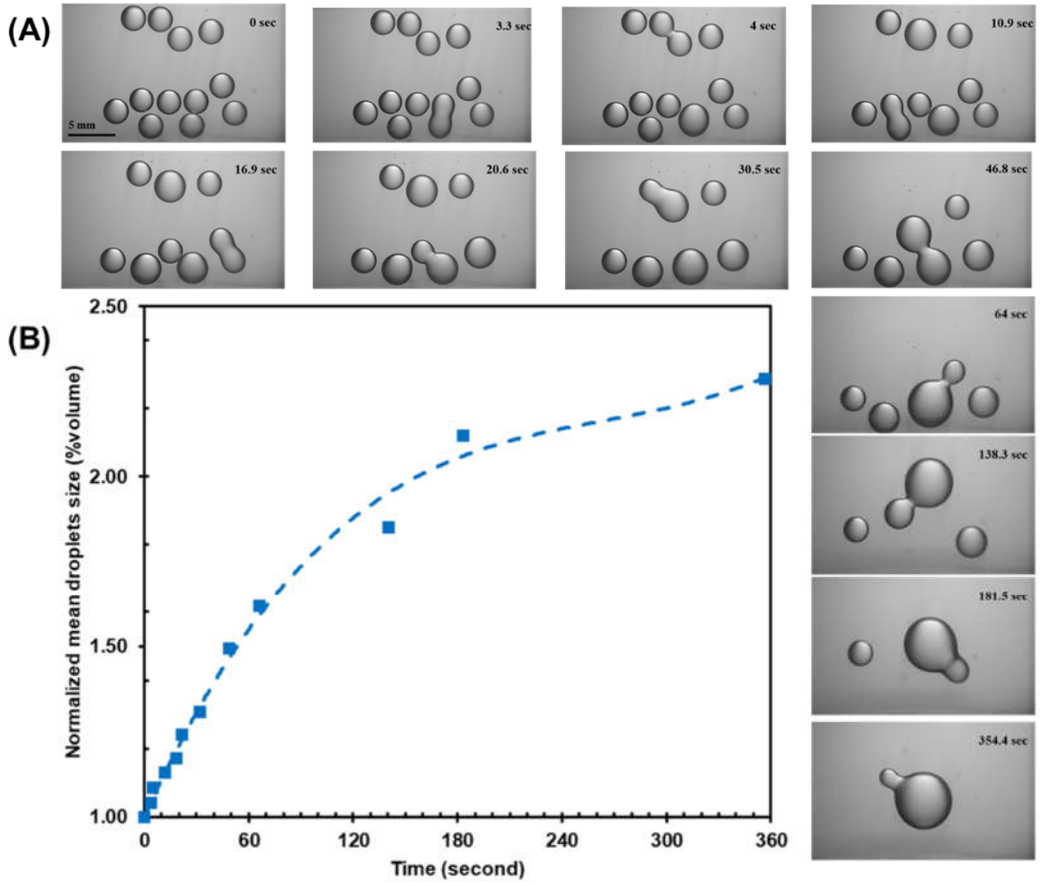

Figure 3-3 (A) Twelve ten µl deionized water droplets were dispersed in the test cell. DDI showed a rapid response to the applied electric field (4 kV) and was responsible for all coalescence events in the first 20 seconds of treatment with corona discharge. The second mechanism of the coalescence was activated when the first water droplet touched the top surface of the dielectric. Subsequently, the migratory motion was the main reason for coalescence events, so-called migratory coalescence. The DEP force increased the rate of coalescence by gathering the far-off water droplets in the center and is involved in coalescence events after 138 seconds of treatment. **(B)** A normalized mean droplet size (volume-weighted) vs time. This plot shows a rate of coalescence, which decreases gradually over time, changing the mechanism of coalescence from DDI to migratory coalescence. Although the rate of coalescence is decreased in migratory coalescence, it still

is a promising mechanism since the normalized water droplet size increased from 1.25 to 2.25.

3.3.3 Coalescence of many water droplets in water/oil emulsion

To investigate the effect of the corona discharge on a real emulsion, a W/O emulsion (2% water content by weight in 350 cSt viscous silicone oil) was prepared and then transferred to a cell in three batches and was exposed to a 7 kV corona discharge for 20, 60, and 120 seconds. An applied voltage of 7 kV was selected to ensure that the surface potential is above the critical voltage, enabling observation of the electroconvection phenomenon and its effect against potential chain formation. One sample without treatment was kept as a control sample. **Figure** 3-4A shows the effect of different treatment times on the size of the water droplets. The size of the water droplets significantly reacted to the treatment time in which the larger droplets corresponded to more corona treatment time. It is evident that only 20 seconds of corona treatment leads to considerable coalescence of water droplets in the emulsion. **Figure** 3-4B shows the same samples (both treated and untreated) after 24 hours in shelf conditions. The untreated emulsion appears to be milky without a considerable sign of separation even after 24 hours. However, the treated emulsions continue to separate further even after the corona discharge; this is despite having smaller-sized water droplets when compared to the untreated emulsion. We believe that the induced charges in the emulsion due to the corona discharge are contributing to shelf condition separation and sedimentation of the water droplets, significantly beyond what could be achieved without any treatment. Also, the effect of the residual charges in

the mixture is negligible since comparing the control sample with the samples treated for different times does not show any sign of stability on all of the treated samples after 24 hrs. Furthermore, using the higher voltage causes the motion inside of the oil inside the test cell, which was symmetrical on both sides vs the location of the corona needle (tip). The movement of the charged droplets made a flow pattern in the center from the ground electrode toward the surface (positive electrode). This motion can be amplified as a result of the ionic wind on the oil surface [148, 186]. Initiating such a motion can also enhance the performance of the coalescence due to increasing the chance of collision between the water droplets [193] and preventing/breaking chain formation inside the emulsion.

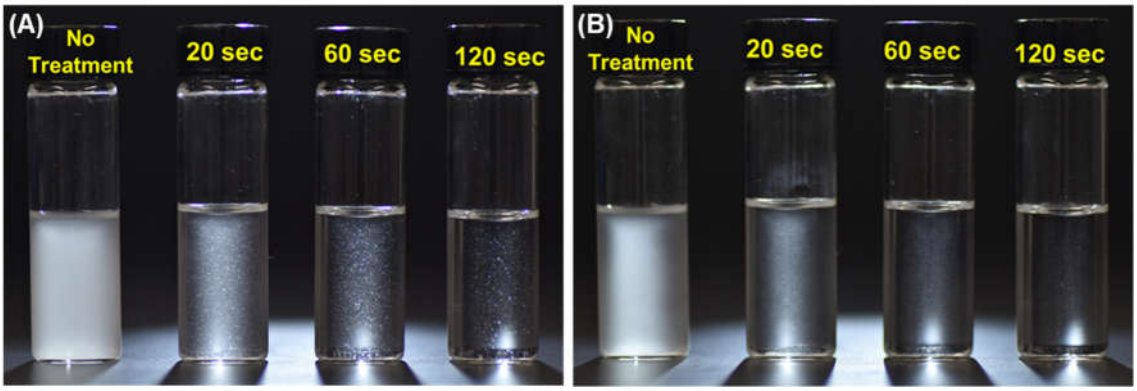

Figure 3-4 Effect of the corona discharge on the concentrated emulsion. **(A)** The effect of different corona treatment times (from left to right: no treatment, 20, 60, and 120 seconds of treatment, respectively) on the W/O emulsion (2% water content by weight in silicone oil with a viscosity of 350 cSt). The size of the water droplets gradually increased over the treatment time. **(B)** The samples from (A) after 24 hours in shelf condition. Forming larger water droplets after corona treatment helps the separation of two phases by accelerating the sedimentation of the water droplets at the bottom of the vials. The sample with the highest treatment time (120 seconds) was nearly separated into two distinct phases.

3.3.4 Diluted emulsion

The average distance between the water droplets in a diluted emulsion is relatively higher when compared to the size of the droplets. As a result, water droplets cannot build up enough interaction energy to attract each other. In addition, the existing nanodroplets in the emulsion make the separation process even more problematic because of the lower electrical forces and the lower sedimentation time. Experiments were carried out to evaluate the effect of corona discharge on emulsion with less than 0.1% water content by weight. Four treatment times (0, 20, 60, and 120 seconds), three applied voltages (4, 7, and 10 kV), and three different viscosities of silicone oil (100, 350, 650 cSt) were studies evaluating the effect of these parameters on the coalescence rate. The initial size distribution at the beginning of the test was considered as a baseline for a comparative evaluation purpose. The natural coalescence of the emulsions has a limited response on time, and the size distribution slowly shifted to a larger size over 4 hours (see **Figure** 3-5A). When the emulsion of silicone oil (100 cSt viscous) was exposed to a 7 kV corona discharge, the volume-weighted size distribution showed a rapid response to the corona treatment. Not only the average size was shifted but also tiny water droplets in the scale of nano coalesced and formed larger droplets in the scale of macro, without leaving residual droplets (see **Figure** 3-5B).

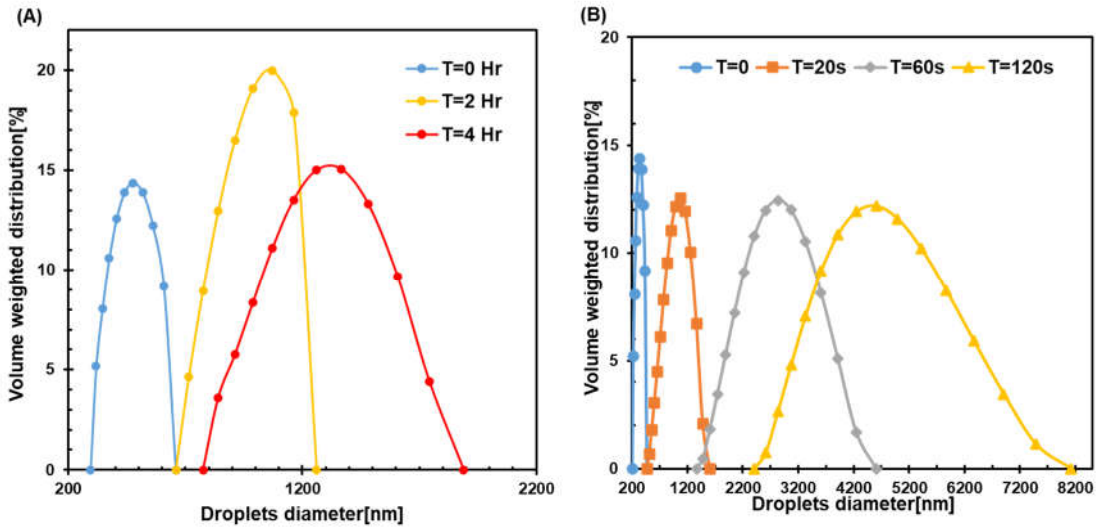

Figure 3-5 Effect of corona discharge on the diluted emulsion. **(A)** Changing in the droplet size distribution of diluted emulsion, including silicone oil with 100 cSt viscosity versus time without corona treatment over 4 hours. The peak volume was ~ 460.8, 972.6, and 1266.7 nm for T=0, 2, and 4 hours, respectively (**B)** Changing in the droplets size distribution of diluted emulsion including silicone oil with 100 cSt viscosity versus time. The peak volume-weighted size was ~ 460.8, 989.3, 2756.8, and 4619.6 nm for T=0, 20, 60, and 120 seconds, respectively (exposed to a 7 kV corona discharge). The size gradually shifts to larger sizes without tiny residual droplets.

Figure 3-6A shows the effect of the electric field strength on the rate of coalescence. The water droplet sizes immediately responded to the applied electric field, and the size of water droplets increased over time. The highest electric field corresponds to a higher coalescence rate. At the highest applied electric field (10 kV) and after 60 seconds of treatment, the rate of the coalescence decreased, and then it reached the limit range of the DLS size, above which the size of the droplets cannot be measured by this method. The curve no longer follows the linear trend observed in other experiments and

seems to be polynomial. These findings agree with the quantitative analysis results shown in **Figure** 3-4B, suggesting that the initial rapid response was due to the DDI and the slower response was due to the DEP and migratory coalescence.

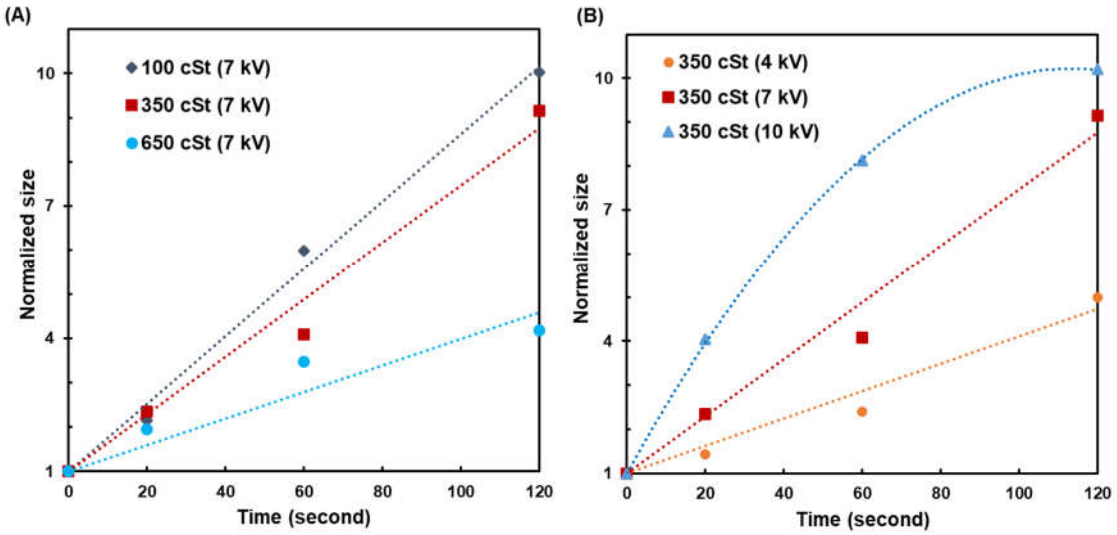

Figure 3-6 (A) Normalized water droplet size against corona treatment time in diluted emulsion (350 cSt) for different applied voltages. The higher voltage corresponds to the faster coalescence rate. The polynomial curve suggests a transition from DDI to migratory coalescence mechanisms using 10 kV voltage. **(B)** The effect of the different oil viscosities on the coalescence rate. Lower viscosity resulted in a faster rate with the same treatment conditions.

The results were also compared with conventional electrocoalescence via a uniform electric field in the literature. As an instance, Williams et al. [88] used a 4 kV voltage and formed a uniform electric field to separate 0.1 % W/O emulsion with silicone oil viscosity of 1cSt. They observed electrocoalescence via enlargement of water droplets reaching a diameter of approximately 1.6 normalized sizes (after 30 seconds) and saturating afterward

without any further increase in size. Here, we used a much viscous silicone oil (350 cSt vs. 1 cSt) and showed continuous and more rapid coalescence verified by an increasing trend in the size of the water droplets as a function of processing time. We observed water droplets reaching 1.6 normalized sizes only after 20 seconds of treatment and continuously enlarging to 5 normalized sizes after 120 seconds, without any sign of saturation in coalescence trend/behavior. This continuous coalescence of water droplets in the diluted emulsion is due to the presence of the DEP forces formed by the non-uniform electric field induced via corona discharge. The DEP forces decrease the distance between the water droplets by bringing them to the center of the test cell, leading to an overall enhancement in the coalescence/separation process. It is to be noted that this improved coalescence behavior occurred while the viscosity of our silicone oil (350 cSt) is significantly higher than the one reported by Williams et al. (1 cSt). This is notable considering higher drag forces and resistance to motion of water droplets when aiming to move in more viscous oil mediums. The experiment conducted on emulsions with various viscosity oils exhibited the volume distribution normalized to the initial value (**Figure** 3-7A). In all cases, shifting to larger water droplets was observed; however, by increasing the viscosity, the rate of the coalescence decreased as expected due to the hydrodynamic drag force and damping force exerted by the squeezed fluid film (i.e., oil layer) between the approaching droplets [114]. A small decrease in the coalescence rate was observed when oil viscosity in the emulsion increased more than three times (from 100 cSt to 350 cSt). This suggests the dominant effect of the electric forces overcoming hydrodynamic forces that are induced by viscosity.

After 120 seconds of treatment under a 7 kV applied voltage, the size of the water droplets reached the same size as the emulsion treated under a 10 kV, although no rapid increase in water droplet size was observed (**Figure** 3-6A). **Figure** 3-7A shows the electrical power consumption during the discharge. The power was calculated based on measuring current and applied voltage over time ($P=V.I$). The consumed power with 10 kV applied voltage is nearly two times the one experienced with the 7 kV voltage, suggesting an optimum operating condition for efficient electrocoalescence and less power consumption using corona discharge. The oil with higher viscosity consumed less power compared to the one with a lower viscosity due to the lower convective flow inside the emulsion with more viscous oil (see **Figure** 3-7B). In other words, increasing the voltage resulted in increasing the coalescence rate in the emulsion to a point in which the convection motion increases without increasing the coalescence rate. This undesired convection motion causes more power consumption and poor electrocoalescence performance. This behavior needs to be considered in search of the best recipe for separating emulsions with different oil viscosity values and overweighed against chain inhibitor behavior.

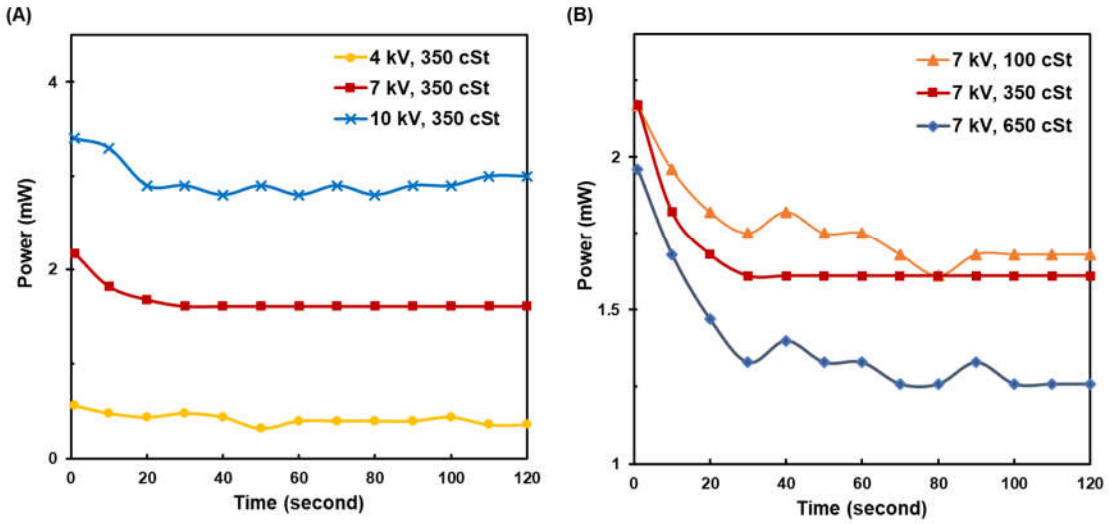

Figure 3-7 (A) Power consumption of the case (B); the consumed power increases nonlinearly by increasing the voltage with a jump from 4 kV to 7 kV applied voltage, suggesting the electroconvection effect. **(B)** Effect of viscosity on power consumption; less viscosity of continuous phase (oil) corresponds to higher power consumption.

3.4 Conclusions

A contactless method of emulsion destabilization is presented utilizing a corona discharge that induces a non-uniform electric field in the emulsion. First, a qualitative analysis was conducted via monitoring coalescence patterns of multiple macro size water droplets (diameter of ~ 2.67 mm) inside an oil medium, captured using a high-speed camera. We found that dipole-dipole-interaction (DDI), migratory coalescence, and dielectrophoresis (DEP) are three major phenomena that induce coalescence of water droplets. While DDI is playing a major role in the initial attraction of water droplets, the migratory coalescence is

enabling the collision or attraction of oppositely charged water droplets. However, the DEP is increasing the coalescence rate by bringing the water droplets to the center due to the non-uniform electric field, that is created by the corona discharge as a key feature of our separation approach. Next, a quantitative analysis was performed to study the impact of corona discharge on the coalescence of water droplets in micro/nanoemulsions using dynamic light scattering (DLS) measurements. We showed that increasing input voltage and lowering the oil viscosity result in a faster coalescence rate, while power consumption increases nonlinearly by an increase in the input voltage. Finally, we found an optimum operating condition for power-efficient electrocoalescence and separation, utilizing the corona discharge. This suggests that our method can be tailored for efficient separation of emulsions with given oil properties.

Some common separation methods such as centrifugation and membrane separation are not energy-efficient and/or environmentally friendly and are incapable of separating a wide range of oil and water emulsions while often involving installation and operation complexities [157-161, 166]. The contactless nature of our separation has several advantages over current methods used in industries. Simplicity in setting up and starting the process and minimal need for maintenance make our approach a reliable alternative for remote and off-site applications where mobility, flexibility, and time-efficiency are needed. Unlike traditional electrocoalescence, the anode (sharp conductive needle) in a positive corona discharge is contactless (not connected directly to the emulsion) and consequently does not experience electrolytic corrosion. Besides, the air gap between the needle and the

liquid (W/O mixture or emulsion) acts as a dynamic overcurrent resistor to protect the electrocoalescer against short circuits, due to bridge formation between water droplets. The corona discharge is a room-temperature process (cold discharge); however, for extra safety in contained working conditions, nitrogen or other inert gases could be used to create ions and separate water from oil. The risk of attaching water droplets to an electrode and forming tiny droplets due to cone formation is also decreased since the number of wetted electrodes is reduced to one (just cathode electrode is in contact with the medium).

In the future, our contactless electrocoalescence method can be scaled up for bulk separation of high-volume emulsions by designing and adapting a wire and/or a grid electrode configuration. In addition, further study could focus on the electrocoalescence of nanoemulsions stabilized using surfactants. Besides, it is recommended for future works to form corona discharge in inert gases (i.e. nitrogen or argon) instead of air and study their impact on oil/water separation using the geometry of multiple electrodes.

3.5 Materials and methods

A high-speed camera (Olympus TR *i*-speed) capable of up to 10,000 fps combined with a macro photography lens (Tamron 90mm 1:2.8) was used to capture the side-videos and images (at 10 fps for droplets and 30 fps for emulsion experiments. The high voltage amplifier (TREK Model 10/10B-HS) was connected to a DC power supply (BK 1698), which was used as a reference to the high voltage amplifier. The amplifier can generate high voltage DC (both positive and negative) and AC by 1:1000 ratio. In these experiments,

the positive DC was only used to generate corona discharge to avoid direct contact of the anode to emulsions and protect the electrode against corrosion. **Figures** 3-8A and 3-8B show a tungsten needle before and after 100 hours of corona discharge service under a high-resolution optical microscope without any sign of corrosion. The current was actively monitored by connecting the Keithley 2100 digital multimeter to the HV amplifier.

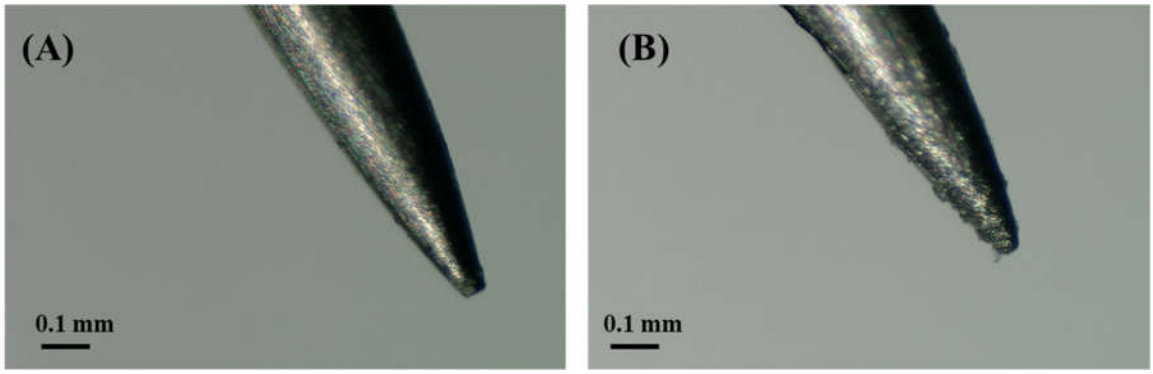

Figure 3-8 (A) Shows polished tungsten needle before exposure to the corona discharge. **(B)** Shows the same needle after 100 hrs discharge without any sign of corrosion.

To understand the fundamentals of coalescence by the corona discharge, 10 µL water droplets (Deionized water, Sigma-Aldrich, Diameter ~ 2.67 mm) were dispersed through a steel needle using a ramé-hart Automated Dispensing System (Model P/N 100-22) with an accuracy of ± 0.002 µL. The water droplets directly sunk into the large cubic quartz cell with the size of 30×30×30 mm (W×D×H) and a 1-inch copper disk fixed to its bottom, acting as a grounding electrode. The test cell then filled to 15 mm height with 3000 cSt silicone oil (obtained from Hudy). The corona gap (t) was kept constant at 10 mm

to assure that the ionic wind created by the corona discharge can reach all oil surfaces based on Warburg's law.

To examine the effectiveness of the corona discharge on emulsion separation, two types of W/O emulsions were prepared using different processes. The first type of emulsion consisted of the 2% water and 98% silicone oil (350 cSt viscous obtained from MicroLubrol) content by weight agitated for 5 minutes by magnetic stirrer at 2000 rpm, followed by 5 minutes of mixing with a homogenizer (Waverly model H-100) at 4000 rpm. Then, the emulsion was transferred to a transparent plexiglass cell with the size of 25×10×30 mm (W×D×H). The homogenizer rpm and the mixing time were experimentally obtained in a way that enables us to have a proper droplet size range for optical observation of the electroconvection, chain formation, coalescence, and sedimentation using a regular camera. In the second type of emulsion, the pre-weighted water and oil (less than 0.1 weight percent water in oil) were mixed in a beaker by magnetic stirrer (BIPEE model SH-2) at 2000 rpm for 5 minutes at room temperature (Temparature= 25 °C for both emulsions), followed by a final mixing by the homogenizer at 6000 rpm for 20 minutes. After that, the emulsions were transferred into customized size 20×20×30 mm (W×D×H) plexiglass cell and exposed to corona discharge. The sample preparation process was experimentally set in a way that emulsions with a small and uniform dispersion of water droplets suitable for the DLS measurements were obtained, repeatedly. The dielectric medium in these experiments was silicone oils with three different viscosities of 100, 350, and 650 cSt (obtained from MicroLubrol and XTR). The oil conductivities were measured with a

rudimentary setup using standard 4 mm electrophoresis cuvettes as test cells. The conductivity of silicone oils with different viscosities was found to be ~ 6×10^{-12} S/m and close to that expected. For each set of experiments, these emulsions were made separately, following the same procedures mentioned above. Water droplet size distributions were quantified using the DLS instrument made by Anton Paar model Litesizer-500 (Measuring range: 0.3 nm – 10 μm particle diameter). The DLS determines the size of water droplets based on their refractive factor compared to the oil medium. Samples were uniformly extracted from all sides of each cell to ensure that the results represent real size distribution in each emulsion.

Chapter 4

4 An optimum operating frequency for electrocoalescence induced by pulsed corona discharge

4.1 Abstract

Current oil-water separation methods require significant power, high processing time, and costly equipment which typically yields low treatment efficiency. Pulsed DC electric fields and recently non-uniform electric fields caught considerable attention in the petroleum industry research in order to address the most common oil-water separation issues such as chain formation, partial coalescence, and low efficiency in either energy consumption or coalescence rate. Here, a contact-less charge injection method induced by corona discharge is utilized to investigate the impacts of non-uniform and pulsed DC electric fields on the coalescence of water droplets inside an oil medium. The operating process parameters were experimentally calibrated and optimized with the goal of increasing the effectiveness and

energy consumption efficiency of the coalescence process. Different pulsed DC frequencies and pure DC waveform applied on water droplets in several geometries. High-speed imaging and image processing techniques were used in order to investigate the effect of different active forces (i.e. dipole-dipole interaction (DDI), migratory coalescence, or electrophoresis (EP), and dielectrophoresis (DEP)) during the coalescence process. An optimal coalescence recipe was proposed by continuous measurement of the distance, velocity, and acceleration of the coalescing water droplets and it is recommended to use pulsed DC for concentrated and pure DC for disperse emulsion.

4.2 Introduction

Many natural and synthetic products such as milk, petroleum, food products, drugs, paints, and many others are made from dispersing droplets of one fluid in another immiscible fluid, known as emulsions [194]. While emulsion formation is a challenging task in industries such as cosmetics and food, the separation process is important when there is a need to purify a liquid product, such as extracting water from crude oil and phase separation during solvent extraction [195-197]. Centrifugal separation, chemical demulsification, electrocoalescence, membrane separation/filtration, pH adjustment, and heat treatment are the most common separation processes depends on the application [198-201]. However, processes that utilize high-electric fields have been extensively used in water/oil separation, especially in the oil and gas industries. The importance of phase separation in these industries is that the emulsions are unwanted phases of extracts which increase the processing costs, transportation-related expenses, catalyst malfunction, damage to the equipment, and degrade product quality [202].

The focus of electrostatic demulsification processes has been on reducing the cost and energy while improving the quality of water/oil separation [92, 203]. Although these methods are promising, the commercially available electrocoalescers are costly to operate since they utilize large vessels to provide enough residence time (~30 minutes) needed for efficient separation of immiscible phases. More details of the currently available technology could be found elsewhere in the literature [204-206]. Providing a reliable and efficient design while meeting the compact dimension requirement in some industries is a difficult task, regardless of the target demulsification efficiency[207, 208]. Most of the current electrocoalescer designs utilize alternating current electric fields (AC electric fields) with frequencies in the range of 50-60 Hz. However using AC electric field showed limited response in later stage of coalescence due to increasing the distance between water droplets and decreasing electrocoalescence forces. Also, AC electric field consume more power because of capacitance effect of the oil and decreasing impedance of oil subject to electric field by increasing frequency [114]. On the other hand, the direct current electric fields (DC electric fields) have been less investigated while it is proved that the efficiency of the DC-based setups could be higher since they maintain the high electric field for the entire duration of the processing and higher motion of water droplets which increase the chance of collusion cause coalescence [88, 170, 209, 210]. However, using DC electric field activate other undesired behavior like chain formation. Berg et al. [211], have demonstrated that the tiny water droplets dispersed in an oil medium form a stable chain aligned with the external electric field. Since the water droplets form a chain, there is a

chance that the chain acts as a bridge and causes a short circuit, or form partially chain and reduce the electrocoalescence efficiency [114]. Also using DC electric field expose anode to electrolytic corrosion results to increasing the downtime and maintenance time [92]. Bailes et al. [212], have introduced an alternative that was implementing a pulsed DC electric field. They have found that the pulsed DC electric field has both advantage of AC and DC electric field and can maintain the electrocoalescence performance for entire process and reduce the chances of chain formation and enhances the efficiency of the electrocoalescence. In the 1980's they have investigated the different parameters affecting the efficiency of electrocoalescence in a pulsed DC electric field; they found that the pulse shape, frequency, and amplitude have major impacts on the coalescence events [213]. In addition, it has been reported that a protective coating layer on the electrodes results in canceling the electrolyte corrosion and also higher electrocoalescence efficiency by optimizing process parameters; however, the cost of the coating and its lifecycle maintenance was considerable [214, 215].

Aside from the type of electrocoalescence processes, it is crucial to understand the nature and fundamentals of the process in order to fully utilize the benefits. The two main schemes of coalescence of water droplets are known to be dipole-dipole interaction (DDI) and migratory coalescence. DDI takes place as a result of the interaction between polarized and aligned water droplets in an electric field at a close distance. The adjacent water droplets exert an attractive force to each other and after reducing the distance, lead to the formation of larger water droplets [216, 217]. On the other hand, migratory coalescence

which is electrophoresis (EP) in nature and observed in DC or AC with low frequency electric field is another type of coalescence in which charged water droplets in an electric field coalesce and form a larger droplet. The water droplets receive free charges when they touch any electrodes or other charged droplets (non-coalescence events); then, the newly charged droplets move toward the opposite electrode in the unit cell, based on their distance. This motion can trigger coalescence due to collusion between moving droplets or attraction force between opposite charged droplets. Finally results in a coalescence that yields larger water droplets which sediment faster, ultimately leading toward two separate phases [218, 219]. However, these two mechanisms are not completely distinct and might act together in a process of electrocoalescence. This means that to an extent that the water droplets can acquire charge (closer to the electrodes), one mechanism triggers, and when the water droplets get farther from the electrodes, another one becomes the main acting mechanism [220].

The performance of DDI and EP are correlated with strength of electric field and in general by intensifying electric field, the droplets coalesce faster. However, By increasing the strength of the electric field after some threshold, not only there is no increase in the coalescence event but also the breakup mechanisms are activated [221, 222]. There are three main mechanisms of water droplet breakup that are introduced by Williams and many other researchers [88, 223]. In the first one, the water droplet is polarized and elongated in presence of the effect of the electric field and starts to disintegrate into smaller droplets (when the electric field is strong enough in that region). In the second one, water droplets

can acquire free charges by coming to contact with electrodes and the charged droplets break up due to limitations on the amount of accumulated charge they can have (Rayleigh limit) if the electric field is strong enough. Finally, water droplets might get stuck to the electrodes which have higher potentials compared to the capacity of the water droplets. This high charge results in Taylor cone formation which disperses tiny droplets of water into the oil, acting against the separation intend [224].

Regardless of the distance to the electrodes, the uniformity of the electric fields is another important parameter that significantly affects the efficiency of electrocoalescence. The first implementation of non-uniform electric fields in electrocoalescence and water motion was conducted by Pearce [225]. Eow et al. [226], in another study, have investigated the effect of electrode geometry and other dynamic parameters on the electrocoalescence of two water droplets in an oil medium. In addition, they have investigated the effect of the direction of the electric field relative to the water droplets. In another research by the same group, the effects of liquid flow, electric field strength, and fluid flow rate on coalescence rate were investigated, concluding that the coalescence rate could be easily enhanced or disturbed by different elements of experiments particularly electrodes geometry [227]. Hoseini et al. have investigated the separation of oil droplets from water medium in the presence of a non-uniform AC and DC electric fields [228, 229]. Non-uniform electric fields can be generated using different electrode configurations which pin-to-plate is the most common one. However, the optimum geometry is still challenging due Joule heating effect on sharp edges or mechanical restriction [183, 230].

Although many other kinds of research may be found in the literature on the application of non-uniform electric fields in electrocoalescence, there are a few studies available in which the simultaneous effect of electric field non-uniformity and pulsed DC waveform was evaluated [94]. It is hypothesized that by combining these two features, the efficiency of coalescing performance increases. Here, this simultaneous effect was achieved utilizing a corona discharge.

Corona discharge is a type of cold plasma that could be useful in electrocoalescence. Thanks to their ability in ionization of gases and releasing radicals, cold plasmas have many different applications such as air purification and filtration, dust removal of airflows, bacteria removal in respirators, and electrohydrodynamic pumping. [186, 231-233]. Corona discharge is simply a high voltage discharge that reaches a point of differential energy that ionizes the air molecules. As a result, the corona discharge setups could be available in different forms of AC, DC, and pulsed DC [234]. Based on the orientation of the electrodes, the corona discharge could be named as either positive or negative corona discharge, from which the latter is utilized in most of the applications such as flow velocimetry and pressure sensors [235]. Corona discharge could be implemented in the field of electrocoalescence by charging the water droplets, build-up electric field, and consecutively, coalescence. The application of corona discharge in electrocoalescence can bring notable advantages compared to available methods, such as the contactless nature of corona discharge and its ability to form a non-uniform electric field. The performance of a DC non-uniform electric field induced by corona discharge for electrocoalescence was

discussed in the literature [236]. The main role of corona discharge is to ionize the environment around the discharge (mostly air molecules) and form charged ions moving toward a ground electrode. In order to have the ionizing regime between the electrodes, it is important to keep the voltage gradient high by utilizing a sharp tip electrode (a small surface area). Ions are created in the area close to the tip and accelerate toward the opposite electrode, forming an ionic wind. The ions can penetrate the surface of a liquid medium if it is in their path and they can be transferred either by conduction or convection and build-up a non-uniform electric field inside of the oil [237]. The presence of electric fields causes the electrocoalescence phenomenon in which the tiny water droplets in a W/O emulsion will coalesce and form a larger phase of water separated from the oil phase. As discussed earlier, increasing the strength of the electric field results in increasing the coalescence rate but an optimum range of the electric field should be utilized for maximum efficiency. In addition, it is crucial to understand the different types of acting forces and coalescence acceleration/deceleration mechanisms [185].

Coalescence (DDI or migratory) or break up (any of the three discussed above) mechanisms could be easily triggered by applying different experimental conditions. As a result, it is important to choose the best set of parameters in order to have the correct outcome with the highest efficiency. In this study, it is tried to have the coalescence of water droplets in a silicone oil medium under pure and pulsed DC electric fields. The experimental setup is schematically illustrated in **Figure** 4-1.

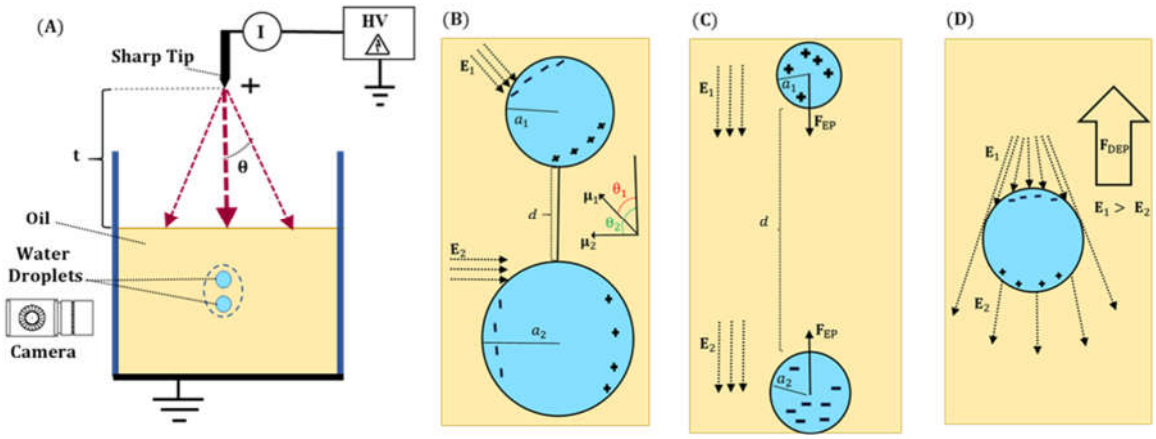

Figure 4-2 (A) Schematic showing various coalescence mechanisms of water droplets in 3000 cst silicone oil, induced via corona discharge that is formed by applying a high voltage to a sharp conductive electrode. **(B)** Two water droplets dispersed in the center of the cuvette, to examine the effect of dipole-dipole interaction and the imposed electric fields on their coalescence. **(C)** Aims to show migratory coalescence (electrophoresis) by dispensing a second water droplet when the first one reaches the ground electrode. Note that the droplets are far away when compared to the case (B). **(D)** Shows dielectrophoresis (DEP) force acting on a single water droplet, bouncing between the two electrodes under the corona discharge.

4.3 Materials and methods

A desktop experimental setup was assembled and utilized in order to study the impact of corona discharge on the coalescence behavior of water droplets in the oil medium (**Figure** 4-1). The setup has consisted of a high-voltage power supply with an amplifier, a sharp tungsten needle (purchased from Bovie Medical with a tip diameter of 65 um) acting as the working electrode, a lab jack holding the two-phase medium (water droplets dispersed in oil) and acting as the ground electrode, a measurement unit with the ability to measure

instantaneous currents. The experiments were monitored with a high-speed camera (Olympus TR i-speed) equipped with a photography lens (Tamron 90mm 1:2.8) which was capable of imaging up to 10,000 frames per second (fps). The high-voltage amplifier (TREK 10/10B-HS) was equipped with a function generator (SDG 1032X) that was capable of providing different waveforms and frequencies. The amplifier was capable of generating positive/negative high-voltage DC and AC by 1:1000 ratio with the highest frequency of 1000 Hz. However, in the experimental process, only the pure and pulsed DC waveforms were applied. For current measurement, a Keithley 2100 multimeter was connected to the high-voltage amplifier.

Different materials used in these experiments were mainly deionized water (Sigma Aldrich) and silicone oil (HUDY). An automated Ramé-Hart dispenser (P/N 100-22 with a maximum accuracy of ±0.002 μL) was used to disperse small water droplets (volume of 10 μl) with controlled volume into the silicone oil medium. The experiment cell was a quartz cube with a dimension of 30×30×30 mm3, filled with silicone oil 3000 cst up to 15 mm height (the maximum oil level). The quartz cube was equipped with a one-inch copper plate at the bottom surface that was connected to the grounding electrode (out of the experiment cell) through a tiny hole. With the help of a laboratory jack, the gap between the corona generating electrode (sharp tungsten needle) and the top surface of the oil in the cube was kept constant to a specific distance of t=5 mm for these sets of experiments. Finally, water droplets added to the silicone oil were treated by +6 kV pure and pulsed DC electric fields under different frequencies of 1, 10, and 20 Hz. The pulses duty cycles are

selected as 50% in all experiments by comparing the best results of 10%, 50%, and 90%. Also, pulse repetition frequency is equal to main waveform frequency to assure that the water droplets are exposed to maximum power injected from the pulsed DC waveform. The recorded videos were then converted to images and analyzed via digital image processing software packages (MIPAR) [60]. At first, the water droplets as a circle object were introduced to the software recipe, and secondly the circles were actively tracked over the corona discharge and all geometry data was recorded. All experiments were conducted in room condition (Temperature of 25 °C and Pressure if 1 atm). The results and the relevant discussions are presented in the following section.

4.4 Results and discussion

To study the impact of the non-uniform electric field on the coalescence of W/O emulsions, two water droplets (10 µl) were placed in silicone oil medium with the viscosity of 3000 cst under pure and pulsed DC (1, 10, and 20 Hz) electric fields. The electrocoalesence behavior of the water droplets was monitored under various operating frequency for both pure and pulsed DC electric fields. **Figure**s 4-2 (A) and 4-2 (B) show the normalized distance of two water droplets with specific process parameters of the distance between the droplets (d) over their initial distance (d_0), and their approaching velocity, respectively. It is hypothesized that the dipole-dipole interaction (DDI) is the main component of the acting forces on adjacent water droplets during the coalescence process [238]. The DDI forces are results of the interaction between two adjacent and charged/polarized water droplets in

tangential and radial directions. These forces could be calculated using the equations (1-11) and (1-17).

Depending on the angle of the droplets relative to each other and the distance between them, the magnitude of the force components changes. It is tried to have the two droplets dispersed in a way that they have the minimum angle between their vertical symmetry axis (ideally $\theta = 0°$) maintaining a distance of d= 6mm. Since the water droplets are polarized, a DDI force is formed between the close-enough water droplets. The DDI forces are the dominant reason for the coalescence of the water droplets in the initial steps of the process since the water droplets are initially close to each other. The DDI forces are in relation to the inverse of the 4th power of the distance between them ($F_{DDI} \propto d^{-4}$) and they lose effect in larger distances. This correlation can be clearly seen from **Figure** 4-2 (A) where the normalized distance of the water droplets is exponentially decreasing with time while the two water droplets get closer and the DDI forces become stronger. It is also shown that a decrease in the frequency of pulsed DC from 20 Hz to 1 Hz reduces the coalesce time of the droplets. However, the coalescence time of the sample under 10 Hz pulsed DC is comparable to that of pure DC. This is taken as a reference when comparing the performance of different electric fields in the coalescence of water droplets. The lower pulsed DC and pure DC showed similar behavior over the DDI experience and in general there is no significant change on the coalescence time. To further examine the coalescence behavior of water droplets, the relative velocity of the two approaching droplets was plotted vs. time in **Figure** 4-2 (B). The relative velocity of the approaching droplets significantly

increases with time, experiencing its maximum value just before the coalescence. This verifies the finding that stronger DDI forces exist as the distance between the droplets decreases. The fluctuations observed in the relative velocity suggest the presence of forces resisting the coalescence and acting in the opposite direction of the DDI forces. It is hypothesized that these coalescences resisting hydrodynamic forces are drag and film-thinning forces that arise from the fluid friction and squeezing of the oil between approaching water droplets. These forces result in local decreases in the relative velocity of the approaching droplets while the DDI forces continue to increase the overall trend of the relative velocity. The introduced damping forces are defined as [114, 239, 240]:

$$\mathbf{F}_{\mathrm{d}} = -6\pi\eta_{\mathrm{c}} a_1 \boldsymbol{V}_1 \quad \text{where} \quad \mathrm{d} > \mathrm{r} \tag{4-1}$$

$$\mathbf{F}_{\mathrm{f}} = \frac{-6\pi\eta_{\mathrm{c}}(\boldsymbol{V}_1 - \boldsymbol{V}_2)}{\mathrm{d}} \left(\frac{a_1 a_2}{a_1 + a_2}\right)^2 \text{ where } \mathrm{d} << \mathrm{r} \tag{4-2}$$

where $\boldsymbol{V}_1$ and $\boldsymbol{V}_2$ are droplets velocity and η_{c} is the dynamic viscosity of the continuous phase (i.e. oil). The interaction between these forces creates the fluctuation in water droplets' motion. Similar to the normalized distance versus time plot, the relative velocity plot shows comparable results under the pure DC and the 10 Hz pulsed DC electric fields. The reason for the delayed increase of the relative velocity under the 20 Hz pulsed DC electric field is that the droplets are not exposed to such a strong electric force to trigger their motion. It took nearly 16 seconds for the droplets to get close enough and excite the motion toward each other. In addition, the low relative velocity observed under 20 Hz pulsed DC is accompanied by few fluctuations in the relative velocity, verifying the presence of the drag and the film-thinning forces with their strength depending on the

velocity. The real-time sequences of the DDI coalescence of the two water droplets can be seen in **Figures** 4-2 (C) and (D). The graph shows that the sample under 1 Hz (fastest coalescence of all in 3.3 seconds) coalesces more quickly than the one under 20 Hz (slowest of all coalesce in 18.9 seconds).

Although it is discussed that the DDI forces act as the primary reason for enabling coalescence, increasing the distance of the water droplets diminishes the strength and effectiveness of the DDI forces in coalescence. However, when water droplets are relatively far, another type of force is responsible to increase the performance of the coalescer. These forces which are commonly known as electrophoresis (migratory coalescence) play a role when water droplets acquire free charges. The electrophoresis force between two charged water droplets can be expressed by equation (1-17) [237]:

while the electrophoresis forces act at larger distances when compared to those of the DDI forces, they are proportional to the inverse of the 2nd power of the distance of the water droplets ($\boldsymbol{F}_{EP} \propto d^{-2}$). Comparing this to the distance dependence of the DDI ($\boldsymbol{F}_{DDI} \propto d^{-4}$), it is evident why lowering the distance leads to two times enhancement of the DDI forces, when compared to the electrophoresis forces. The electrophoresis forces occur naturally in DC electric fields or AC electric fields with low frequencies [114]. Migratory coalescence takes place due to the traverse of the charged water droplets between the two electrodes based on the relaxation time of the silicone oil as the medium. The relaxation time determines whether the water droplets are able to keep their charge to travel at least half of the distance between the electrodes [237].

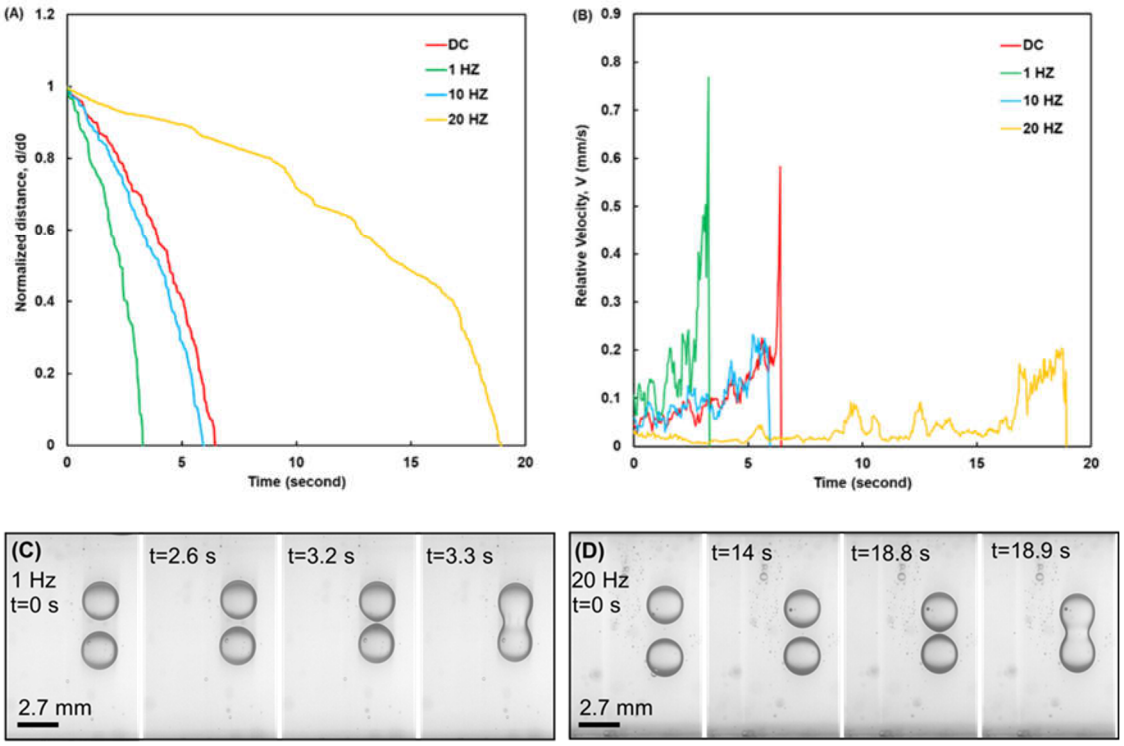

Figure 4-3 (A) Normalized distance of two nearby water droplets (10 µl) in 3000cst silicone oil vs. time for coalescence, that is induced by pure DC and pulsed DC (1, 10, and 20 Hz) corona discharge. **(B)** The relative velocity of the coalescing droplets vs. their coalescence time under pure DC and pulsed DC (1, 10, and 20 Hz) electric fields. **(C)** and **(D)** Snapshots of coalescing droplets via dipole-dipole interaction (DDI) induced by pulsed DC electric field with 1 Hz and 20 Hz frequency, respectively. All the experiments were conducted at + 6 kV voltage.

The whole process of migratory coalescence occurs due to the Coulombic forces. **Figure** 4-3 shows the migratory coalescence behavior of two far-away water droplets in silicone oil under pure and pulsed DC electric fields of +6 kV. The Coulomb force due to electrophoretic phenomenon results in the initial attraction of the water droplets since the initial distance between the water droplets is further than what is needed to have effective DDI forces. Unlike close water droplets, the pure DC electric field is more effective in the

attraction of faraway water droplets when compared to the pulsed DC electric fields. The highest efficiency of the coalescence is yielded under a pure DC electric field and for all the pulsed electric fields the coalescence occurs slower. Since the behavior of the coalescence process is not proportional to the frequency of the electric field, it is crucial to have the optimum working frequency while utilizing a pulsed DC electric field. As can be seen in **Figure** 4-3 (A), the coalescence efficiency of the sample under 10 Hz is the highest while the ones under 1 and 20 Hz are less efficient. Despite of the DDI experiences, there is less similarities between the coalescence time of pure DC and lower pulsed DC frequency electric field, it seems that it is directly correlated with duty cycle of waveform (%100 compare to pulsed DC %50). The amount of electric field charge transferred during touching process is the main factor to manipulate water droplets during migratory coalescence. From **Figure** 4-3 (B), it can be concluded that the fastest coalescence takes place under a pure DC electric field. The behavior of the samples under a pulsed DC electric field is different in a way that in all cases, the relative velocity increases gradually and does not reach the highest peak provided by the pure DC electric field. Similar to the trends in the normalized distance in **Figure** 4-2 (A) it can be seen that there is a need to optimize the working frequency of the electric field in order to enhance the efficiency of coalescence. The coalescence time of the droplets under the 10 Hz pulsed DC is close to that observed under the pure DC electric field, while the ones under 1 and 20 Hz are noticeably slower. The real-time sequences of coalescence of the droplets treated under

pure and pulsed DC (20 Hz) electric fields as the fastest and the slowest coalescence processes are presented in sections **Figure** 3 (C) and (D).

In comparison to the coalescence time of pure DC treated samples, it is obvious that the coalescence occurs nearly four times slower in the samples treated under a pulsed DC electric field (20 Hz). The real-time images are in accord with the experimental results plotted in this Figure. The slope of the relative velocity graph (**Figure** 4-3 (B)) represents a relatively water droplets acceleration. The slope in the sample treated under a pure DC electric field is the highest acceleration. This fact can also translate to the highest net force acting on the water droplets. Also, this high acceleration is reflected in the high relative velocity of the water droplets in the pure DC electric field at the early stages. Since the droplets are fully charged at the beginning of the coalescence process, they experience the highest electrophoresis forces and highest accelerations. However, the slope decreases over time since the water droplets are discharged in the dielectric (silicone oil) medium and the Coulomb force decreases. The increase of the relative velocity is limited due to the increase of opposite hydrodynamic forces (equation 4-1 and 4-2). The relative velocity fluctuation in the samples treated under pulsed DC electric field is negligible through the beginning of the process to the three-quarters of the distance but after that, the fluctuation starts.

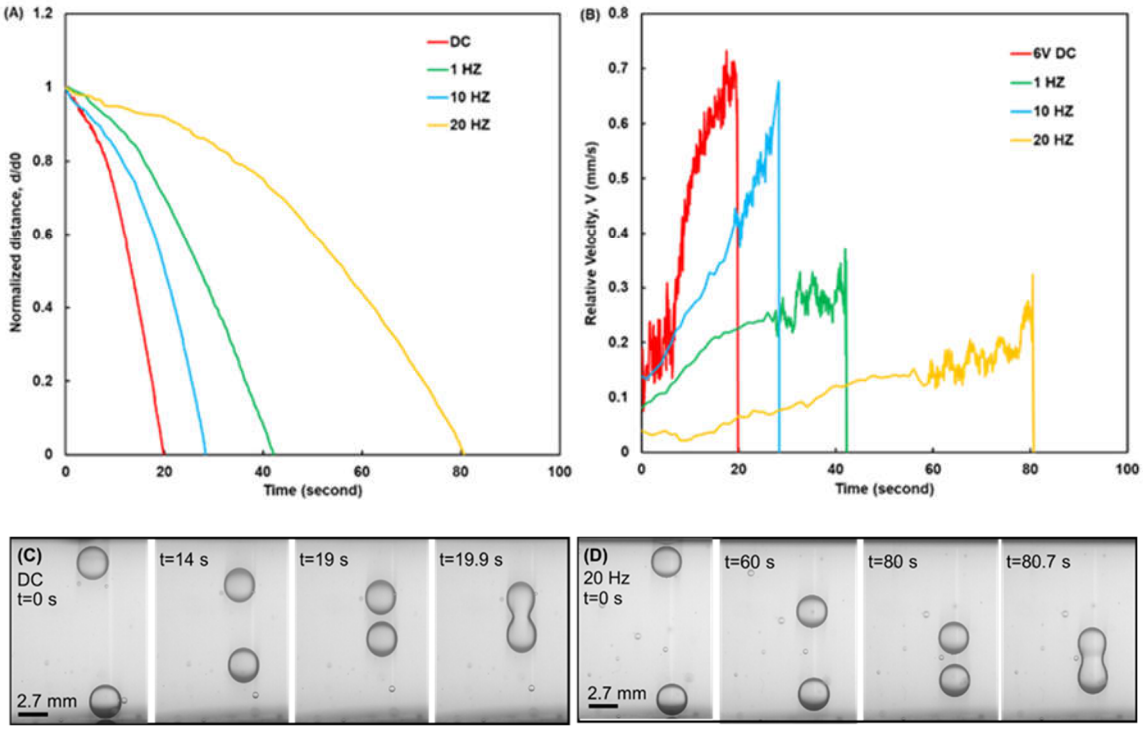

Figure 4-4 (A) Normalized distance of two far-away water droplets (10 µl) in 3000cst silicone oil vs. their coalescence time, induced by pure and pulsed DC (1, 10, and 20 Hz) electric fields. **(B)** The relative velocity of the droplets in motion toward each other vs. their coalescence time under pure and pulsed DC (1, 10, and 20 Hz) electric fields. **(C)** Migratory coalescence (electrophoresis) observed from snapshots of two far away droplets under 1 Hz pulsed DC electric field. **(D)** Migratory coalescence sequences of the same droplets in (C) under 20 Hz pulsed DC electric field. All the experiments were conducted under +6 kV.

At the endpoint of the graphs where the distance is close to zero, the coalescence regime transforms from the migratory coalescence to the DDI. **Figure** 4-4 compares acceleration between approaching water droplets in silicone oil under pure DC and pulsed DC electric fields and also under both DDI and EP experiments. In DDI cases (**Figure** 4 (A) and 4 (B)), the pulsed DC treated sample shows higher acceleration over the entire coalescence course.

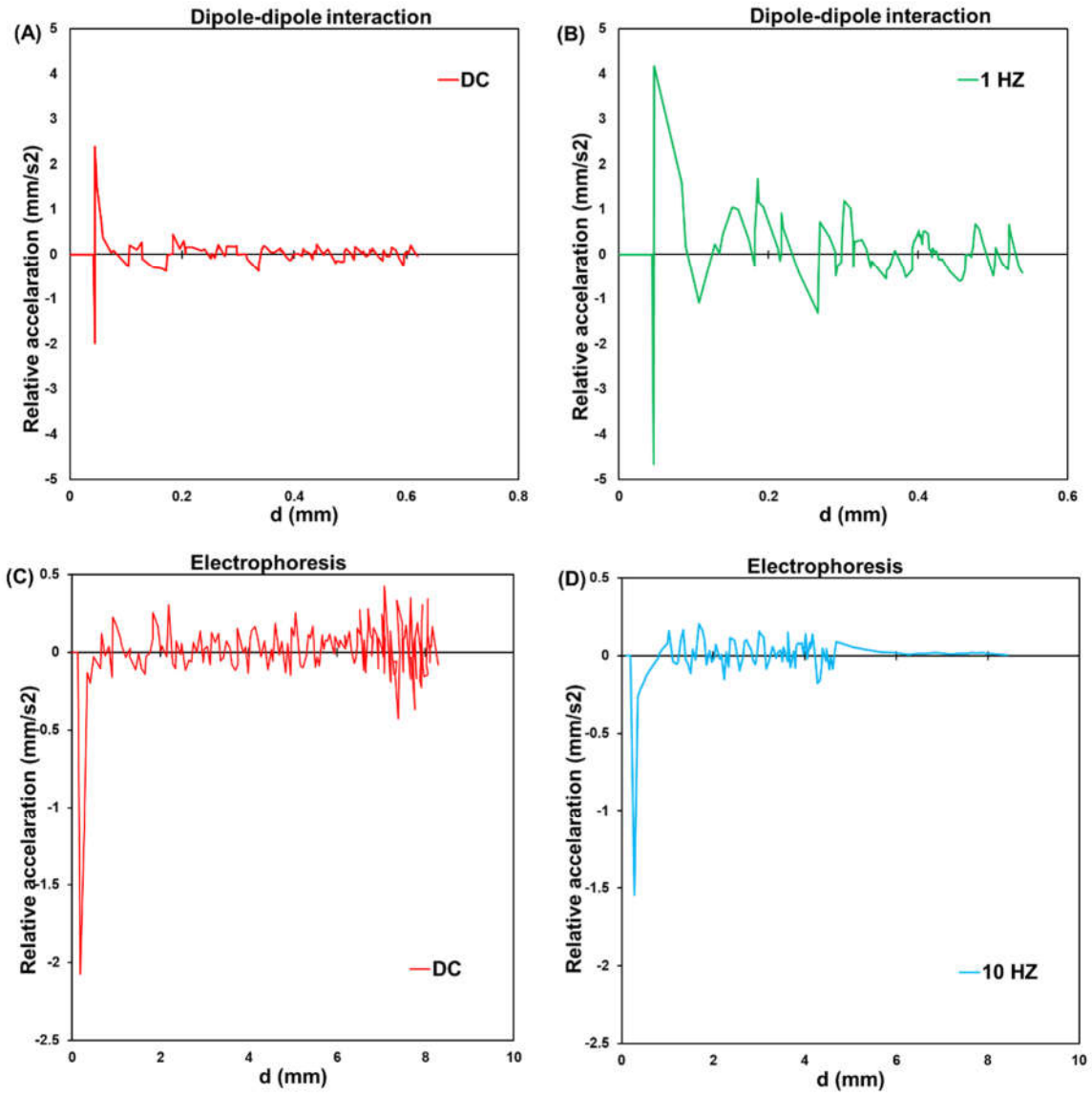

Figure 4-5 Relative acceleration of two nearby water droplets (10 µl) in 3000cst silicone oil coalescing by dipole-dipole interaction (DDI) under a pure DC electric field in **(A)** and under 1 Hz pulsed DC electric field in **(B)**. The droplets experience higher acceleration under low frequency pulsed DC electric field, leading to faster coalescence. (C) Relative acceleration of two far-away water droplets approaching each other due to electrophoresis (EP) induced by pure DC and 10 Hz pulsed DC electric field in **(C)** and **(D)**, respectively. In the case of pure DC, the relative acceleration is higher and the coalescence is faster. Comparing all cases (A) - (D) coalescence is the best by EP under pure DC electric field.

This force (DDI) increases by decreasing the distance and fluctuates as a result of resistance forces such as drag force in higher distances and film-thinning in final steps of coalescence. From **Figures** 4-4 (C) and (D), it can be seen that pure DC provides acceleration in the beginning while the pulsed DC has a significantly lower acceleration and limited response, till it passes half of the course. This behavior can be explained by the small DC component of pulsed DC in comparison to that of pure DC. The acceleration declines gradually from the beginning to about half of the distance in pure DC and starts to increase in both cases nearly from the same point. This regime suggests that most of the free charges in the water droplets have vanished and the coalescence mechanism is changed from EP to a combination of EP and DDI in the lower distances. This transient point is important during the design of a coalescer and needs to be considered in a way that water droplets can have an opportunity to transit from the EP to the DDI induced coalescence otherwise a low enhancement of coalescence efficiency will result by solely relying on the EP phenomena. Other than DDI and migratory coalescence mechanisms, it is possible to boost the motion of the water droplets in a medium under an external non-uniform electric field. The motion of the charged droplets toward the strongest pole of a non-uniform electric field due to a high dielectric constant is called dielectrophoresis (DEP) which takes place regardless of the distance of the adjacent charged droplets and defined as equation (1-18).

The DEP occurs in only one direction even if the direction of the electric field is changed, *i.e.* the only triggering component is the the gradient of electric field strength ($F \propto E^2$) not the direction in which the charges move [241, 242]. The electric field intensity in the oil

medium is different based on the angle of the needle compared to the surface of the test cell in each point. The highest intensity of the electric field occurs exactly beneath the needle electrode where θ=0° and it decreases as the angle continues to increase (see schematic in **Figure** 4-1). The distribution of the electric field could be considered similar to a cone with the apex on the sharp conductive electrode (needle). Consequently, the non-uniform distribution of the current density is experienced and could be calculated by different equations such as Warburg's correlation, equation (2-5), leading to electric field presence expressed by Ohm's law in EHD [190]. The non-uniformity of the electric fields results in weaker and stronger electric fields applied to the different regions of the continuous phase (i.e. silicone oil). This phenomenon pushes the water droplets toward the stronger regions of the electric field [189, 236, 237]. To further investigate the impact of non-uniform electric field and dielectrophoresis phenomena, the motion of a single water droplet under pure and pulsed DC electric fields were investigated (**Figure** 4-5).

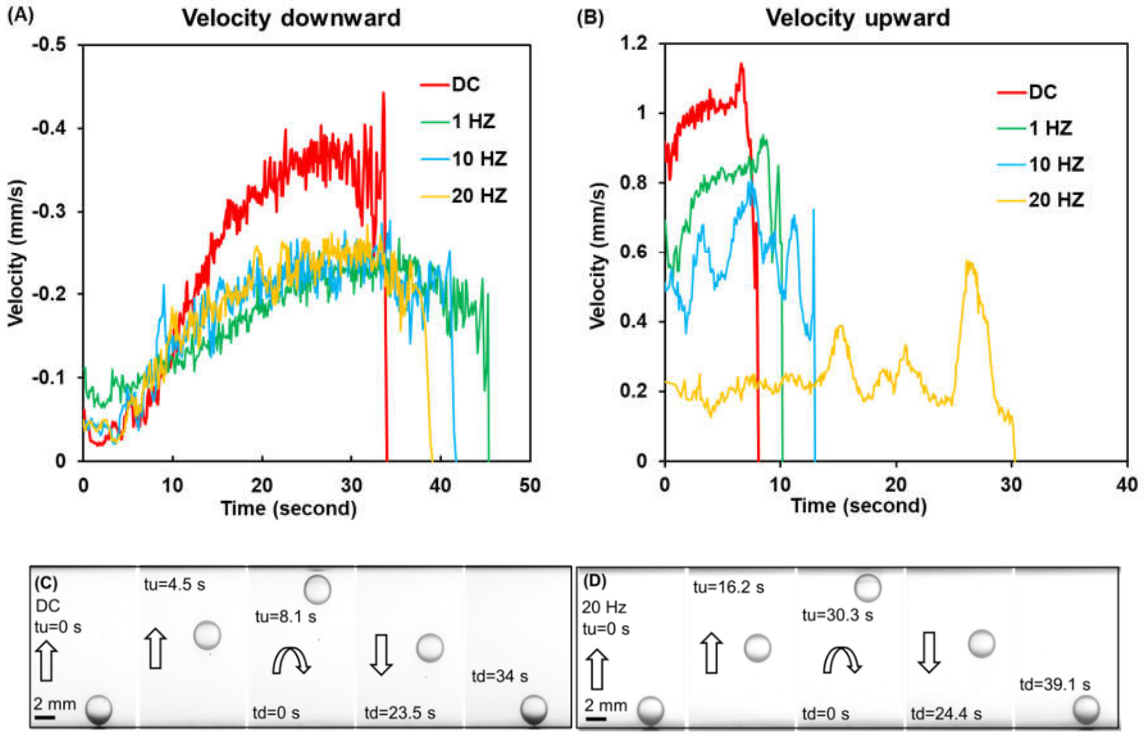

Figure 4-6 Velocity of one water droplet (10 µl) in 3000cst silicone oil vs. its traveling time between two electrodes under pure and pulsed DC (1, 10, and 20 Hz) electric fields in a downward motion in **(A)** and in an upward motion in **(B)**. It is believed that the dielectrophoresis (DEP) is responsible for the droplet motion. **(C,** and **D)** Snapshots of a droplet showing upward (t_u) and downward (t_d) traveling time between the two electrodes under a pure DC electric field and 20 Hz pulsed DC electric fields, respectively. In all cases, the EP and DEP agree in an upward direction and opposite in a downward direction. The magnitude of DEP significantly decrease by increasing the frequency results in lower.

Figure 4-5 (A) shows that the downward velocity of the droplet is not impacted by the frequency of the pulsed DC; however, switching to pure DC leads to an enhanced downward velocity. Under all applied pulsed DC voltages with various frequencies, the motion patterns of the droplets are comparable in the first 10 seconds. In the first 10 seconds of processing under pure DC, the relative velocity is less than those of the pulsed DC cases. However, after 10 seconds the velocity of the droplet under a pure DC field

increases significantly when compared to the droplet under various pulsed DC electric fields. It is speculated that this is a result of the higher electric field intensity in the areas closer to the tip of the corona needle and weaker intensity in the lower areas. This phenomenon consequently results in higher and lower DEP forces in upper and lower regions of the oil medium, respectively. Since DEP acts in the opposite direction the velocity increases by increasing the distance relative to the oil surface and eventually, electrophoresis forces overcome DEP due to the decrease in the electric field intensity in the lower areas. At some point, the droplet velocity reaches its peak and starts to decline gradually. This point is where the water droplets lose all the accumulated charges and become less active under the electric field. Similar peak and decline in the droplet velocity observed under pulsed DC electric field as well but the rate of increase and decrease of the velocity and the peak values are different. There is a tiny difference in the traveling time of the different pulsed DC treated samples which are caused by the frequency and the falling/rising potentials of the waves. The other similarity of the patterns is that in all of them, the final point has a sharp decrease in velocity (instantaneously drops to zero) which indicates the point that the water droplets touch the opposing electrode and the velocity direction start to change (half of the traveling distance, t_u=0). Due to the agreement in the direction of EP and DEP in the reverse motion (**Figure** 4-5 (B)), the pattern of the velocities is fully changed, and the velocity values are nearly three times those values observed in the downward motion. In all cases, the peak is the point where the droplets become closer to the top surface of the test cell (the surface of the silicone oil) where the intensity of the

electric field is the highest. The peak in velocity values is caused by continuously increasing DEP forces which pull the droplets toward the surface. Passing the peak point, there is a relatively sharp decline in the velocity which indicates the point where the droplets touched the top surface and released all their charges, obtained opposite charges, and started moving downward once more.

Figure 4-5 (C) and (D) represent the DEP movement sequences of two water droplets under pure and pulsed DC (20 Hz) electric fields, respectively. Under pure DC, the upward motion takes 8.1 seconds while the total transverse time in downward motion is equal to 34 seconds. The upward motion takes less time since the velocity is higher (the effect of the DEP and electrophoresis forces are in one direction); however, in a downward motion, the velocity is less since the DEP and electrophoresis are in opposite direction. This significant difference in the upward versus downward velocities takes place under the pulsed DC (1, 10, and 20 Hz) electric fields as well. However, the difference in travel time in the pulsed DC samples is not significantly higher than that of the pure DC sample. The pulsed DC samples show higher upward traveling (30 seconds in 20 Hz) time and lower downward traveling time which is the opposite of what happens under the pure DC (39 seconds in 20 Hz). By deeply considering the change in behavior, it is safe to conclude that the effect of DEP becomes weaker in the pulsed DC electric field. It is believed that this occurs due to the constant change in the potential of the electric field. Overall, understanding the movement of the charged particles helps to increase the chance of collision between the water droplets and enhance the coalescence process when multiple

droplets are present. This behavior suggests that utilizing DEP enhances the efficiency of the coalescer, especially in dilute emulsions.

In order to find the best strategy to perform a coalescence process, it is needed to first understand and define the coalescence mechanisms based on the different experimental conditions, aiming to obtain an optimized recipe. **Figure** 4-6 represents different comparisons of the upward/downward velocities of water droplets, velocities of water droplets in DDI and migratory coalescence, and the consumed power based on the frequencies of the processes. It should be noted that the 0 Hz frequency represents the case where pure DC electric fields were utilized. **Figure** 4-6 (A) shows the velocity of a single water droplet in the upward and downward directions due to the DEP forces. Forces act on single water droplet is a combination of buoyancy, gravity, drag, DEP and EP and equal to equation (4-3) and (4-4) for downward and upward motion respectively. The difference between equation (4-3) and (4-4) is approximately equal to two times of DEP (equation 4-5). The only positive value is buoyancy force which is small comparing to other forces and makes this assumption valid (ρ_{water}=1000 kg/m3 and ρ_{oil}= 967 kg/m3).

$$\boldsymbol{F_{downward} = F_{EP} - F_{DEP} - F_{Drag} + F_{gravity} - F_{Buoyancy}} \quad (4-3)$$

$$\boldsymbol{F_{upward} = F_{EP} + F_{DEP} - F_{Drag} - F_{gravity} + F_{Buoyancy}} \quad (4-4)$$

$$\boldsymbol{F_{upward} - F_{downward} = 2\,F_{DEP} - 2\,F_{gravity} + 2\,F_{Buoyancy} - F_{Drag\,up} + F_{Drag\,down} \approx 2\,F_{DEP}} \quad (4-5)$$

As indicated earlier, in the upward motion the droplet has a higher velocity but as the frequency of electric field increases, the difference between velocities in the upward and downward diminishes to the point where they become identical at a frequency of 50 Hz.

Thus, it is reasonable to design the coalescence setups in a way that the droplets mostly experience upward motions instead of a reciprocating one. Now that the direction of the motion is determined, it is better to understand and select the best fit for the type of motions. This is crucial where the water droplets need to gather in the surface of oil or the bottom of oil (higher or lower oil density compared to water density).

Figure 4-6 (B) represents the average relative velocities of two approaching droplets moving due to DDI and electrophoresis forces under the various frequency of applied electric fields. As can be seen, the average velocity of the migratory coalescence scheme (EP) is higher than that of the DDI-based coalescence. In the pulsed DC electric fields, the efficiency tends to drastically decrease after passing the frequency of 10 Hz. However, the overall efficiencies of DDI and EP between the 1 and 10 Hz are in the same order in general. It should be mentioned that in dilute emulsions (higher water droplet distances) it is more efficient to use a pure DC electric field while in highly concentrated emulsions (lower water droplet distances), the pulsed DC electric fields with the lowest possible frequency are the most efficient ones. **Figure** 4-6 (C) represents the efficiency of the coalescence processes based on the consumed power in different electric field sources (*i.e.* AC and DC).

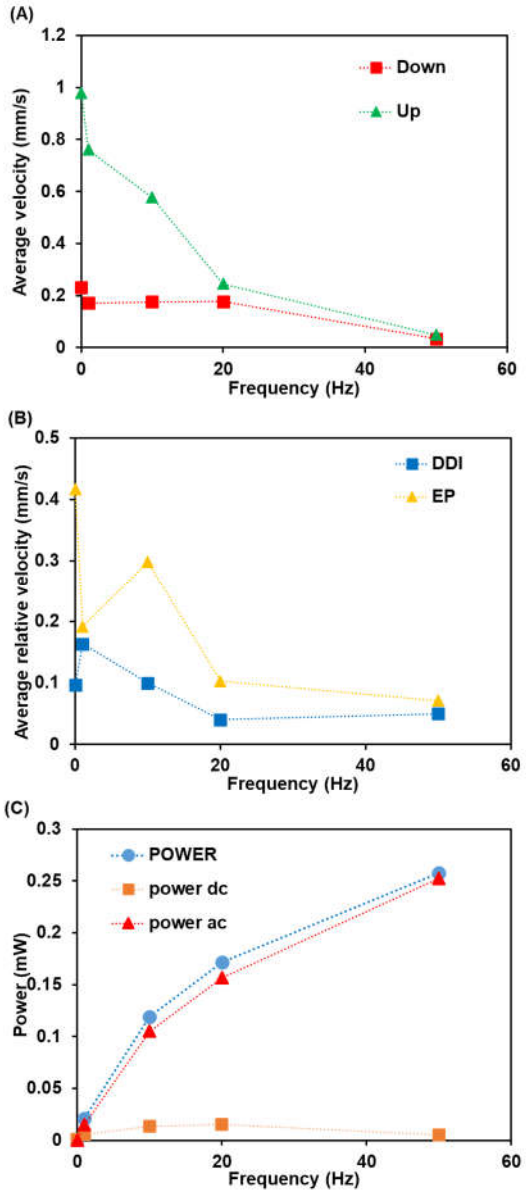

Figure 4-7 (A) The average velocity of a water droplet in 3000cst silicone oil in upward and downward motion due to the DEP forces under pure DC (0 Hz frequency) and various pulsed DC electric fields. **(B)** The average relative velocity of two approaching water droplets (10 µl) in 3000cst silicone oil under the dipole-dipole interaction (DDI) and the migratory coalescence conditions vs. the frequency of the applied electric field. **(C)** AC, DC, and total Power consumption of the pure and Pulsed DC with different frequencies.

The pulsed DC waveform is a combination of AC and DC waveforms and the power in all cases were calculated based on measuring current with multimeter in both AC and DC mode. Finally, the total power was addition of those two values (*i.e.* $P_{Total} = P_{AC} + P_{DC}$). As can be seen, the majority of the power goes to the samples treated under pulsed DC electric field with higher frequency due to an increase in the oil capacitance (higher current). Considering the effect of the frequency, it is obvious that the change in frequency from 0 Hz to higher values keeps the power consumption of the DC part constant; however for the similar frequencies, the power consumption of the AC part rapidly increases from 10 to 15, and then 25 times of pure DC at frequencies of 10, 20, and 50 Hz, respectively. To finalize this discussion, it is important to consider the type, direction, and the power consumption of the coalescence process and select the best and the most efficient coalescence scheme based on emulsion types in order to achieve the highest efficiency.

4.5 Conclusion

In the current study, a series of experiments were conducted in order to investigate the effect of DC and pulsed DC electric fields on the performance of the electrocoalescence process initiated by unipolar charge injection using corona discharge. Three main coalescence forces, DDI, EP, and DEP, were considered and investigated under different electric field types (DC and pulsed DC electric fields). All the experiments were analyzed using digital image processing techniques in order to capture the real-time values of distance between water droplets, their acceleration, and velocity in different modes of

coalescence, in addition to the power consumption of each case, were monitored and recorded. Based on the concentration of the emulsions and size of the water droplets inside the oil mediums, different regimes of electrocoalescence trigger which require different processing conditions. As a result, there is no global solution to the emulsion separation process using a corona discharge-induced charge injection. Thus, a general and optimum strategy was introduced to address different emulsions with different water concentrations and conditions.

- Pulsed DC with the lowest frequency shows better performance in DDI cases and is recommended for the emulsions with high water concentration.
- Pure DC shows the best performance in EP, beyond the other cases (pulsed DC), and is recommended for the emulsions with low water concentration.
- For emulsions with moderate water concentrations (between the highest and the lowest concentrations), the use of the pure or pulsed DC strategies is outweighed against the power consumption and processing time in order to find the optimal process conditions.
- The use of DEP forces was also investigated to address the best performance of coalescer for oil with different density particularly with oil with higher density than water.

Finally, the authors believe that this strategy can be time-varying based on dynamic emulsion conditions.

Chapter 5

5 A Top-down method of emulsion formation using corona discharge

5.1 Abstract

Forming emulsions has been a challenging task, especially for mediums with high viscosity. In conventional methods, it is needed to overcome the shear stress of the continuous phase in order to disrupt the dispersed phase droplets. Up to now, many high- and low-energy methods have been utilized in order to make emulsions. Here, a top-down method of emulsion formation is proposed using a corona discharge applicable to a wide range of emulsions (e.g., macro, nanoemulsions). The corona discharge creates an ionic wind (electroconvection) that drags water vapor droplets, created by a humidifier, into an oil medium. The corona discharge also induces the motion of the oil medium via an EHD pumping effect using a modulated bottom electrode geometry. By these two effects, this contactless method enables the immersion of the water droplets into the moving oil

medium, continuously forming a water-in-oil (W/O) emulsion. This method does not require high power and/or and an excessive amount of surfactant. The medium used in this study was silicone oil in different viscosities. The impact of oil viscosity in properties of created emulsion and the power consumption of the process is studied. This is a low-cost, contactless, and power-efficient process enabling the continuous formation of emulsions with varying oil viscosities.

5.2 Introduction

Emulsions are formed from two naturally immiscible liquids from which one is dispersed uniformly or non-uniformly into the other phase [243]. The most common emulsions in nature are water-in-oil (W/O) and oil-in-water (O/W) emulsions, which could be in different size-categories of macro, nanoemulsions in the range of 0.5-100 μm, 0.1-1 μm, and 0.01-0.1 μm, respectively [244-247]. The range of dispersity of one phase in the other one may vary based on their physical conditions and chemical compositions. However, many of the immiscible liquids could not be combined into an emulsion due to the difference in their properties (solubility of one material to the other one). In this case, there has to be a mediating agent (i.e., surfactant) in order to combine the two phases and make them stably mixed for an extended period of time [248]. In general, for emulsion formation, water, oil, energy/power, and surfactant (emulsifier compound) are needed [249]. Emulsion formation methods are investigated based on their properties and are categorized

into two general classes of high- and low-energy. Emulsions can also be classified based on other parameters, such as the chemicals used in their formation processes.

High-energy methods are referred to the emulsion formations that implement a high mechanical shear rate in the liquid medium in order to break down the large droplets of one immiscible liquid and disperse it into the other liquid homogeneously [250]. In these methods, the energy consumption is considerably high ($\approx 10^8$-10^{10} W/kg), and the droplets of the dispersed phase are relatively large (i.e., 0.1~1 μm). One limitation of these processes is that only two-phase emulsions could be formed (i.e., W/O or O/W) and it's not applicable for double emulsion [251]. The most common high-energy methods of emulsion formation are ultrasonic emulsification, high-pressure homogenization, mechanical blending (blade stirring), and microfluidics, and membrane systems [252]. However, high-pressure homogenization (HPH) and ultra-high-pressure homogenization (UHPH) are the most commonly implemented methods in commercial and industrial applications, especially in dairy industries [253]. In low-energy emulsification methods, the liquids are mixed without using mechanical forces [254]. The most common of these methods work based on the composition of the two liquid phases and the temperature at which they are treated [255]. Based on these two, low-energy emulsification methods are categorized into different distinct processes, such as emulsion inversion point (EIP), phase inversion composition (PIC), phase inversion temperature (PIT), direct emulsification inversion (DEI), and spontaneous emulsification (SE) [256]. For instance, in SE methods, an emulsion is created based on the dilution of emulsion with the disperse phase (self-emulsification). In contrary

to the high-energy emulsification methods, these methods are temperature/composition driven with significantly lower energy consumption (10^3-10^5 W/kg). However, the low-energy processes have the limitation of less flexibility in the selection of oils and working temperature and also a relatively high concentration of surfactant, which is not desirable in most applications [257].

Based on the availability of the facilities and materials, either of the low- or high-energy emulsification methods could be implemented in forming a new emulsion product. Still, in each of them, there are limitations such as chemical composition, working temperature, energy consumption, change of material properties, etc. On the other hand, most of these emulsification processes are non-continuous with a limited production rate since an external factor affects the emulsion phases (i.e., agitators, blades, chemicals, etc.).

The use of electric fields to form emulsions has been previously studied with a minimal need for surfactants and without physical/mechanical disturbance to the emulsification environment. It is hypothesized that during the electroemulsification, some charge residue remains in the emulsion, and charges which agree (either positive or negative depending on discharging polarity) are repelled each other and build-up higher zeta potential consequently form more stable emulsions [258]. With power consumption significantly less than those of the high-energy emulsification methods, electroemulsification is a reliable replacement of low- and high-energy methods (especially in high viscosity liquids) [259]. In addition, electroemulsification can enable encapsulation of liquids and formation of O/W/O or W/O/W emulsions, when compared to regular W/O and O/W emulsions that

are formed by low- and high-energy methods with less flexibility. These complex emulsions (O/W/O or W/O/W) are widely used in biomedical, drug delivery, and medicine applications [260]. Also, it has been hypothesized that electroemulsification can built-up residual charges, which consequently can increase the stability of emulsions in their shelf life [261]. But none of these methods can provide practical solutions to be implemented in real industrial applications, mainly due to difficulties of designing mechanical setups capable of addressing production line requirements. During electroemulsification, a major problem is a coalescence between like-phase droplets as a side effect of the applied electric field in the continuous phase, which is against the emulsification and is not desirable. To address this, a couple of methods have been introduced, such as using a magnetic stirrer [261] or rotary drum [262], but none can be scaled up for industrial application. In addition, problems like high dependency on dispersed phase properties, coalescence during the emulsification process, and power consumption have not been addressed.

Here, a non-uniform electric field is created using a corona discharge to form nano W/O emulsions with varying oil viscosities via a continuous and power-efficient process. A pin-to-plate (can be extended to multiple electrode and wire to plate configuration) is built for forming the non-uniform electric field via negative corona discharge. The negative corona discharge ionizes the air molecules around the pin (discharge zone), creating an ionic wind that carries water droplets (formed by a humidifier) towards a silicone oil medium. A ground electrode (plate) is placed inside the oil medium leading to oil circulation via EHD pumping. The electroconvective driven water droplets drift toward the circulating oil and

immerse into it, continuously forming a W/O emulsion. The offset of the ground electrode to the surface beneath the ionizing electrode is engineered to obtain the desired motion of the continuous phase (i.e., silicone oil) for efficient emulsion formation. The charged water droplets vary in sizes (from nano to macro) based on the type of utilized humidifier, leading to the formation of nano to macro W/O emulsions. This study paves the path for developing a contactless, continuous, and power-efficient method for the production of W/O emulsions applicable in the cosmetic, drug delivery, and food industry.

5.3 Materials and methods

Figure 5-1A shows the schematic of the electroemulsification method induced by the corona discharge. Setup includes a sharp tip/wire (pin), narrow channel, ground electrode (plate), and continuous phase fluid (i.e., silicone oil). The ground electrode is installed at the bottom of the container with an adjustable position. This offset can create horizontal movement on the oil as an effect of the collision between ions (created by the sharp electrode) and the oil surface, so-called EHD pumping. In order to investigate the EHD pumping in a laboratory environment and to eliminate the effect of other mechanical variables, a circular shape closed-loop setup is designed to conduct the experiments (**Figure** 5-1B). A high-voltage generating system is tied to a super fine tungsten needle as a corona-generating electrode. A DSLR camera (Nikon D5500) was remotely operated to take a video of the top view of the liquid surface during the tests. Voltages and currents were actively monitored and recorded using the built-in measurement system of the TREK

amplifier coupled to a Keithley 2100 digital multimeter. The high-voltage system utilizes a ± 10 kV TREK Model 10/10B high-voltage amplifier connected to a bench-top function generator (SDG 1032X) that was capable of providing different waveforms and frequencies. Still, only negative voltages were used for the results presented in this work. Different materials used in these experiments were mainly deionized water (Sigma-Aldrich) and silicone oil with different viscosities (Hudy). The setup is filled up to h=10 mm silicone oil with a viscosity of 100, 200, and 350 cst. With the help of a laboratory jack, the gap between the corona generating electrode (sharp tungsten needle) and the top surface of the oil in the pump was kept constant to a specific distance. The optimum distance can be calculated by considering the current density distribution on the oil surface, which is defined by Warburg's law (Equation 2-5).

The current density distribution in a point on the surface reaches zero when the angle between the point and the needle axis reaches 65˚[131]. As a results of this distribution the corona emitting electrode must be placed in a distance d away from the oil, and is offset from the ground electrode by a length L, where L is at least equal to or greater than 2.15*d(tan(65°)*d). The pump has consisted of two concentrically attached glass Petri dishes with outside diameters (OD) of 60 and 90 mm. With this configuration, a circular channel formed with a width of 25 mm. In order to cover the whole width of the channel with the ionic wind, the distance of the needle tip to the oil surface was set to d=6 mm. In addition, the ground electrode needs to be out of this area to make sure that no vertical impact takes place by the ionized water droplets. In this way, all the water droplets have

velocity in the oil surface direction. This configuration prevents charge trapping by vertical charge injection as well as a lack of momentum by horizontal charge injection. Due to these considerations, the ground electrode was kept as l=12 mm.

Another thing that needs to be considered is the applied voltage to the EHD pumping setup. If the applied voltage is lower than that of corona onset voltage, there is no discharge occurring during the process. According to Townsend's discharge regime, the current is proportional to the square of the applied voltage [142], and the corona onset voltage can be found from the experimental results (equation 1-3).

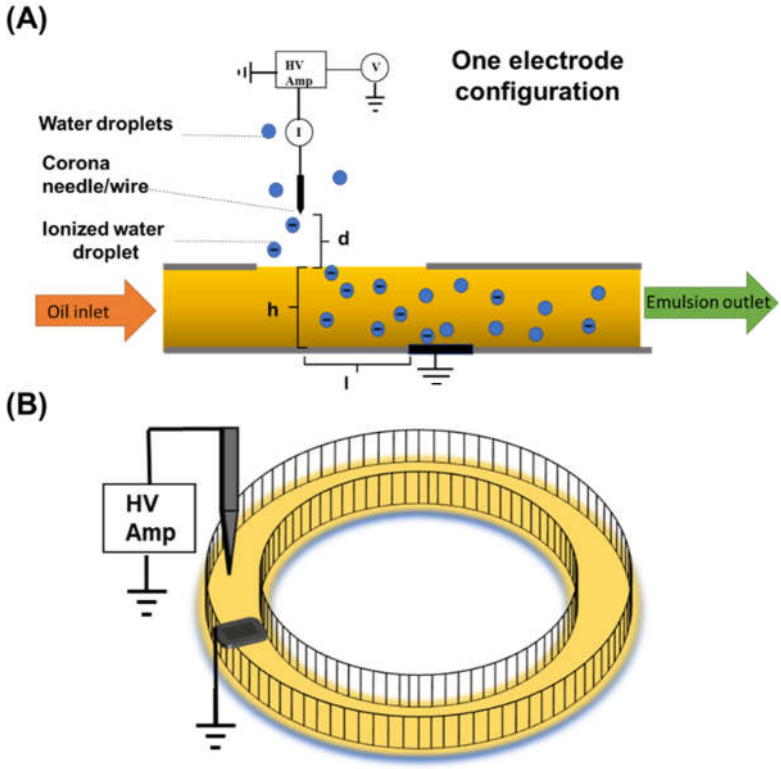

Figure 5-1 A cross-section schematic of the setup for W/O emulsion formation in (A) air near the sharp needle/wire is ionized due to the high gradient of the electric field. These ions drift toward the ground electrode forming an ionic wind that caries water droplets

(formed by a humidifier) towards the oil medium via electroconvection. The charged water droplets immerse into the silicone oil that is drifted/pumped by the corona discharge (EHD pumping) via modulating the configuration of the ground electrode. The combination of both effects induced by the corona discharge leads to dispersion of the medium phase (silicone oil) embedding water droplets inside and results in the formation of W/O emulsion. (B) 3D view of the circular setup cross-section of which is shown in (A).

Figure 5-2 shows negative corona discharge with different electrode configurations (changed t values from 10 to 25 mm). In all cases, the corona onset voltage was found to be 3 kV. In general, the higher applied voltage corresponds to a higher current and stronger discharge regime. The most applicable way to control the pump discharge flow rate is to manipulate applied voltage. The electric wind velocity in corona discharge can be calculated by [263]:

$$v = M\sqrt{\frac{R.I}{\mu}} \qquad (5-1)$$

Where R is the distance between the electrodes, μ is the ion mobility, and M is a constant. According to this equation, the higher current is correlated to the higher velocity of the impacting water droplets and higher pump performance. However, a higher current increase number of ions in the space charge and built-up trapped charge on the oil surface and consequently increase the electrostatic pressure causing a cone formation, which results in a vortex flow between the needle and the ground electrode. This phenomenon is deeply investigated by authors in other work [186]. Based on the limitations of the high and low voltages in the processing and by applying ramp waveform from 0 to 8.5 kV, an optimum operating voltage was experimentally found to be precisely 6.5 kV. However, this voltage might differ based on different setup geometry and oil level and properties.

In order to control the processing parameters (i.e., relative humidity, needle distance to the oil surface, imaging, etc.), a customized chamber with a controlled atmosphere was utilized. The moisture was provided by a typical home humidifier, and the relative humidity was kept continuously at 87-90%, during the whole experiments. Also, in order to prevent the accumulation and excessive condensation of tiny water droplets, the complete emulsion formation setup was kept at 100 mm from the bottom of the chamber and out of the direct flow of the humidifier.

The emulsion samples were made by applying voltage for 5 minutes for each batch with different silicone oil viscosities of 100, 200, and 350 cst and 100 mM Span 80 as the surfactant. The processed samples were weighted and then collected into separate quartz

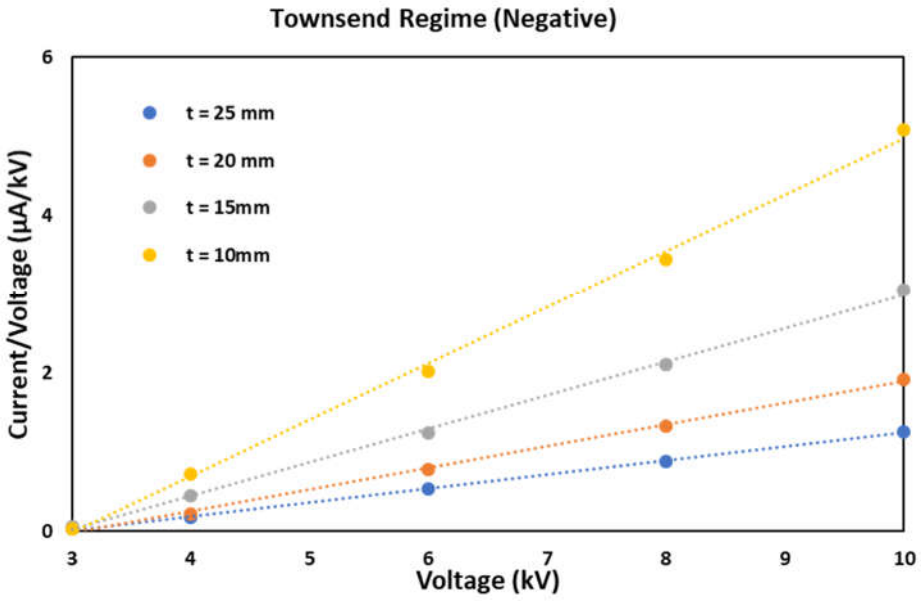

Figure 5-2 Shows negative corona discharge characterization on the pin-to-plate (needle-to-ground electrode) configuration. The corona onset voltage was found to be 3kV in all corona gaps (*t*, the distance between the pin and the plate). In all cases, the relationship

between the voltage and the current/voltage datapoints is linear, which verifies Townsend's regime characteristics of the corona discharge.

cuvettes (10×10×45 mm) for characterization purposes. The prepared batches were then analyzed under an automated optical microscope for measuring the droplet sizes and their distribution (Keyence VHX-600 digital microscope, Magnification of 20-2000 x). Finally, using the MIPAR software package [264], a proper recipe was prepared for calculating the number and the size of the droplets from the captured images. The water droplets size created by the humidifier was measured by a Phase Doppler Anemometer capable of measuring droplets ranging from 0.3 to 10 μm. The results of image processing and the experimental observations were in strong accordance.

5.4 Result and discussion

In the ion-drag pump, EHD force is produced by the interaction of electrical fields and free charges in a fluid insulating medium. Pumping is achieved if the electrical shear stresses are higher than the viscous shear stress. Therefore, EHD pumping is a phenomenon that has two basic requirements. First, the dielectric fluid being pumped must contain free charges. Second, an electric field must be present to interact with the free charges in the fluid. Free charges are established in the fluid medium by direct injection from a corona source [44]. An electric field is formed between the sharp tip (pin) and the ground electrode (plate). This electric field drags the free charges through the area, thus setting the fluid in motion. These EHD pumps are known as ion-drag pumps. In general, The EHD ion drag

pumping depended on the electrical current, the applied voltage, and the geometry of the electrode. The flow of this EHD pumping can be manipulated by either power supply voltage or distance between the beneath of the ionizing electrode to the closest side of the ground electrode. In the corona discharge fields of the pumping section, it was expected that ionic wind as gas-phase EHD flow was blown along with the gas-liquid interface from the emitter electrode toward the collector electrode. It seemed that the ionic wind improved the liquid pumping due to an interfacial momentum transfer effect along with the gas-liquid interface [45]

The prepared emulsion samples were collected separately into different quartz cuvettes in order to do optical microscopy for observing the water droplet sizes in the emulsions. In all the samples, under different magnifications, a significant number of water droplets were found, which the quantity of them is in agreement with the weighted samples ~2 wt.% of added water content (**Figure** 5-3A). In addition to this, the size distribution of the water droplets under higher magnification (**Figure** 5-3B) shows significantly smaller droplets that were not apparent under an optical microscope. It was hypothesized that the droplet size distribution in the droplet is the same as the size distribution of the water droplets made by the humidifier. The size distribution and water droplet uniformity in all samples with different oil viscosities are nearly similar, which proves that the process is independent of the oil viscosity. **Figures** 5-3A and B clearly show that the emulsion samples were made successfully, considering the stable water droplets inside the oil medium. Regardless of the

oil viscosity, the emulsion samples show the obvious presence of the water droplets in different sizes.

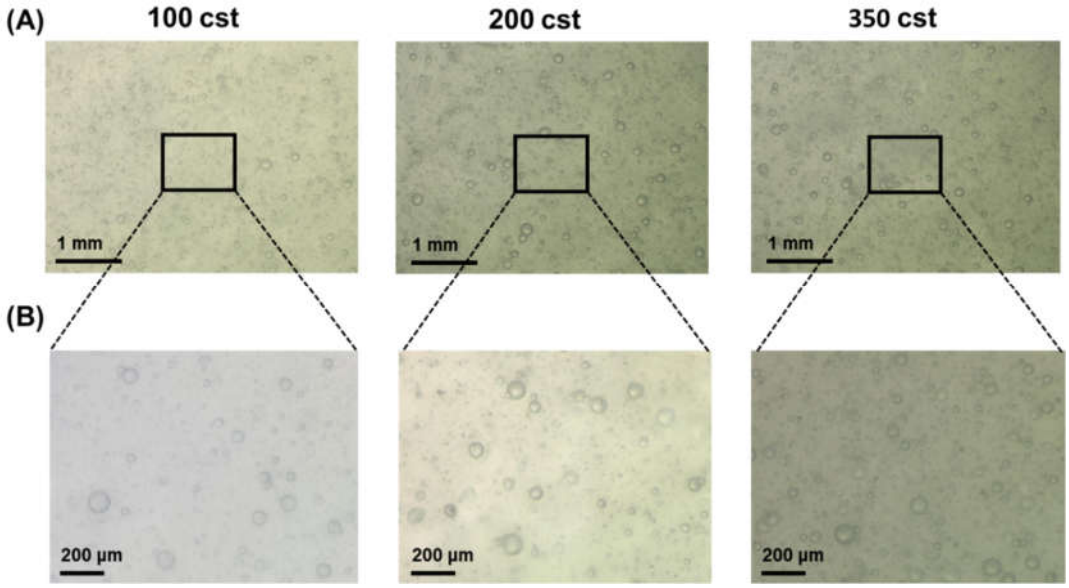

Figure 5-3 Microscopy images of the W/O emulsions formed using the corona discharge with varying oil viscosity. (A), clearly showing the water droplets inside the silicone oil continuous phase. Distribution and size of the water droplets are comparable, regardless of different viscosity oils (B) Shows higher magnification microscopy images shown in (A).

This proves that the processing recipe could be applied to different mediums with different viscosities. On the other hand, the distribution of the droplets throughout the imaging areas of all samples shows that the water droplets existed uniformly in different locations. This finding justifies that the pumping process is efficient since the samples were collected from different levels of oil from different regions of the pump surface. It worth mentioning that the reason for slightly higher water content in the lower oil viscosity reflects the fact that the pumping process was more easily done for the silicone oil 100 cst due to higher electroconvection flow. As can be seen from the size distribution graphs (**Figure** 5-4), all

the samples have a relatively similar trend in the size distribution of the water droplet size inside the emulsions. However, by increasing the viscosity of the silicone oil to 350 cst, it seems that the size of the water droplets slightly increased. The most probable reason for this behavior is that in this viscosity, a coalescence happens around the ground electrode due to lower electroconvection motion, and water droplets have enough time to get closer and coalesce. This suggests that the geometry of the ground electrode needs to be optimized based on the liquid properties, processing conditions, and the electric field applied to the medium to reduce the coalescence rate.

Figure 5-5 shows the current consumed by EHD pump as the response to ramp input (0~8.5 kV) with different oil viscosities under the same processing conditions (i.e., processing time, applied voltage, needle distance to the oil surface, etc.). As can be seen, the highest current consumption goes to the sample with the highest viscosity. The reason is that higher viscosities correspond to the lower ion mobility which is the same as lower electroconvection flow and subsequently, fewer charge carriers can pass the distance between electrodes and trapped on the oil surface. The trapped charge built electrostatic pressure and deformed the surface, causing lower oil thickness on the area close to the ground electrode. This phenomenon creates a short passage with lower electrical resistance resulting in a significant portion of charges transferred through conduction rather than electroconvection.

Figure 5-6A shows surface deformation of different oil viscosity at 6.5 kV applied voltage. In the highest applied voltage (8.5 kV) and higher viscosity, the charges can penetrate the

surface, open a direct path to the ground electrode (**Figure** 5-6B). The effect of decreasing resistance directly reflected the number of transferred charges and the consumed current, which is in direct relation with the consumed power.

Table 5-1 shows the power consumed during the process with different oil viscosity. In the next step, the corresponding power density of each sample with different viscosity is calculated. In order to do so, the prepared emulsions were weighed after processing and Compared to the reference weight of each 10-g batch before processing. The additional weight to the oil medium shows the final mass of each sample. By dividing the weight of each batch after the emulsification process, the current density is found. As can be seen from **Table** 5-1, the highest power density is found to be for the sample with the highest viscosity (358 mW/kg). Apparently, the power density calculated for these samples is significantly lower than that of the emulsions formed via other methods such as high-energy (10^8~10^{10} W/kg) and low-energy (10^3~10^5 W/kg) emulsification methods even by considering the power of the external source of humidity (According to Department of Energy report the average power of portable cool mist generator is 85 Watt [265]).

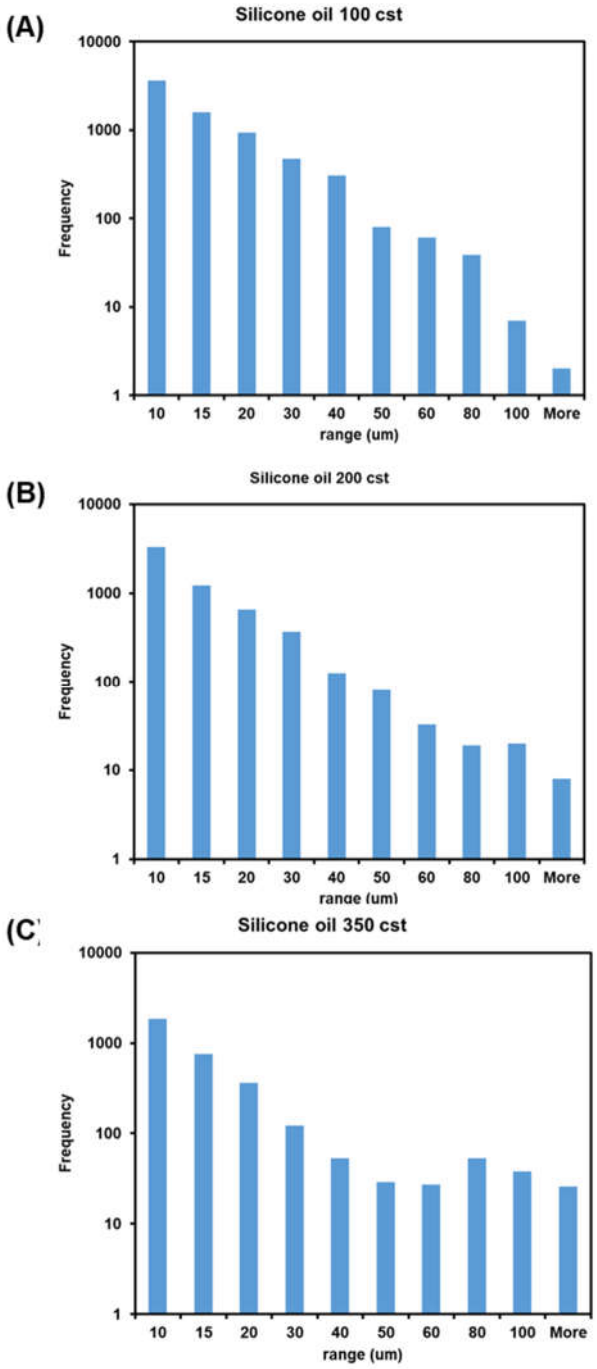

Figure 5-4 Size and distribution of the water droplets inside the silicone oil with a viscosity of 100 cst (A), 200 cst (B), and 350 cst (C). Regardless of oil viscosity, the distribution

number of the water droplets significantly decreases by an increase in the droplet sizes, which is in accord with the measured sizes of the water droplets formed by the humidifier. This indicates successful immersion of water droplets, without major coalescence, inside various silicone oil mediums.

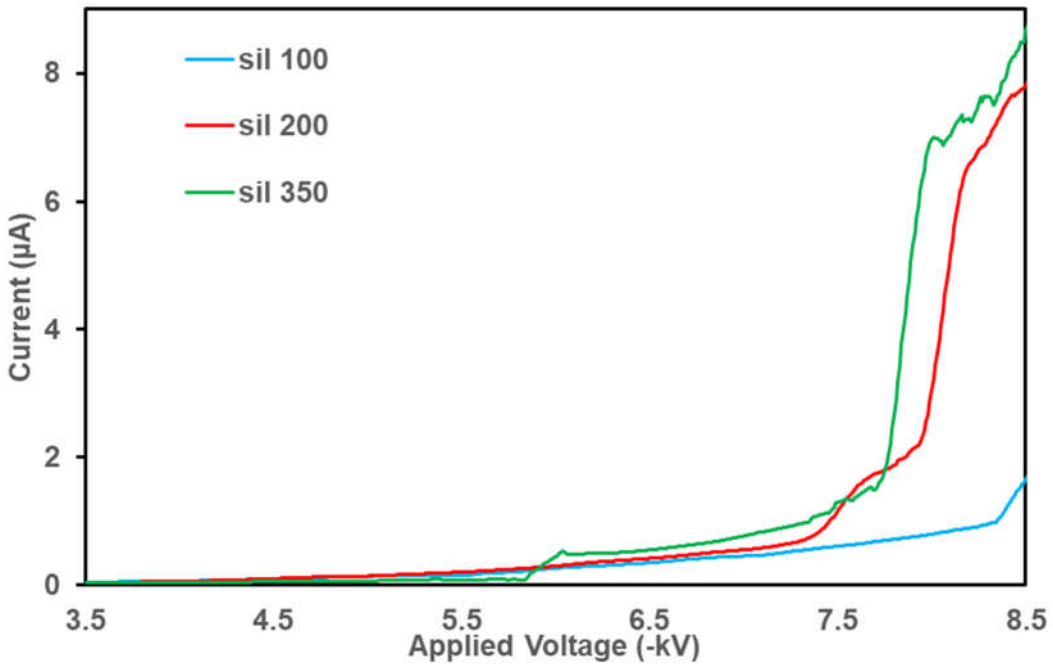

Figure 5-5 Plot of current versus the applied voltage to the tip of the corona generating needle (pin). Regardless of silicone oil viscosity, the measured current is minimal and following the same trend when the applied voltage is below 7kV (absolute value). After this voltage, higher viscosity oil undergoes a considerable surface deformation opening a clear path for ions created by the needle (pin) to reach the ground electrode (plate) directly. As a result, the sharp peaks of the immediate increase in the current can be seen for oils with viscosities of 200 cst and 350 cst, when compared to the low viscous silicone oil (100 cst).

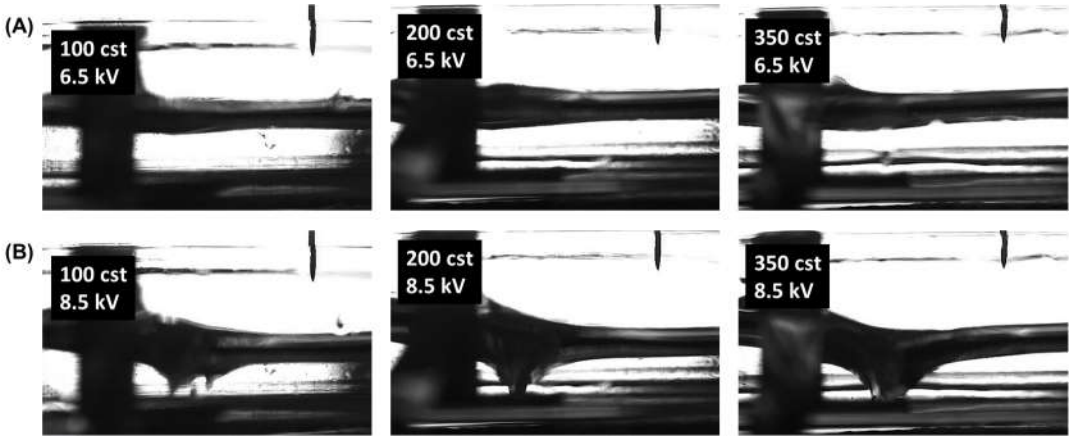

Figure 5-6 Shows cross-section images of the silicone oil deformation under the corona discharge. In (A), by increasing the oil viscosity, a slight increase in the surface deformation of the oil is observed, which results to lower electrical resistance between the needle or oil surface and the ground electrode (at the bottom of the oil) and the higher current passing through the oil. (B) Shows oil deformation (cone formation) by an increase in the applied electric field. The observed deformation is enhanced for the oil with the highest viscosity (350 cst). The cone formation results in a back-vortex flow, which is not favorable for the emulsion formation using the corona discharge. For emulsion formation, applied voltage and other parameters need to be adjusted for a given oil to avoid its deformation.

Table 5-1 Power consumption for emulsion formation using silicone oil with different viscosities.

Oil vicosity (cst)	100	200	350
Power (mW)	2.3	2.7	3.6
Power density (mW/Kg)	229.2	273.6	358.5

5.5 Conclusion

The proposed emulsion formation method is a top-down approach for preparing emulsions with controllable water content. Despite all the conventionally available emulsion formation methods, the droplets are first made externally regardless of the limitation

introduced by the continuous phase (overcoming the shear stress or chemical composition). In the next step, the droplets have impinged into the oil medium via acquired acceleration and velocity from electrical charging. Simultaneously, the discharged ions create a pumping feature inside the continuous phase, which provides continuous emulsion formation. Continuous emulsion formation makes it possible to have real-time control of the emulsion formation process. In addition, the proposed method eliminates the adverse effects of external pressure and temperature existing in commercially available processes on sensitive applications. At the same time, the use of any type of moving parts is eliminated as well, which results in a cleaner product without introducing erosion byproduct to the final product. Furthermore, it is hypothesized that some charge residue remains in the emulsion, which potentially can increase the stability of the emulsion and, consequently, less needed concentration of emulsifier agents. Finally, the energy consumption of this process is significantly less than other widely used methods of emulsion formation. Combined with its scalability and low initial cost and life cycle cost, this method could be a viable alternative to the other emulsion formation process in different industrial sectors. **Table** 5-2 shows a comparison between this method and commercially available method (low and high energy).

Table 5-2 A comparison between low energy, high energy, and proposed electroemulsification methods.

Methods	Power density	Viscosity dependency	Surfactant concentration	Equipment cost	Continous/batch	Scalibility	Stability	Controlled enviroment	Increasing temperature/pressure
Low Energy	10^3~10^5 W/kg	High	High	Low	Batch	Low	High	Yes	No
High Energy	10^8~10^{10} W/kg	High	Moderate	High	Batch	Moderate	Moderate	No	Yes
Electroemulsification	<100 W/kg	Low	Low	Low	Continious	High	Moderate	No	No

Chapter 6

6 Future work

6.1 A potential application of the corona discharge in medical diagnosis

The need for the fast diagnosis of illnesses in the early stage is going to become essential to taking actions against curing and potentially obtaining higher chances of success and detecting a cause for the disease such as cancers, viruses, bacteria, a fungal, autoimmune disorder, interruption of the balance in human bodies playing crucial roles in selecting standard treatment care of the patient which usually takes time and needs special and expensive equipment. In addition, conducting those tests need well-trained clinical personnel to perform procedures, which typically it is not available in small cities or villages. Furthermore, this process can increase the risk of false-negative results. Recently, the application of dielectrophoresis (DEP) and electrophoresis (EP), which have been widely used in microfluidics, biosensors, environmental studies, have shown promising

results to distinguish between healthy and infected (unhealthy) cells in a fast and accurate way.

The motion of matter due to the polarization effect in a non-uniform electric field is called DEP, and due to this effect, issues in medical science can be identified according to their polarization properties. This effect has shown exciting results in several applications, including eukaryotic and prokaryotic cells, oncology, stem cells, drug delivery, virus, bacteria, microorganism, fungi, DNA, proteins, and enzymes.

Also, the charged particle such as backbone phosphate in DNA will move when they are exposed to an electric field (either uniform or non-uniform) due to electrophoresis effect. If they are dispersed into a special gel, they can show the unique DNA fingerprint. Also, EP is widely used to detect some diseases such as Thyroid problems, Diabetes, Anemia, Liver diseases.

DEP and EP have been demonstrated to have the ability to be accurate and cost and time effective diagnostic techniques in comparison to the conventional methods. However, they have several challenges such as darkening of the electrode, the effect of high gradients acting on electrodes, increasing fluid temperature, evaporation of water or liquid, and consequence variations in concentrations and osmolarity which need to be considered.

Corona discharge is a contactless method to generate a non-uniform electric field inside of the fluid with lower power and consistent intensity. This method can be an excellent alternative for the current approach and overcome those challenges.

References

1. Melcher, J. and G. Taylor, *Electrohydrodynamics: a review of the role of interfacial shear stresses.* Annual review of fluid mechanics, 1969. **1**(1): p. 111-146.
2. Saville, D., *Electrohydrodynamics: the Taylor-Melcher leaky dielectric model.* Annual review of fluid mechanics, 1997. **29**(1): p. 27-64.
3. Peek, F.W., *Dielectric phenomena in high voltage engineering*. 1920: McGraw-Hill Book Company, Incorporated.
4. Chapman, J.R. and J.R. Chapman, *Practical organic mass spectrometry: a guide for chemical and biochemical analysis*. 1995: John Wiley & Sons.
5. Zhang, J., K. Adamiak, and G. Castle, *Numerical modeling of negative-corona discharge in oxygen under different pressures.* Journal of Electrostatics, 2007. **65**(3): p. 174-181.
6. Pignolet, P., et al., *Ozone generation by point to plane corona discharge.* Journal of Physics D: Applied Physics, 1990. **23**(8): p. 1069.
7. Locke, B., et al., *Electrohydraulic discharge and nonthermal plasma for water treatment.* Industrial & engineering chemistry research, 2006. **45**(3): p. 882-905.
8. Chang, J.-S., A.J. Kelly, and J.M. Crowley, *Handbook of electrostatic processes*. 1995: CRC Press.
9. Doshi, J. and D.H. Reneker, *Electrospinning process and applications of electrospun fibers.* Journal of electrostatics, 1995. **35**(2-3): p. 151-160.
10. Inculet, I.I., Y. Murata, and G.P. Castle, *A new electrostatic separator and sizer for small particles.* IEEE Transactions on Industry Applications, 1983(3): p. 318-323.
11. Yabe, A., Y. Mori, and K. Hijikata, *EHD study of the corona wind between wire and plate electrodes.* AIAA journal, 1978. **16**(4): p. 340-345.
12. Jones, T., *Electrohydrodynamically enhanced heat transfer in liquids—a review*, in *Advances in heat transfer*. 1979, Elsevier. p. 107-148.
13. Robinson, M., *Convective heat transfer at the surface of a corona electrode.* International Journal of Heat and Mass Transfer, 1970. **13**(2): p. 263-274.
14. Yamaga, J. and M. Jido, *Cooling method by use of corona discharge*. 1976, Google Patents.
15. Carlon, H. and J. Latham, *Enhanced drying rates of wetted materials in electric fields.* Journal of Atmospheric and Terrestrial Physics, 1992. **54**(2): p. 117-118.
16. Wolny, A., *Intensification of the evaporation process by electric field.* Chemical Engineering Science, 1992. **47**(3): p. 551-554.
17. Wolny, A. and R. Kaniuk, *The effect of electric field on heat and mass transfer.* Drying technology, 1996. **14**(2): p. 195-216.
18. Barthakur, N. and N. Arnold, *Evaporation rate enhancement of water with air ions from a corona discharge.* International Journal of Biometeorology, 1995. **39**(1): p. 29-33.

19. Go, D.B., et al., *Ionic winds for locally enhanced cooling.* Journal of Applied Physics, 2007. **102**(5): p. 053302.
20. Nelson, D., et al., *Corona discharge effects on heat transfer and pressure drop in tube flows.* Journal of Enhanced Heat Transfer, 2000. **7**(2).
21. Seyed-Yagoobi, J., *Electrohydrodynamic pumping of dielectric liquids.* Journal of Electrostatics, 2005. **63**(6-10): p. 861-869.
22. Lai, F. and K.-W. Lai, *EHD-enhanced drying with wire electrode.* Drying technology, 2002. **20**(7): p. 1393-1405.
23. Davidson, J., F. Kulacki, and P. Dunn, *Convective heat transfer with electric and magnetic fields.* Handbook of Single-Phase Convective Heat Transfer, 1987: p. 9.1-9.48.
24. Vinogradov, J., et al., *Voltage-current characteristics of a flame-assisted unipolar corona.* Combustion and flame, 2001. **127**(1-2): p. 2041-2050.
25. Ohisa, H., I. Kimura, and H. Horisawa, *Control of soot emission of a turbulent diffusion flame by DC or AC corona discharges.* Combustion and Flame, 1999. **116**(4): p. 653-661.
26. Won, S., et al., *Effect of electric fields on reattachment and propagation speed of tribrachial flames in laminar coflow jets.* Proceedings of the Combustion Institute, 2007. **31**(1): p. 963-970.
27. Dion, M., C. Martoff, and M. Hosack, *On the mechanism of Townsend avalanche for negative molecular ions.* Astroparticle Physics, 2010. **33**(4): p. 216-220.
28. Aliat, A., et al., *Implementation of Fuchs' model of ion diffusion charging of nanoparticles considering the electron contribution in dc-corona chargers in high charge densities.* Journal of Physics D: Applied Physics, 2009. **42**(12): p. 125206.
29. Castle, G.P., I.I. Inculet, and K.I. Burgess, *Ozone generation in positive corona electrostatic precipitators.* IEEE Transactions on Industry and General Applications, 1969(4): p. 489-496.
30. Dau, V.T., et al., *Corona based air-flow using parallel discharge electrodes.* Experimental Thermal and Fluid Science, 2016. **79**: p. 52-56.
31. Liu, M., et al. *Development processes of positive and negative DC corona under needle-plate electrode in air*. in *2016 IEEE International Conference on High Voltage Engineering and Application (ICHVE)*. 2016. IEEE.
32. Lu, B. and H. Sun, *The role of photoionization in negative corona discharge.* AIP Advances, 2016. **6**(9): p. 095111.
33. He, B., et al., *Study on law of negative corona discharge in microparticle-air two-phase flow media.* Aip Advances, 2016. **6**(3): p. 035114.
34. Jadidian, J., et al., *Effects of impulse voltage polarity, peak amplitude, and rise time on streamers initiated from a needle electrode in transformer oil.* IEEE Transactions on Plasma Science, 2012. **40**(3): p. 909-918.
35. Fylladitakis, E.D., M.P. Theodoridis, and A.X. Moronis, *Review on the history, research, and applications of electrohydrodynamics.* IEEE Transactions on Plasma Science, 2014. **42**(2): p. 358-375.
36. Robinson, M., *A history of the electric wind.* American Journal of Physics, 1962. **30**(5): p. 366-372.

37. Tsouris, C., W.T. Shin, and S. Yiacoumi, *Pumping, spraying, and mixing of fluids by electric fields.* The Canadian Journal of Chemical Engineering, 1998. **76**(3): p. 589-599.
38. Darabi, J., M. Ohadi, and D. DeVoe, *An electrohydrodynamic polarization micropump for electronic cooling.* Journal of Microelectromechanical Systems, 2001. **10**(1): p. 98-106.
39. Darabi, J. and M.M. Ohadi, *Electrohydrodynamicly enhanced micro cooling system for integrated circuits*. 2002, Google Patents.
40. Lee, C., A. Robinson, and C. Ching. *Development of EHD ion-drag micropump for microscale electronics cooling*. in *2007 13th International Workshop on Thermal Investigation of ICs and Systems (THERMINIC)*. 2007. IEEE.
41. Melcher, J.R., *Continuum electromechanics*. Vol. 2. 1981: MIT press Cambridge.
42. Stuetzer, O.M., *Ion drag pressure generation.* Journal of Applied physics, 1959. **30**(7): p. 984-994.
43. Pickard, W.F., *Ion drag pumping. I. Theory.* Journal of Applied Physics, 1963. **34**(2): p. 246-250.
44. Bryan, J.E. and J. Seyed-Yagoobi, *An experimental investigation of ion-drag pump in a vertical and axisymmetric configuration.* IEEE Transactions on Industry Applications, 1992. **28**(2): p. 310-316.
45. Sharbaugh, A.H. and G.W. Walker, *The design and evaluation of an ion-drag dielectric pump to enhance cooling in a small oil-filled transformer.* IEEE Transactions on Industry Applications, 1985(4): p. 950-955.
46. Benetis, V., *Experimental and computational investigation of planar ion drag micropump geometrical design parameters*. 2005.
47. Yang, L.-J., J.-M. Wang, and Y.-L. Huang. *The micro ion drag pump using indium-tin-oxide (ITO) electrodes*. in *The Sixteenth Annual International Conference on Micro Electro Mechanical Systems, 2003. MEMS-03 Kyoto. IEEE*. 2003. IEEE.
48. McClements, D.J., *Food emulsions: principles, practices, and techniques*. 2015: CRC press.
49. Chiou, Y.-C., et al., *Direct Measurement of the Magnitude of the van der Waals Interaction of Single and Multilayer Graphene.* Langmuir, 2018. **34**(41): p. 12335-12343.
50. Ambrosetti, A., et al., *Wavelike charge density fluctuations and van der Waals interactions at the nanoscale.* Science, 2016. **351**(6278): p. 1171-1176.
51. Lim, J., et al., *A review on the effects of emulsions on flow behaviours and common factors affecting the stability of emulsions.* Journal of Applied Sciences, 2015. **15**(2): p. 167-172.
52. Khan, B.A., et al., *Basics of pharmaceutical emulsions: A review.* African Journal of Pharmacy and Pharmacology, 2011. **5**(25): p. 2715-2725.
53. Aditya, N., et al., *Co-delivery of hydrophobic curcumin and hydrophilic catechin by a water-in-oil-in-water double emulsion.* Food chemistry, 2015. **173**: p. 7-13.
54. Laba, D., *Rheological properties of cosmetics and toiletries*. 2017: Routledge.
55. Janssen, P., C. Noïk, and C. Dalmazzone. *Emulsion formation in a model choke-valve*. in *SPE Annual Technical Conference and Exhibition*. 2001. Society of Petroleum Engineers.
56. Posocco, P., et al., *Interfacial tension of oil/water emulsions with mixed non-ionic surfactants: comparison between experiments and molecular simulations.* RSC Advances, 2016. **6**(6): p. 4723-4729.

57. Winsor, P., *Hydrotropy, solubilisation and related emulsification processes.* Transactions of the Faraday Society, 1948. **44**: p. 376-398.
58. Ozturk, B. and D.J. McClements, *Progress in natural emulsifiers for utilization in food emulsions.* Current Opinion in Food Science, 2016. **7**: p. 1-6.
59. Kilpatrick, P.K., *Water-in-crude oil emulsion stabilization: review and unanswered questions.* Energy & Fuels, 2012. **26**(7): p. 4017-4026.
60. Ganley, W.J., P.T. Ryan, and J.S. van Duijneveldt, *Stabilisation of water-in-water emulsions by montmorillonite platelets.* Journal of colloid and interface science, 2017. **505**: p. 139-147.
61. Urbina-Villalba, G. and M. García-Sucre, *Brownian dynamics simulation of emulsion stability.* Langmuir, 2000. **16**(21): p. 7975-7985.
62. Salager, J.-L., *Surfactants types and uses.* FIRP booklet, 2002. **300**.
63. Kokal, S.L., *Crude oil emulsions: A state-of-the-art review.* SPE Production & facilities, 2005. **20**(01): p. 5-13.
64. Sztukowski, D.M. and H.W. Yarranton, *Oilfield solids and water-in-oil emulsion stability.* Journal of colloid and interface science, 2005. **285**(2): p. 821-833.
65. Đorđević, S.M., et al., *Parenteral nanoemulsions as promising carriers for brain delivery of risperidone: Design, characterization and in vivo pharmacokinetic evaluation.* International journal of pharmaceutics, 2015. **493**(1-2): p. 40-54.
66. Lyklema, J., *Fundamentals of interface and colloid science: soft colloids*. Vol. 5. 2005: Elsevier.
67. Sjöblom, J., et al., *Our current understanding of water-in-crude oil emulsions.: Recent characterization techniques and high pressure performance.* Advances in Colloid and Interface Science, 2003. **100**: p. 399-473.
68. Tyndall, J., *Faraday as a Discoverer*. 1868: D. Appleton.
69. Harding, S.E. and K. Jumel, *Light scattering.* Current protocols in protein science, 1998. **11**(1): p. 7.8. 1-7.8. 14.
70. Berne, B.J. and R. Pecora, *Dynamic light scattering: with applications to chemistry, biology, and physics*. 2000: Courier Corporation.
71. Lee, J.M., et al. *In-Field Emulsion Treatability Test with the Electrostatic Susceptability Tester*. in *SPE Annual Technical Conference and Exhibition*. 2006. Society of Petroleum Engineers.
72. Chatzi, E. and C. Kiparissides, *Drop size distributions in high holdup fraction dispersion systems: effect of the degree of hydrolysis of PVA stabilizer.* Chemical engineering science, 1994. **49**(24): p. 5039-5052.
73. Choi, M. *Prediction of separator performance under changing field conditions*. in *SPE Annual Technical Conference and Exhibition*. 1990. Society of Petroleum Engineers.
74. Graham, D.E. and A. Stockwell. *Selection of demulsifiers for produced crude oil emulsions*. in *European Offshore Technology Conference and Exhibition*. 1980. Society of Petroleum Engineers.
75. Zhou, H., et al., *Development of More Environmentally Friendly Demulsifiers*, in *SPE International Symposium and Exhibition on Formation Damage Control*. 2012, Society of Petroleum Engineers: Lafayette, Louisiana, USA. p. 11.

76. Pacheco, V.F., et al., *Destabilization of petroleum emulsions: evaluation of the influence of the solvent on additives.* Energy & Fuels, 2011. **25**(4): p. 1659-1666.
77. Zdravkov, A., G. Peters, and H. Meijer, *Film drainage between two captive drops: PEO–water in silicon oil.* Journal of colloid and interface science, 2003. **266**(1): p. 195-201.
78. Atten, P., L. Lundgaard, and G. Berg, *A simplified model of electrocoalescence of two close water droplets in oil.* Journal of Electrostatics, 2006. **64**(7-9): p. 550-554.
79. Lundgaard, L., et al., *Emulsions and emulsion stability. Vol. 132*. 2006, CRC Press, Ch. Electrocoalescence for oil-water separation: Fundamental aspects.
80. Sanfeld, A. and A. Steinchen, *Emulsions stability, from dilute to dense emulsions—role of drops deformation.* Advances in colloid and interface science, 2008. **140**(1): p. 1-65.
81. Stein, H., *The drainage of free liquid films.* Colloids and Surfaces A: Physicochemical and Engineering Aspects, 1993. **79**(1): p. 71-80.
82. Nierstrasz, V.A. and G. Frens, *Marginal regeneration in thin vertical liquid films.* Journal of colloid and interface science, 1998. **207**(2): p. 209-217.
83. Cottrell, F.G., *Process for separating and collecting particles of one liquid suspended in another liquid*. 1911, Google Patents.
84. Godfrey, J. and M. Slater, *Electrically aided extraction and phase separation equipment.* Liquid–Liquid Extraction Equipment, Wiley, New York, 1994.
85. Chen, C.-T., et al., *Effects of electrolytes and polarity of organic liquids on the coalescence of droplets at aqueous-organic interfaces.* Surface science, 1998. **406**(1-3): p. 167-177.
86. Førdedal, H., et al., *Crude oil emulsions in high electric fields as studied by dielectric spectroscopy. Influence of interaction between commercial and indigenous surfactants.* Colloids and Surfaces A: Physicochemical and Engineering Aspects, 1996. **106**(1): p. 33-47.
87. Brandenberger, H., et al., *Monodisperse particle production: A method to prevent drop coalescence using electrostatic forces.* Journal of electrostatics, 1999. **45**(3): p. 227-238.
88. Williams, T.J. and A.G. Bailey, *Changes in the size distribution of a water-in-oil emulsion due to electric field induced coalescence.* IEEE Transactions on Industry Applications, 1986(3): p. 536-541.
89. Bhardwaj, A. and S. Hartland, *Kinetics of coalescence of water droplets in water-in-crude oil emulsions.* JOURNAL OF DISPERSION SCIENCE ANDTECHNOLOGY, 1994. **15**(2): p. 133-146.
90. Dalmazzone, C. and H. Seris, *Use of the DSC technique to characterize water in crude oil emulsions stability.* Revue de l Institut Francais du Petrole, 1998. **53**(4): p. 463-471.
91. Aske, N., H. Kallevik, and J. Sjöblom, *Water-in-crude oil emulsion stability studied by critical electric field measurements. Correlation to physico-chemical parameters and near-infrared spectroscopy.* Journal of Petroleum Science and Engineering, 2002. **36**(1-2): p. 1-17.
92. Noik, C., J. Chen, and C.S. Dalmazzone. *Electrostatic demulsification on crude oil: A state-of-the-art review*. in *International Oil & Gas Conference and Exhibition in China*. 2006. Society of Petroleum Engineers.
93. Eow, J.S., et al., *Electrostatic enhancement of coalescence of water droplets in oil: a review of the current understanding.* Chemical engineering journal, 2001. **84**(3): p. 173-192.

94. Yang, D., et al., *The influence and optimisation of electrical parameters for enhanced coalescence under pulsed DC electric field in a cylindrical electrostatic coalescer.* Chemical Engineering Science, 2015. **138**: p. 71-85.
95. Bailes, P. and S. Larkai, *Liquid phase separation in pulsed d. c. fields.* Transactions of the Institution of Chemical Engineers, 1982. **60**(2): p. 115-121.
96. Williams, T., *The resolution of water-in-oil emulsions by the application of an external electric field*. 1989, University of Southampton.
97. Taylor, S., *Theory and Practice of Electrically-Enhanced Phase-Separation of Water-in-Oil Emulsions.* Chemical engineering research & design, 1996. **74**(5): p. 526-540.
98. Yang, D., et al., *Critical electric field strength for partial coalescence of droplets on oil–water interface under DC electric field.* Chemical Engineering Research and Design, 2018. **136**: p. 83-93.
99. Waterman, L.C., *Electrical Coalescers: Theory and Practice*. 1965.
100. Galvin, P., *Design principles for electrical coalescers.* Proc. Extraction" 84, EFCE, 2013. **43**: p. 101-113.
101. Souza, W., et al., *Effect of water content, temperature and average droplet size on the settling velocity of water-in-oil emulsions.* Brazilian Journal of Chemical Engineering, 2015. **32**(2): p. 455-464.
102. Xia, Y. and J.-L. Reboud, *Hydrodynamic and electrostatic interactions of water droplet pairs in oil and electrocoalescence.* Chemical Engineering Research and Design, 2019. **144**: p. 472-482.
103. Vivacqua, V., et al., *Electrocoalescence of water drop trains in oil under constant and pulsatile electric fields.* Chemical Engineering Research and Design, 2015. **104**: p. 658-668.
104. Anand, V., et al., *Electrocoalescence of a pair of conducting drops in an insulating oil.* Journal of Fluid Mechanics, 2019. **859**: p. 839-850.
105. Kamp, J. and M. Kraume, *Coalescence efficiency model including electrostatic interactions in liquid/liquid dispersions.* Chemical Engineering Science, 2015. **126**: p. 132-142.
106. Blass, E., et al., *Hydrodynamic Modeling of Droplet Coalescence at Liquid-Liquid Interfaces.* Int. Chem. Engng, 1992. **32**(4): p. 601-608.
107. Rommel, W., W. Meon, and E. Blass, *Hydrodynamic modeling of droplet coalescence at liquid-liquid interfaces.* Separation science and technology, 1992. **27**(2): p. 129-159.
108. Weheliye, W.H., T. Dong, and P. Angeli, *On the effect of surfactants on drop coalescence at liquid/liquid interfaces.* Chemical Engineering Science, 2017. **161**: p. 215-227.
109. Zhang, X., O.A. Basaran, and R.M. Wham, *Theoretical prediction of electric field-enhanced coalescence of spherical drops.* AIChE Journal, 1995. **41**(7): p. 1629-1639.
110. Urdahl, O., et al., *Electrostatic destabilization of water-in-oil emulsions under conditions of turbulent-flow.* Chemical engineering research & design, 1996. **74**(2): p. 158-165.
111. Bailes, P., *Column Liquid Contacting with Vigorous an Agitation Balanced by Electrostatic Coalescence.* Chem. Eng. Res. Des., 1987. **65**: p. 514-523.
112. Pohl, H.A., *The motion and precipitation of suspensoids in divergent electric fields.* Journal of Applied Physics, 1951. **22**(7): p. 869-871.
113. Urdahl, O., et al., *Development of a new, compact electrostatic coalescer concept.* SPE Production & Facilities, 2001. **16**(01): p. 4-8.

114. Mhatre, S., et al., *Electrostatic phase separation: A review.* Chemical Engineering Research and Design, 2015. **96**: p. 177-195.
115. Bo-Ping, R. and K. Yong. *Movement Behavior of Oil Drops and Demulsification of Oil-in-water (O/W) Emulsion under Direct Current Pulsed Electric Field*. in *2018 International Conference on Energy Development and Environmental Protection (EDEP 2018)*. 2018. Atlantis Press.
116. Eow, J.S. and M. Ghadiri, *Electrostatic enhancement of coalescence of water droplets in oil: a review of the technology.* Chemical Engineering Journal, 2002. **85**(2-3): p. 357-368.
117. Panofsky, W.K. and M. Phillips, *Classical electricity and magnetism*. 2005: Courier Corporation.
118. Eow, J.S., *Electrostatic enhancement of coalescence of water drops in oil*. 2002, University of Surrey (United Kingdom). http://epubs.surrey.ac.uk/842815/. p. 273.
119. Block, R.J., E.L. Durrum, and G. Zweig, *A manual of paper chromatography and paper electrophoresis*. 2016: Elsevier.
120. Manning, F.S. and R.E. Thompson, *Oilfield processing of petroleum: Crude oil*. Vol. 2. 1995: Pennwell books.
121. Pohl, H.A., *Some effects of nonuniform fields on dielectrics.* Journal of Applied Physics, 1958. **29**(8): p. 1182-1188.
122. Baklanov, M., K. Maex, and M. Green, *Dielectric films for advanced microelectronics*. Vol. 12. 2007: John Wiley & Sons.
123. Datta, S., et al., *Investigation of droplet coalescence propelled by dielectrophoresis.* AIChE Journal, 2019. **65**(2): p. 829-839.
124. Hou, L., et al., *Continuously electrotriggered core coalescence of double-emulsion drops for microreactions.* ACS applied materials & interfaces, 2017. **9**(14): p. 12282-12289.
125. Sadeghi, H.M., et al., *Coalescence of charged droplets in outer fluids.* Journal of Colloid and Interface Science, 2018. **532**: p. 363-374.
126. Melcher, J.R., *Continuum electromechanics*. 1981, Cambridge, Mass.: MIT Press. 618 p. in various pagings.
127. Aryana, K., et al., *A review on Electrohydrodynamic (EHD) pumps*. 2016.
128. Iverson, B.D. and S.V. Garimella, *Recent advances in microscale pumping technologies: a review and evaluation.* Microfluidics and Nanofluidics, 2008. **5**(2): p. 145-174.
129. Melcher, J.R., *Traveling-Wave Induced Electroconvection.* The Physics of Fluids, 1966. **9**(8): p. 1548-1555.
130. Ohyama, R., A. Watson, and J.S. Chang, *Electrical current conduction and electrohydrodynamically induced fluid flow in an AW type EHD pump.* Journal of Electrostatics, 2001. **53**(2): p. 147-158.
131. Goldman, M., A. Goldman, and R. Sigmond, *The corona discharge, its properties and specific uses.* Pure and Applied Chemistry, 1985. **57**(9): p. 1353-1362.
132. Atten, P., *Electrohydrodynamic instability and motion induced by injected space charge in insulating liquids.* Ieee Transactions on Dielectrics and Electrical Insulation, 1996. **3**(1): p. 1-17.
133. Vega, F. and A.T. Perez, *Corona-induced electrohydrodynamic instabilities in low conducting liquids.* Experiments in Fluids, 2003. **34**(6): p. 726-735.

134. Chicón, R. and A.T. Pérez, *The stability of a horizontal interface between air and an insulating liquid subjected to charge injection.* Physics of Fluids, 2014. **26**(3).
135. Perez, A.T., *Electrohydrodynamic instabilities in dielectric liquids induced by corona discharge.* Icdl 1996 - 12th International Conference on Conduction and Breakdown in Dielectric Liquids, 1996: p. 126-129.
136. Kawamoto, H. and S. Umezu, *Electrohydrodynamic deformation of water surface in a metal pin to water plate corona discharge system.* Journal of Physics D-Applied Physics, 2005. **38**(6): p. 887-894.
137. Mahmoudi, S.R., K. Adamiak, and G.S.P. Castle, *Spreading of a dielectric droplet through an interfacial electric pressure.* Proceedings of the Royal Society A: Mathematical, Physical and Engineering Science, 2011. **467**: p. 3257-3271.
138. Ohyama, R., et al., *A fundamental characteristic and image analysis of liquid flow in an AW type EHD pump.* Journal of Visualization, 2005. **8**(4): p. 339-346.
139. Ohyama, R., et al., *Experimental analyses of gas liquid interfacial phenomena in an AW type EHD pump.* 2002 Annual Report Conference on Electrical Insulation and Dielectric Phenomena, 2002: p. 200-203.
140. Kumeta, M., et al., *Current density distribution on gas-liquid two-phase fluid flow in an air-wave type EHD pump.* 2003 Annual Report Conference on Electrical Insulation and Dielectric Phenomena, 2003: p. 690-693.
141. Shutov, A.A., *Flow of an Inclined Surface-Charged Layer in a Longitudinal Electric Field.* Fluid Dynamics, 2003. **38**(5): p. 692-697.
142. Akishev, Y., et al., *The influence of electrode geometry and gas flow on corona-to-glow and glow-to-spark threshold currents in air.* Journal of Physics D-Applied Physics, 2001. **34**(18): p. 2875-2882.
143. Schneider, J.M. and P.K. Watson, *Electrohydrodynamic Stability of Space-Charge-Limited Currents in Dielectric Liquids. I. Theoretical Study.* The Physics of Fluids, 1970. **13**(8): p. 1948-1954.
144. Cagnoni, D., et al., *Multiphysics simulation of corona discharge induced ionic wind.* Journal of Applied Physics, 2013. **114**(23): p. 233301.
145. Juraschek, R. and F. Röllgen, *Pulsation phenomena during electrospray ionization.* International journal of mass spectrometry, 1998. **177**(1): p. 1-15.
146. Warburg, E., *About silent discharge in gases*, in *Handbuch der Physik*. 1927, Springer Berlin-Heidelberg. p. 149-170.
147. Sigmond, R., *Simple approximate treatment of unipolar space-charge-dominated coronas: The Warburg law and the saturation current.* Journal of Applied Physics, 1982. **53**(2): p. 891-898.
148. Ohyama, R. and K. Kaneko, *Optical characterization of steady electrohydrodynamic fluid motion induced by surface corona discharge.* 1998 Annual Report Conference on Electrical Insulation and Dielectric Phenomena, Vols 1 and 2, 1998: p. 158-161.
149. S. Herrick, C., *Electroconvection Cells in Dielectric Liquids Interfaced with Conducting Fluids*. Vol. 336. 1974. 487-494.
150. Tinevez, J.-Y., et al., *TrackMate: An open and extensible platform for single-particle tracking.* Methods, 2017. **115**(Supplement C): p. 80-90.

151. Aldrees, A. and M. Nachabe, *Capillary Length and Field Capacity in Draining Soil Profiles.* Water Resources Research, 2019. **55**(5): p. 4499-4507.
152. Sun, T., C.D. White, and Y. Shuai, *Scaling analysis of capillary transition zones.* International Journal of Oil, Gas and Coal Technology, 2018. **19**(1): p. 22-34.
153. Ganan-Calvo, A.M., et al., *Steady capillary jet length.* arXiv preprint arXiv:1908.10841, 2019.
154. Atten, P., J. Raisin, and J.-L. Reboud. *Field induced disruption of a planar water-oil interface influenced by a close metallic sphere*. in *Dielectric Liquids, 2008. ICDL 2008. IEEE International Conference on*. 2008. IEEE.
155. Chiesa, M. *Electrocoalescence modeling: an engineering approach*. in *15th Australasian Fluid Mechanics Conference, Sydney, Australia*. 2004.
156. Schramm, L.L., *Emulsions, foams, and suspensions: fundamentals and applications*. 2006: John Wiley & Sons.
157. Klasson, K.T., et al., *Modification of a Centrifugal Separator for In-Well Oil-Water Separation.* Separation Science and Technology, 2005. **40**(1-3): p. 453-462.
158. Chan, C.-C. and Y.-C. Chen, *DEMULSIFICATION OF W/O EMULSIONS BY MICROWAVE RADIATION.* Separation Science and Technology, 2002. **37**(15): p. 3407-3420.
159. Xu, B., et al., *Influence of Water Content and Temperature on Stability of W/O Crude Oil Emulsion.* Petroleum Science and Technology, 2013. **31**(10): p. 1099-1108.
160. Sadek, S.E. and C.D. Hendricks, *Electrical Coalescence of Water Droplets in Low-Conductivity Oils.* Industrial & Engineering Chemistry Fundamentals, 1974. **13**(2): p. 139-142.
161. Solomon, B.R., M.N. Hyder, and K.K. Varanasi, *Separating Oil-Water Nanoemulsions using Flux-Enhanced Hierarchical Membranes.* Scientific Reports, 2014. **4**(1): p. 5504.
162. Harami, H.R., et al., *Mixed Matrix Membranes for Sustainable Electrical Energy-Saving Applications.* ChemBioEng Reviews, 2021. **8**(1): p. 27-43.
163. Takahashi, Y., N. Koizumi, and Y. Kondo, *Active Demulsification of Photoresponsive Emulsions Using Cationic–Anionic Surfactant Mixtures.* Langmuir, 2016. **32**(3): p. 683-688.
164. Couck, S., et al., *Adsorption and Separation of Small Hydrocarbons on the Flexible, Vanadium-Containing MOF, COMOC-2.* Langmuir, 2015. **31**(18): p. 5063-5070.
165. Chiba, A., A. Oshima, and R. Akiyama, *Confined Space Enables Spontaneous Liquid Separation by Molecular Size: Selective Absorption of Alkanes into a Polyolefin Cast Film.* Langmuir, 2019. **35**(52): p. 17177-17184.
166. Wu, J., et al., *Effect of Demulsifier Properties on Destabilization of Water-in-Oil Emulsion.* Energy & Fuels, 2003. **17**(6): p. 1554-1559.
167. SA, A.R., et al., *Gas barrier and mechanical properties of crosslinked ethylene vinyl acetate nanocomposites.* Journal of Composite Materials, 2013. **47**(23): p. 2987-2993.
168. Hano, T., T. OHTAKE, and K. TAKAGI, *Demulsification kinetics of W/0 emulsion in an AC electric field.* Journal of chemical engineering of Japan, 1988. **21**(4): p. 345-351.
169. Lesaint, C., et al., *Dehydration efficiency of AC electrical fields on water-in-model-oil emulsions.* Colloids and Surfaces A: Physicochemical and Engineering Aspects, 2009. **352**(1-3): p. 63-69.

170. Berg, G., L.E. Lundgaard, and N. Abi-Chebel, *Electrically stressed water drops in oil.* Chemical Engineering and Processing: Process Intensification, 2010. **49**(12): p. 1229-1240.
171. Suemar, P., et al., *Quantitative evaluation of the efficiency of water-in-crude-oil emulsion dehydration by electrocoalescence in pilot-plant and full-scale units.* Industrial & Engineering Chemistry Research, 2012. **51**(41): p. 13423-13437.
172. Pearce, C., *The mechanism of the resolution of water-in-oil emulsions by electrical treatment.* British Journal of Applied Physics, 1954. **5**(4): p. 136.
173. Bezemer, C. and G. Croes, *Motion of water droplets of an emulsion in a non-uniform field.* British Journal of Applied Physics, 1955. **6**(6): p. 224.
174. Leary, T., M. Yeganeh, and C. Maldarelli, *Microfluidic Study of the Electrocoalescence of Aqueous Droplets in Crude Oil.* ACS Omega, 2020. **5**(13): p. 7348-7360.
175. Mainier, F., et al., *Passivation of the Zinc Anode of a Crude Oil Vertical Separator Resulting in Corrosion*. Vol. 6. 2016.
176. Luo, S., J. Schiffbauer, and T. Luo, *Effect of electric field non-uniformity on droplets coalescence.* Physical Chemistry Chemical Physics, 2016. **18**(43): p. 29786-29796.
177. Luo, X., et al., *Breakup characteristics of aqueous droplet with surfactant in oil under direct current electric field.* Journal of Colloid and Interface Science, 2017. **505**: p. 460-466.
178. Atten, P. *Elect rohydrodynamics of dispersed drops of conducting liquid: from drop deformation and interaction to emu lsion evolution*. in *Proceedings of the International Symposium on Electrohydrodynamics, Gda nsk, Poland, Se ptember*. 2012.
179. Ristenpart, W., et al., *Non-coalescence of oppositely charged drops.* Nature, 2009. **461**(7262): p. 377.
180. Mhatre, S. and R. Thaokar, *Electrocoalescence in non-uniform electric fields: An experimental study.* Chemical Engineering and Processing: Process Intensification, 2015. **96**: p. 28-38.
181. Xu, J., et al., *Effects of electrode geometry on emulsion dehydration efficiency.* Colloids and Surfaces A: Physicochemical and Engineering Aspects, 2019. **567**: p. 260-270.
182. Eow, J.S. and M. Ghadiri, *Drop–drop coalescence in an electric field: the effects of applied electric field and electrode geometry.* Colloids and Surfaces A: Physicochemical and Engineering Aspects, 2003. **219**(1-3): p. 253-279.
183. Abd Rahman, N., F. Ibrahim, and B. Yafouz, *Dielectrophoresis for biomedical sciences applications: A review.* Sensors, 2017. **17**(3): p. 449.
184. Chang, J., P.A. Lawless, and T. Yamamoto, *Corona discharge processes.* IEEE Transactions on Plasma Science, 1991. **19**(6): p. 1152-1166.
185. Mahmoudi, S.R., K. Adamiak, and G.P. Castle, *Spreading of a dielectric droplet through an interfacial electric pressure.* Proc. R. Soc. A, 2011. **467**(2135): p. 3257-3271.
186. Mohamed, M.H., et al., *Deformation of bulk dielectric fluids under corona-initiated charge injection.* Experiments in Fluids, 2020. **61**(5): p. 116.
187. Schneider, J. and P. Watson, *Electrohydrodynamic Stability of Space-Charge-Limited Currents in Dielectric Liquids. I. Theoretical Study.* The Physics of Fluids, 1970. **13**(8): p. 1948-1954.
188. Hartmann, G., *Spectroscopie de la décharge couronne: étude des mécanismes de collisions dans le dard (streamer)*. 1977, Universite de Paris-Sud.

189. Warburg, E., *Handbuch der Physik.* Chapter, 1927. **14**: p. 154-155.
190. Ramos, A., *Electrokinetics and electrohydrodynamics in microsystems*. Vol. 530. 2011: Springer Science & Business Media.
191. Shahbaznezhad, M., A. Dehghanghadikolaei, and H. Sojoudi, *Optimum Operating Frequency for Electrocoalescence Induced by Pulsed Corona Discharge.* ACS Omega, 2020.
192. Shojaeian, M. and S. Hardt, *Mass Transfer via Femtoliter Droplets in Ping-Pong Mode.* Physical Review Applied, 2020. **13**(1): p. 014015.
193. Vasilkov, S., V. Chirkov, and Y.K. Stishkov, *Electrohydrodynamic flow caused by field-enhanced dissociation solely.* Physics of Fluids, 2017. **29**(6): p. 063601.
194. McClements, D.J. and S.M. Jafari, *Improving emulsion formation, stability and performance using mixed emulsifiers: A review.* Advances in colloid and interface science, 2018. **251**: p. 55-79.
195. Abeynaike, A., et al., *The experimental measurement and modelling of sedimentation and creaming for glycerol/biodiesel droplet dispersions.* Chemical engineering science, 2012. **79**: p. 125-137.
196. Yue, X., et al., *Design and fabrication of superwetting fiber-based membranes for oil/water separation applications.* 2019.
197. Ma, W., et al., *Durable superhydrophobic and superoleophilic electrospun nanofibrous membrane for oil-water emulsion separation.* 2018. **532**: p. 12-23.
198. Shehzad, F., et al., *Polymeric surfactants and emerging alternatives used in the demulsification of produced water: A review.* 2018. **58**(1): p. 63-101.
199. Gong, H., et al., *Influence of electric field on water-droplet separated from emulsified oil in a double-field coupling device.* 2018. **550**: p. 27-36.
200. Zhu, Y., et al., *Zwitterionic nanohydrogel grafted PVDF membranes with comprehensive antifouling property and superior cycle stability for oil-in-water emulsion separation.* 2018. **28**(40): p. 1804121.
201. Ribeiro, K.C., et al., *Biodiesel/Water/Glycerol Emulsion Separation Using Electrocoalescence: Model and Process Emulsions.* 2020. **34**(2): p. 1737-1743.
202. Wong, S., et al., *Crude oil emulsion: A review on formation, classification and stability of water-in-oil emulsions.* 2015. **135**: p. 498-504.
203. Eow, J.S. and M.J.C.E.J. Ghadiri, *Electrostatic enhancement of coalescence of water droplets in oil: a review of the technology.* 2002. **85**(2-3): p. 357-368.
204. Less, S., R.J.J.o.P.S. Vilagines, and Engineering, *The electrocoalescers' technology: Advances, strengths and limitations for crude oil separation.* 2012. **81**: p. 57-63.
205. Mohammadi, M.J.J.o.P.S. and Technology, *Population Balance Modeling for Integrating Hydrodynamics with Electrostatics in Crude Oil Electrocoalescers.* 2019. **9**(4): p. 3-21.
206. Anand, V., et al., *Modes of coalescence of aqueous anchored drops in insulating oils under an electric field.* 2019. **568**: p. 294-300.
207. Friedemann, J.D., et al., *Electrostatic attraction of particles: the implications of field theory on coalescer design.* 2004. **22**(7-8): p. 1087-1096.
208. Anand, V., et al., *Electrocoalescence of a pair of conducting drops in an insulating oil.* 2019. **859**: p. 839-850.

209. Aryafar, H. and H.P.J.L. Kavehpour, *Electrocoalescence: effects of DC electric fields on coalescence of drops at planar interfaces.* 2009. **25**(21): p. 12460-12465.
210. Chabert, M., K.D. Dorfman, and J.L.J.E. Viovy, *Droplet fusion by alternating current (AC) field electrocoalescence in microchannels.* 2005. **26**(19): p. 3706-3715.
211. Owe Berg, T., G. Fernish, and T. Gaukler, *The mechanism of coalescence of liquid drops.* Journal of the Atmospheric Sciences, 1963. **20**(2): p. 153-158.
212. Bailes, P., B. PJ, and L. SKL, *An experimental investigation into the use of high voltage DC fields for liquid phase separation.* 1981.
213. Bailes, P. and P.J.J.o.E. Dowling, *The production of pulsed EHT voltages for electrostatic coalescence.* 1985. **17**(3): p. 321-328.
214. Guzman, A.R., et al., *A three-dimensional electrode for highly efficient electrocoalescence-based droplet merging.* 2015. **17**(2): p. 35.
215. Chen, P., et al., *Demulsification and oil recovery from oil-in-water cutting fluid wastewater using electrochemical micromembrane technology.* 2020. **244**: p. 118698.
216. Luo, S., J. Schiffbauer, and T.J.P.C.C.P. Luo, *Effect of electric field non-uniformity on droplets coalescence.* 2016. **18**(43): p. 29786-29796.
217. Anand, V., et al., *Modelling and particle based simulation of electro-coalescence of a water-in-oil emulsion.* 2019. **121**: p. 608-617.
218. Kang, W., et al., *Flocculation, coalescence and migration of dispersed phase droplets and oil–water separation in heavy oil emulsion.* 2012. **81**: p. 177-181.
219. Williams, T.J. and A.G.J.I.T.o.I.A. Bailey, *Changes in the size distribution of a water-in-oil emulsion due to electric field induced coalescence.* 1986(3): p. 536-541.
220. Mengual, O., et al., *TURBISCAN MA 2000: multiple light scattering measurement for concentrated emulsion and suspension instability analysis.* 1999. **50**(2): p. 445-456.
221. Gong, H., et al., *Simulation of the coalescence and breakup of water-in-oil emulsion in a separation device strengthened by coupling electric and swirling centrifugal fields.* 2020. **238**: p. 116397.
222. Yang, D., et al., *Critical electric field strength for partial coalescence of droplets on oil–water interface under DC electric field.* 2018. **136**: p. 83-93.
223. Karimi, M. and R.J.A.J. Andersson, *Dual mechanism model for fluid particle breakup in the entire turbulent spectrum.* 2019. **65**(8): p. e16600.
224. Kim, J., et al., *Experimental study on fluid selection for a stable Taylor cone formation via micro-PIV measurement.* 2020: p. 1-9.
225. Pearce, C.J.B.J.o.A.P., *Reply to motion of water droplets of an emulsion in a non-uniform field.* 1955. **6**(6): p. 224.
226. Eow, J.S., M. Ghadiri, and A.J.J.o.E. Sharif, *Deformation and break-up of aqueous drops in dielectric liquids in high electric fields.* 2001. **51**: p. 463-469.
227. Eow, J.S., et al., *Drop–drop coalescence in an electric field: the effects of applied electric field and electrode geometry.* 2003. **219**(1-3): p. 253-279.
228. Hosseini, M., M. Shahavi, and A.J.A.J.C. Yakhkeshi, *AC & DC-currents for separation of nano-particles by external electric field.* 2012. **24**: p. 181-184.
229. Hosseini, M. and M.J.C.J.o.C.E. Shahavi, *Electrostatic enhancement of coalescence of oil droplets (in nanometer scale) in water emulsion.* 2012. **20**(4): p. 654-658.

230. Zhao, L. and K.J.J.o.e. Adamiak, *EHD flow in air produced by electric corona discharge in pin–plate configuration.* 2005. **63**(3-4): p. 337-350.
231. Wang, X., A. Khomenko, and A. Shashurin, *Enhancement of positive pulsed corona by dielectric enclosure.* AIP Advances, 2019. **9**(10): p. 105029.
232. Keidar, M., et al., *Cold plasma selectivity and the possibility of a paradigm shift in cancer therapy.* British journal of cancer, 2011. **105**(9): p. 1295-1301.
233. Morfill, G. and J. Zimmermann, *Plasma Health Care-Old Problems, New Solutions.* Contributions to Plasma Physics, 2012. **52**(7): p. 655-663.
234. Lee, E.-H., et al., *A disposable bacterial lysis cartridge (BLC) suitable for an in situ water-borne pathogen detection system.* Analyst, 2015. **140**(22): p. 7776-7783.
235. Chua, B. and A. Son, *Sensing absolute air pressure using micro corona discharge.* Sensors and Actuators A: Physical, 2014. **217**: p. 49-55.
236. Sojoudi, H. and M. Shahbaznezhad. *Instabilities of Bulk Dielectric Fluids Under Corona-Initiated Charge Injection*. in *2020 Spring Meeting & 16th Global Congress on Process Safety*. 2020. AIChE.
237. Mohamed, M.H., et al., *Deformation of bulk dielectric fluids under corona-initiated charge injection.* Experiments in Fluids, 2020. **61**: p. 1-12.
238. Huang, X., et al., *Electro-coalescence in Step Emulsification: Dynamics and Applications.* 2020.
239. Moosaie, A., et al., *An algebraic closure model for the DNS of turbulent drag reduction by Brownian microfiber additives in a channel flow.* Journal of Non-Newtonian Fluid Mechanics, 2015. **226**: p. 60-66.
240. Moosaie, A., N. Shekouhi, and A. Ahmadi, *Large-eddy simulation of fiber-induced turbulent drag reduction in a channel flow at Reτ= 180.*
241. Li, M. and D.J.J.o.C.A. Li, *Separation of Janus droplets and oil droplets in microchannels by wall-induced dielectrophoresis.* 2017. **1501**: p. 151-160.
242. Zhao, K. and D.J.J.o.C.A. Li, *Direct current dielectrophoretic manipulation of the ionic liquid droplets in water.* 2018. **1558**: p. 96-106.
243. Smith, W.V. and R.H. Ewart, *Kinetics of emulsion polymerization.* The journal of chemical physics, 1948. **16**(6): p. 592-599.
244. Aveyard, R., B.P. Binks, and J.H. Clint, *Emulsions stabilised solely by colloidal particles.* Advances in Colloid and Interface Science, 2003. **100**: p. 503-546.
245. Shah, R.K., et al., *Designer emulsions using microfluidics.* Materials Today, 2008. **11**(4): p. 18-27.
246. Friberg, S., K. Larsson, and J. Sjoblom, *Food emulsions*. 2003: CRC Press.
247. Jafari, S.M., et al., *Re-coalescence of emulsion droplets during high-energy emulsification.* Food hydrocolloids, 2008. **22**(7): p. 1191-1202.
248. Walstra, P., *Principles of emulsion formation*, in *The Preparation of Dispersions*. 1991, Veldhofen. p. 77-92.
249. Tadros, T.F., *Emulsion formation, stability, and rheology.* Emulsion formation and stability, 2013. **1**: p. 1-75.
250. Gupta, A., et al., *Nanoemulsions: formation, properties and applications.* Soft matter, 2016. **12**(11): p. 2826-2841.

251. Solans, C., et al., *Nano-emulsions.* Current opinion in colloid & interface science, 2005. **10**(3-4): p. 102-110.
252. Juttulapa, M., et al., *Effect of high-pressure homogenization on stability of emulsions containing zein and pectin.* asian journal of pharmaceutical sciences, 2017. **12**(1): p. 21-27.
253. Velázquez-Estrada, R.M., et al., *Evaluation of Mycobacterium smegmatis as indicator of the efficacy of high hydrostatic pressure and ultra-high pressure homogenization treatments for pasteurization-like purposes in milk.* Journal of Dairy Research, 2020: p. 1-9.
254. Yang, Z., et al., *Optimization of low-energy Pickering nanoemulsion stabilized with montmorillonite and nonionic surfactants.* Colloids and Surfaces A: Physicochemical and Engineering Aspects, 2020. **585**: p. 124098.
255. Mashhadi, S., et al., *The effect of Na2SO4 concentration in aqueous phase on the phase inversion temperature of lemon oil in water nano-emulsions.* Journal of Molecular Liquids, 2016. **215**: p. 454-460.
256. Forgiarini, A., et al., *Formation of nano-emulsions by low-energy emulsification methods at constant temperature.* Langmuir, 2001. **17**(7): p. 2076-2083.
257. Jasmina, H., et al., *Preparation of nanoemulsions by high-energy and lowenergy emulsification methods*, in *CMBEBIH 2017*. 2017, Springer. p. 317-322.
258. Karyappa, R.B., A.V. Naik, and R.M. Thaokar, *Electroemulsification in a uniform electric field.* Langmuir, 2016. **32**(1): p. 46-54.
259. LONG, R.-m., Y.-g. LIU, and S.-b. WANG, *Application of electroemulsification in microsphere preparation.* Food Science and Technology, 2010(5): p. 42.
260. Rafieian, S., et al., *A review on nanocomposite hydrogels and their biomedical applications.* Science and Engineering of Composite Materials, 2019. **26**(1): p. 154.
261. Nawab, M. and S. Mason, *The preparation of uniform emulsions by electrical dispersion.* Journal of Colloid Science, 1958. **13**(2): p. 179-187.
262. Hughes, J. and I. Pavey, *Electrostatic emulsification.* Journal of Electrostatics, 1981. **10**: p. 45-55.
263. Moreau, E., et al., *Electrohydrodynamic force produced by a wire-to-cylinder dc corona discharge in air at atmospheric pressure.* Journal of Physics D: Applied Physics, 2013. **46**(47): p. 475204.
264. Sosa, J.M., et al., *Development and application of MIPAR™: a novel software package for two-and three-dimensional microstructural characterization.* Integrating Materials and Manufacturing Innovation, 2014. **3**(1): p. 10.
265. Energy, D.o., 2012.